Some electrical and structural properties of Pr-Ce alloys

M. Altunbas

Altunbas, M. (1975) Some electrical and structural properties of Pr-Ce alloys. Doctoral thesis, Durham University.

SOME ELECTRICAL AND STRUCTURAL PROPERTIES OF Pr-Ce ALLOYS

by

M. ALTUNBAS B.Sc.

A thesis submitted to the University of Durham

for the degree of

Doctor of Philosophy

July 1975

Department of Physics
Science Laboratories
Durham University
Durham City

ACKNOWLEDGMENTS

I am grateful to Professor K.N.R. Taylor of the University of New South Wales, Australia, who supervised the first part of this work and to Dr. W.D. Corner for the supervision of the second part of the work. My gratitude also goes to Professor G.D. Rochester and to his successor, Professor A.W. Wolfendale, for the research facilities made available to me and to the staff of the Physics Department workshops for their technical assistance on apparatus construction.

I greatly appreciate the helpful discussions with Dr. G.A. Wilkinson and I should like to thank Dr. I.R. Harris of Birmingham University for giving his data prior to publication and for providing the experimental facilities needed for the X-ray diffraction studies. My thanks also go to the following: Dr. J. Crangle of Sheffield University for the preparation of the La-Ce alloys and Mrs. E.M. Johnston for drawing the diagrams in the thesis. Finally I would like to thank Mrs. J. Henderson for carefully typing the thesis.

The work was performed during the tenure of a Research Studentship from the Turkish Ministry of Education to whom I am also greatly indebted.

ABSTRACT

The electrical resistivity of praseodymium-cerium (Pr-Ce) and lanthanum-cerium (La-Ce) alloys has been studied in the temperature range 1.3 - 1100 K and 0 - 900°C respectively. The present data have confirmed the existence of a conventional Kondo divergence at $T = 0$ K in double-hexagonal close packed Pr-Ce alloys. In addition to this, evidence has been found of structure at about 20 K and 90 K. This is tentatively ascribed to the presence of Kondo sidebands of the type discussed by Maranzana. These Kondo sidebands are related to the cerium crystalline electric field levels expected in the Pr-Ce alloys on the basis of Rainford's (1971) crystalline electric field parameters for pure praseodymium. Evidence has also been obtained, under certain conditions, for the existence of antiferromagnetic ordering in the alloys at around 26 K.

In connection with the structural properties, the dhcp $\rightleftarrows$ fcc phase transition in the Pr-Ce alloys and the absence of this transition in pure praseodymium have been discussed on the basis of electrical resistivity and X-ray powder diffraction data. At high temperatures, a hysteresis loop for the dhcp $\rightleftarrows$ fcc transition in the Pr-Ce alloys has been observed which decreased in size with increasing praseodymium content and vanished in the $Ce_{.10}Pr_{.90}$ alloy. No hysteresis was observed with alloys of higher praseodymium content. The similarity between the atomic volumes of the dhcp - Pr and the hypothetical fcc-Pr phases and the disappearance of the dhcp $\rightleftarrows$ fcc transition in the Pr-Ce alloys containing more than 90 at.% Pr have indicated the possibility that there is a delicate relationship in favour of the dhcp phase towards the praseodymium end. The observed positive deviation from the line connecting the atomic volumes of the dhcp-Pr and dhcp-Ce has been attributed to the change of the effective valency of cerium from 3.1 to 3. A tentative phase diagram for the Pr-Ce system has been presented which is similar to the La-Nd phase diagram proposed by Gschneidner (1961).

CONTENTS

CHAPTER 3 THE PHASE TRANSFORMATION IN La, Ce and Pr

CHAPTER 5

CHAPTER 6 THE INFLUENCE OF THE CRYSTALLINE ELECTRIC FIELD ON THE KONDO EFFECT OF ALLOYS WITH CERIUM IMPURITIES

CHAPTER 7 RESULTS AND DISCUSSION OF ELECTRICAL PROPERTIES OF Pr-Ce ALLOYS

CHAPTER 1

INTRODUCTION

The experimental results on a variety of alloys and compounds containing magnetic impurities show at high temperatures a decrease in resistivity with decrease of temperature followed by a logarithmic increase in resistivity with further decrease of temperature over a considerable temperature range. This contrasts with the monotonic decrease found in many metals and alloys. Recently, there has been a great effort in order to have a better understanding of this resistance minimum, both theoretically and experimentally. Kondo made the first important step in this respect in 1964 and the effect is usually given his name.

The Kondo effect, in systems containing rare earth impurities, is closely connected with the presence of a 4f level of the magnetic ions close to the Fermi level of the conduction electrons. Two models are generally considered to explain the Kondo effect.

1. The s-f exchange model which assumes a localized magnetic impurity spin $\vec{S}$ coupled to the conduction electron spin $\vec{s}$ by an interaction of the form

$$H = -\Gamma \vec{S}.\vec{s} \qquad \Gamma \text{ ; exchange coupling constant.}$$

2. The Anderson model which introduces the impurity as a localized extra orbital in a free electron gas, but it has been shown that the Anderson model leads to an exchange type Hamiltonian in the case of small mixing.

It is remarkable that of the fourteen rare earth ions only cerium and ytterbium are known to give rise to a Kondo effect, and then only in certain suitable paramagnetic host materials. Ytterbium has been relatively little studied in this respect, attention having centred largely on cerium either in a rare earth-like host (La or Y) or in the form of compounds or alloys with non-rare earth metals (aluminium and magnesium respectively). In all these cases it has been established that the cerium ion is in its trivalent (magnetic) state rather than the tetravalent (non-magnetic), yet the occurrence of the Kondo effect is surprisingly variable. For example, the magnetically dilute Mg-Ce alloys do not show a Kondo effect at all, while Al-Ce compounds have a wealth of Kondo behaviour extending out to temperatures as high as 300 K. The La-Ce and Y-Ce alloys also continue to show Kondo behaviour for large Ce concentrations. It has been explained that the absence of a Kondo effect in Mg-Ce alloys is due to a large energy gap between the Fermi level and the cerium 4f levels resulting in a negligible s-f exchange interaction. Presumably in the other systems mentioned this gap is much smaller and gives rise to considerable s-f mixing.

So far, the magnetic ion has been assumed to be a degenerate system, but the effect of the crystal field from its environment is such as to lift partially the (2J+1)-fold degeneracy. This is capable of profoundly modifying the Kondo effect leading to the dramatic 'Kondo sideband' structure in the electrical resistivity. The Kondo sidebands should arise at the relatively high temperature corresponding to the crystal field splittings. This has been used to give a qualitative explanation of the structure observed in the AlCe compounds.

To date, praseodymium appears to have received little attention as a host material for the cerium ion apart from the initial demonstration by Nagasawa and Sugawara (1967) that two such alloys (of 0.5 and 1.71 at.% of Ce) do indeed show a Kondo effect. The motivation of the present work was largely to extend these results to a wider range of compositions and temperatures, and hopefully to analyse them in the light of more recent theories of the behaviour of cerium alloys.

In addition, considering the absence of a phase diagram for the PrCe system, it was thought that the electrical resistivity measurements could be useful for the investigation of subsolidus equilibria. At subsolidus temperatures, formation of a new phase will, in most cases, be evidenced by a change in slope in the curve of resistivity versus temperature.

By the Hume-Rothery rules of alloy formation, one would expect Ce and Pr metals to be highly soluble in one another. That is, the size, valence and electronegativity of Ce and Pr are almost identical. However some interesting phase transitions were expected in PrCe systems because of the complex structural nature of Ce metal. Ce is face-centred cubic (γ) at 25°C (after heat treatment at high temperatures) but transforms partially to double hexagonal close-packed (β) structure just below room temperature depending on its metallurgical past. Thus cerium with a "collapsed" (more densely packed) fcc (α) structure at very low temperatures has three allotropic forms between room temperature and 0 K.

The aim of this chapter is to provide a general outline of fundamental concepts related particularly to the light rare earths (La, Ce, Pr, Nd, Sm).

1.1 Electron Configuration of Rare Earth Metals

The rare earth metals are located at the atomic numbers 57-71 forming a sub-group in the periodic table. They have electron configurations of the general form $(Xe)4f^n5d^16s^2$, in which the $4f^n$ shell is progressively filled from $n=0$ for Lanthanum to $n=14$ for Lutecium (see Table (1.1)). As n increases, the relative stability of the 4f levels is enhanced and they fall increasingly below the outer electrons, both energetically and radially.

The wave functions for the 4f electrons (Herman and Skillman, 1963) are nearly zero beyond half the nearest neighbour distance so

Table 1.1 Outer Electron Configurations of the Atoms and ions of the Rare Earth Series

Element	Atomic Number	Neutral Atom	Trivalent Ion
La	57	$5d^1\ 6s^2$	$5s^2\ 5p^6$
Ce	58	$4f^2\ 6s^2$	$4f^1\ 5s^2\ 5p^6$
Pr	59	$4f^3\ 6s^2$	$4f^2\ 5s^2\ 5p^6$
Nd	60	$4f^4\ 6s^2$	$4f^3\ 5s^2\ 5p^6$
Pm	61	$4f^5\ 6s^2$	$4f^4\ 5s^2\ 5p^6$
Sm	62	$4f^6\ 6s^2$	$4f^5\ 5s^2\ 5p^6$
Eu	63	$4f^7\ 6s^2$	$4f^6\ 5s^2\ 5p^6$ †
Gd	64	$4f^7\ 5d^1\ 6s^2$	$4f^7\ 5s^2\ 5p^6$
Tb	65	$4f^9\ 6s^2$	$4f^8\ 5s^2\ 5p^6$
Dy	66	$4f^{10}\ 6s^2$	$4f^9\ 5s^2\ 5p^6$
Ho	67	$4f^{11}\ 6s^2$	$4f^{10}\ 5s^2\ 5p^6$
Er	68	$4f^{12}\ 6s^2$	$4f^{11}\ 5s^2\ 5p^6$
Tm	69	$4f^{13}\ 6s^2$	$4f^{12}\ 5s^2\ 5p^6$
Yb	70	$4f^{14}\ 6s^2$	$4f^{13}\ 5s^2\ 5p^6$ †
Lu	71	$4f^{14}\ 5d^1\ 6s^2$	$4f^{14}\ 5s^2\ 5p^6$

† Normally divalent elements with configurations $4f^7\ 5s^2\ 5p^6$ and $4f^{14}\ 5s^2\ 5p^6$.

there is almost no overlap between 4f shells of adjacent atoms (see Figure (1.1)). Thus the metals can be considered as consisting of tri-positive ions surrounded by a sea of conduction electrons. This view was introduced by measurement of the high temperature susceptibilities which follow a Curie-Weiss law and possess effective moments very close to the free 3+ ion values. Therefore, in calculating the properties of the rare earth metals, it is justifiable to consider an isolated ion, initially and subsequently introduce the additional effects due to the metallic environment. The outer electrons $5d^1 6s^2$ are easily removed to become conduction electrons in the metallic state.

It is well known that the 4f radius and the radius of the valence electrons decreases with increasing atomic number. This phenomenon is known as the lanthanide contraction and arises because the electron distribution in the 4f shell is such that an electron added to this shell cannot screen the remaining 4f electrons or the outer electrons from the added positive nuclear charge. As a result the radii of the outer shells is decreased because of the increased electrostatic attraction. This contraction exerts an influence on the magnetic and structural properties of these metals. Because of the decrease in the radius of the 4f shell across the series which is accompanied by the decrease in the ionic radius there will be a decrease of the spacing in the metals, alloys or compounds of the rare earths as the atomic number increases. Divalent Eu and Yb constitutes exceptions to this contraction.

1.2 The s-f Exchange Interaction

This exchange interaction between the localized and conduction electrons has been studied in detail by several authors. The Hamiltonian of this interaction is usually written in the scalar form

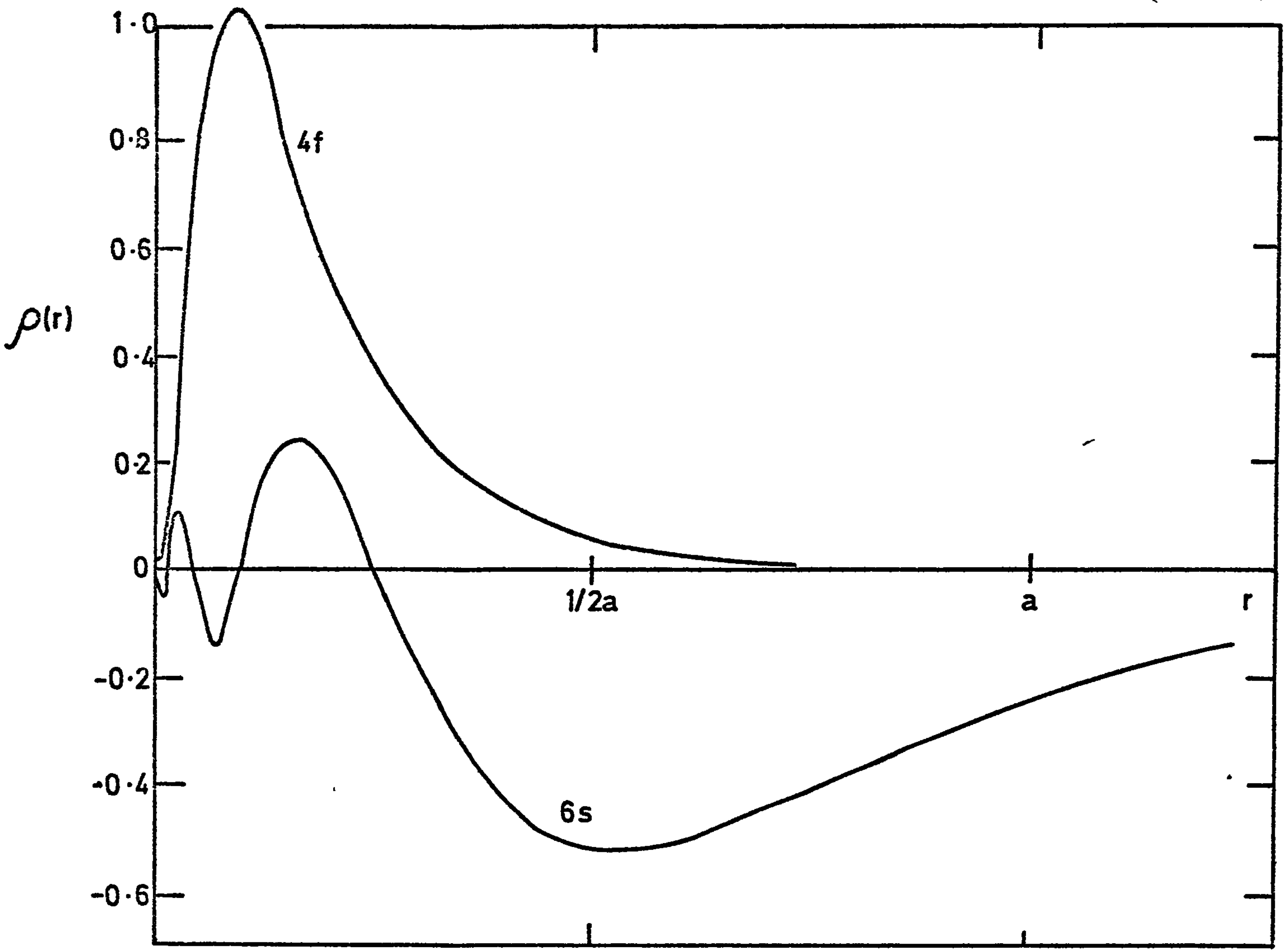

FIG. 1·1. Wave functions for 6s and 4f electrons in neodymium [Herman and Skillman 1963]

$$H = -\Gamma \vec{S}.\vec{s} \qquad (1.1)$$

The effect of exchange of this type was first examined by Rudermann and Kittel (1954) for the case of nuclei interacting via the hyperfine interaction with the conduction electron. Kasuya (1956) and Yosida (1957) extended these ideas and obtained the so-called Rudermann, Kittel, Kasuya, Yosida (RKKY) exchange interaction for materials such as the rare earths.

As a result of the scattering produced by equation (1.1), the 4f shell moment polarizes the spins of the conduction electrons in the neighbourhood of the nth ion. This polarisation $P_n(R)$ is given by

$$P_n(R) = \frac{9\pi z^2}{4v^2} \frac{\Gamma}{\varepsilon_F} S_n F(2k_F R) \qquad (1.2)$$

where z is the number of conduction electrons per atom, v is the atomic volume, ε_F is the Fermi energy, k_F is the Fermi wave vector, R is the distance from the ion and

$$F(x) = \frac{x \cos x - \sin x}{x^4} \qquad x = 2k_F R$$

The function F(x), and hence the polarization is long range, decreasing as R^{-3} for large R so that it is closely centred about the ion site. This resultant polarization is carried over to the vicinity of the other ions and then interacts with the moment of their 4f shells to produce an alignment of the moments. Rudermann and Kittel (1954) showed that the energy of a system of localized moments was lowered by this indirect exchange between the moments.

The main features of this model have remained intact, despite many attempts to improve upon it. Perhaps the most fundamental improvement is the generalization of the interaction for a non-spherical Fermi surface.

The important thing in applying the RKKY interaction to the rare earth metals is to correctly include the effect of the spin-orbit coupling on the spins. de Gennes has shown (1962) for $E_{LS} >> kT$, that it is necessary to make the substitution

$$\vec{S} = (g - 1)\vec{J} \quad . \qquad (1.3)$$

and the s-f exchange Hamiltonian becomes;

$$H = -\Gamma(g - 1)\vec{J}.\vec{s} \qquad (1.4)$$

where g is the Landé g factor.

This type of Hamiltonian leads to a rather puzzling result, namely in the case of cerium alloys, (g-1) is negative, so that there would be a Kondo effect only if Γ were positive, in contrast to transition alloys. This matter will be dealt with in detail in Chapter 6.

1.3 Crystal Structures of the Light Rare Earth Metals

The heavy rare earth metals crystallize in a simple hexagonal close-packed (hcp) structure. The light rare earth metals are considerably more complex in crystal structure than the heavy ones. The first two elements in the series lanthanum and cerium occur in both fcc and double hexagonal close-packed crystal structure. Ce transforms into a more densely packed fcc phase at low temperature. Praseodymium and neodymium, the next two metals in the series, also occur in this dhcp structure. Promethium, which has no stable isotope has not been studied but predicted to have the dhcp structure at 25°C (Gschneidner and Valletta 1968). Sm has the most complex structure of any of the rare earth metals. The crystal structure of Sm is basically hexagonal but it goes through nine layers before it repeats itself. Divalent europium which is the last of the light rare earths has a body-centred cubic structure. See Table (1.2).

The stacking sequences of the double hexagonal close-packed structure is ABACABAC.... where the layer orientation can be visualized by comparison to the hexagonal close-packed structure (ABAB....) and cubic close-packed (ABCABC....). A Schematic representation of dhcp and fcc, hcp and Sm-type crystal forms is shown in Figure 3.1. In the dhcp structure it can be seen that the atoms in the B and C layers have the same nearest neighbours as does an atom in an hcp structure. The atoms in the A layers have the same nearest neighbours as does an atom in an fcc lattice. Thus there are two inequivalent sites in the lattice which makes the dhcp lattice unique among the rare earth crystal structures.

1.4 Alloying Theory

The empirical rules of alloying behaviour for primary substitutional solid solutions were formulated by Hume-Rothery (1936) and relate to ionic size, electronegativity and valence. Gschneidner and Waber (1959) have shown that the Hume-Rothery rules are also applicable to alloy systems containing other metals, lanthanum, cerium, praseodymium and yttrium. Very briefly, these rules are as follows:

Hume-Rothery Rules:

(a) The atomic size factor

If the atomic diameter of the solute atom differs by more than 15 per cent from that of the solvent atom, the extent of primary solid solution is small. The closest distance of approach of the atoms in the lattice has been used as a measure of the atomic size. A favourable size factor is necessary, but not sufficient for extensive solid solubility.

Table 1.2 Crystallographic data for the Rare Earth Metals

Element	Structure	Lattice Parameters c(Å)	 a(Å)	Axial Ratio c/a
La	d-hex	12.134	3.762	3.224 †
Ce	f.c.c.		5.161	
	d-hex	11.778	3.666	3.214 †
Pr	d-hex	11.807	3.664	3.222 †
Nd	d-hex	11.771	3.649	3.226 †
Pm	?			
Sm	Sm-type	26.178	3.621	7.23 ††
Cu	b.c.c.		4.572	
Gd	h.c.p.	5.770	3.627	1.59
Tb	h.c.p.	5.686	3.599	1.580
Dy	h.c.p.	5.642	3.586	1.574
Ho	h.c.p.	5.616	3.572	1.572
Er	h.c.p.	5.582	3.554	1.571
Tm	h.c.p.	5.560	3.536	1.573
Yb	f.c.c.		5.474	
Ln	h.c.p.	5.555	3.503	1.586

† Normally the c/a ratio is given at half this value so reducing it to an effective single layered structure.

†† Frequently the c/a ratio of this element is given as c/4.5a, again reducing the structure to a non-primitive hexagonal form.

(b) The electrochemical factor

Electronegativity is a measure of the reactivity of a metal. The greater the difference in electronegativity between the two metals of a binary system, the greater is the tendency for the two metals to form intermediate phases at the expense of extensive solid solution. Since the electronegativities of the rare earth metals are almost the same, the intermediate phase formation would not normally be expected if both components were the rare earth metals. However some intermediate phases have been shown to exist in a number of binary rare earth alloys indicating that there must be some other factors to explain the alloying behaviour of these systems. For example see La-Gd system, Spedding et al. (1962).

(c) The relative valency effect

The size factor and electronegativity being equal, a metal of lower valency is more likely to dissolve in one of higher valency than the reverse. Since the valencies of the rare earth metals are almost the same, the effect of this rule in binary rare earth alloys will be negligible.

In view of these three empirical rules, one would expect extensive solid solutions in intra - rare earth alloys. However if the components forming a binary system do not have the same crystal structure, the above case should not be expected.

1.5 Crystalline Electric Field

An ion in a lattice is situated in an electrostatic field due to effect of the surrounding charges. This field is called the crystalline electric field. The general effect of this field is to split the degenerate energy levels of the magnetic ions depending on the symmetry properties of the field. This symmetry is related directly to the structure of the lattice.

The crystalline electric field splitting may be typically of the order of 1 eV for 3d-transition elements. In the case of the rare earths, the ions with uncompleted 4f electrons are shielded from the crystalline electric field by the outer filled 5s and 5p shells. Thus crystalline electric field splitting for the rare earths is reduced to a typical order of 10 meV, Purwins (1972). However, cerium, praseodymium and neodymium possess crystalline electric fields which are sufficiently strong to affect their physical and chemical properties. This internal electric field may be expected to modify the magnetic contribution to the total electrical resistivity as will be discussed in a later chapter.

The ground state of a rare earth ion situated in a lattice is a (2J+1)-fold degenerate multiplet ($J = L \mp S$ according to Hund's Rules and Russell-Saunders coupling). The potential at a point (r,θ,ϕ) due to the effect of charges q_i at $\vec{R}_i$ is

$$V(r,\theta,\phi) = \sum_i \frac{q_i}{|\vec{r} - \vec{R}_i|} \qquad (1.5)$$

on a simple point charge model, where q_i is the charge at the ith neighbouring ion. The effect of this field on the ion is to split the (2J+1)-fold degeneracy to an extent depending on the symmetry of the field. There are two important theorems about the energy levels of magnetic ions in a crystalline electric field.

(a) Kramers' Theorem

This states that in the absence of any magnetic fields, the energy levels of an ion with an odd number of electrons can at most be split into doubly degenerate levels by the crystalline electric field. Thus rare earth ions with half integral values of J when situated in a crystalline electric field will have Kramers' degeneracy, (e.g. Ce^{3+}).

(b). Jahn-Teller Effect

When Kramers' theorem does not apply the environment of a magnetic ion will distort and the degeneracy will be lifted. This occurs because the small displacement of the ion will reduce the energy. That is, ions with an even number of electrons will always have a singlet ground state (e.g. Pr^{3+}, $J=4$).

The potential V (equation (1.5)) is assumed to obey Laplace's equation and therefore may be expanded into spherical harmonics in which case the number of terms in the expansion is greatly reduced by the symmetry of the crystal. The terms in the expansion are of the following type (Hutchings 1964).

$$A_\ell^m \, r^\ell \, P_\ell^{|m|} (\cos\theta) \, e^{im\phi} \qquad (1.6)$$

Here r, θ, ϕ are spherical co-ordinates $P_\ell^{|m|}(\cos\theta)$ are Legendre polynominals and A_ℓ^m are constants which are treated as empirical parameters.

In evaluating the matrix elements of V between coupled wave functions that are specified by an angular momentum quantum number J, the angular integrations are easily achieved by the "operator equivalents" method (Stevens 1952). This method eliminates the need to return to the single electron wave-function by using, instead, an "operator equivalent" to Hamiltonian (H), comprising angular momentum operators which act on the angular part of the wave-functions of the coupled system.

The cartesian function f(x,y,z) of a given degree converts to "operator equivalent" form by the replacement of x,y and z by J_x, J_y and J_z respectively, allowing for non-commutation of J_x, J_y and J_z. A few examples are:

$$\sum_i (3z_i^2 - r_i^2) \equiv \alpha_J \langle r^2 \rangle \left[3J_z^2 - J(J+1) \right] = \alpha_J \langle r^2 \rangle O_2^0$$

$$\sum_i (x_i^2 - y_i^2) \equiv \alpha_J \langle r^2 \rangle \left[(J_x^2 - J_y^2) \right] = \alpha_J \langle r^2 \rangle O_2^2$$

$$\sum_i (x_i^4 - 6x_i^2 y_i^2 + y_i^4) = \sum_i \left\{ \left[(x_i + iy_i)^4 + (x_i - iy_i)^4 \right] /2 \right\}$$

$$\equiv \beta_J \langle r^4 \rangle \frac{1}{2} \left[J_+^2 + J_-^2 \right] = \beta_J \langle r^4 \rangle O_4^4$$

(where $J_\pm = J_x \pm iJ_y$ are the step up and step down operators).

Thus matrix elements from the expression

$$\sum_i (3z_i^2 - r_i^2)$$

between coupled states $|L\,S\,J\,J_z\rangle$ are equal to those of $\alpha_J \langle r^2 \rangle O_2^0$ between the angular part of the coupled wavefunctions, i.e.

$$\langle L\,S\,J\,J_z' | \sum_i (3z_i^2 - \gamma_i^2) | L\,S\,J\,J_z \rangle \equiv \alpha_J \langle r^2 \rangle \langle L\,S\,J\,J_z' | \left[3J_z^2 - J(J+1) \right] | L\,S\,J\,J_z \rangle$$

$\langle r^2 \rangle$ is the radial part of the integral, α_J are multiplicative constants depending upon ℓ (the orbital quantum number of the electrons in the unfilled shell). The multiplicative constants for the fourth and sixth degree expressions are β_J and γ_J respectively.

The crystal field Hamiltonian can be written in the following form by using Hutchings' (1964) notation

$$H = \sum_{\ell,m} B_\ell^m O_\ell^m \qquad (1.7)$$

where B_ℓ^m's depend on crystal field parameters

$$B_\ell^m = A_\ell^m \langle r^\ell \rangle \theta_\ell$$

$$\theta_2 = \alpha_J , \quad \theta_4 = \beta_J \quad \text{and} \quad \theta_6 = \gamma_J .$$

Hutchings has tabulated the matrix elements for all these operators between states $|J,M_J>$ for J values corresponding to the rare earths.

The energy matrix can be constructed by using these tables. By suitable matrix operations the original matrix may be simplified to form submatrices, the number of such submatrices being dependent upon the symmetry of the crystal field. The submatrices may be solved in the usual way, by the subtraction of eigenvalues (λ) from the diagonal elements and finding the solution of the resulting secular equation by equating its determinant to zero.

The crystal field levels of Ce^{3+} in double-hexagonal close packed environment of Pr are given in Appendix 1.

1.6 Resistivity near the Néel transition T_N

The characteristic resistivity behaviour of antiferromagnets is a "hump-backed" curve which has a maximum at a temperature below that of the order-disorder Néel temperature T_N. See Figure (1.2). This anomaly at antiferromagnetic-paramagnetic transition in metals has been explained by several authors (Mackintosh 1962, Kasuya 1965, Meaden 1971). In normal metals, the electron states in which the conduction electrons exist are surrounded by Brillouin zone boundaries. In the simple metals the Fermi sphere is completely within a Brillouin zone (see Figure (1.3)). The conduction electrons are at the surface of this sphere, and the conductivity is governed by the area of this surface. Now consider a simple antiferromagnet with two interpenetrating sub-lattices. Each sub-lattice contains parallel spins which are antiparallel to those of the other sub-lattice. Since every sub-lattice has a period within the crystal lattice greater than that of the crystal lattice itself, other zone boundaries will occur. These new zone boundaries may intersect the Fermi sphere. Since these

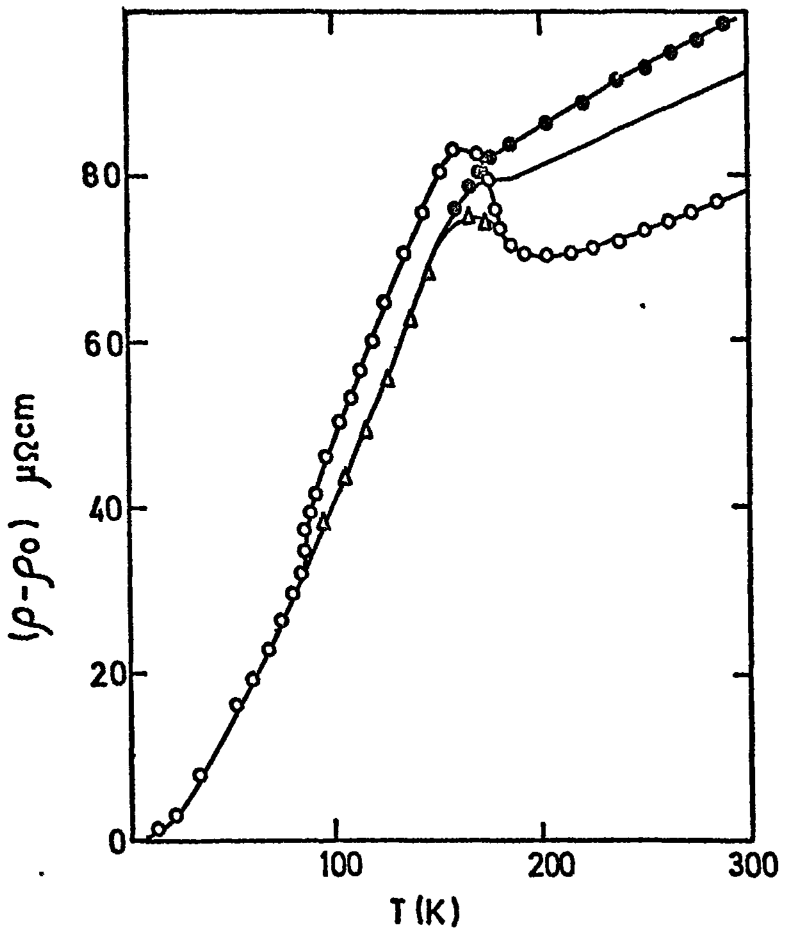

Fig.1.2: The resistivity of Dy: O, C-axis resistivity in zero magnetic field; Δ, c-axis resistivity with the super-zone component eliminated; ●, Basal plane resistivity in zero field; ——, polycrystalline resistivity as calculated from $\rho = (1/3)\ \rho_c + (2/3)\ \rho_b$ (Wilding and Lee 1965)

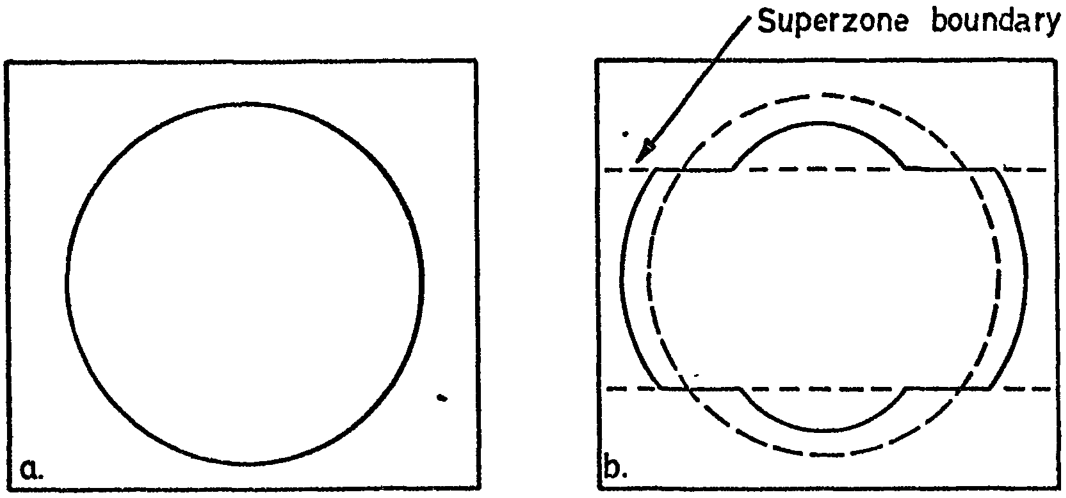

Fig.1.3: The effect of introducing superzones on a spherical Fermi surface a, simple metal, b the intersection of the surface by superzones.

boundaries will bring with them an associated energy gap, the intersections will result in a transfer of electrons from the cut-off (and energetically less favourable) parts of the Fermi sphere to more favourable regions. The effect of these new periodic potentials is shown in Figure (1.3b). Since the electrons on the planes of energy discontinuity cannot contribute to the conductivity, it is clear that the effective surface area of the Fermi sphere in Figure (1.3b) is less than that in Figure (1.3a) and consequently there will be a resistivity increase from a to b.

This is very important when explaining the electronic behaviour of the heavy rare earths with helical and conical spin structures. These have a periodicity in the c axis direction which is appreciably greater than that of the lattice and once formed on decreasing the temperature from the paramagnetic to the antiferromagnetic phase, will lead to the introduction of several new "superzone" boundaries within the fundamental Brillouin zone, some of which will intersect the Fermi surface causing the observed increase in resistivity at T_N.

For the hexagonal rare earths this super-zone scattering has a strong anisotropy which depends on crystal orientation. The effect is maximum along the c-axis and minimum for the basal plane directions. In polycrystalline samples the characteristic hump is considerably weakened due to averaging over the randomly-oriented crystallites. (Colvin, Legvold and Spedding 1960). This would be the situation in polycrystalline double hexagonal close packed Praseodymium and will be discussed in detail in Chapter 7.

CHAPTER 2

EXPERIMENTAL METHODS, APPARATUS

2.1 Alloy Preparation

PrCe and LaCe alloys used for the resistivity measurements were prepared from stock material of nominally better than 99.9% purity purchased in the form of ingots. Pr, La were obtained from Rare-Earth Products Ltd., and in the case of Ce from Koch-Light Laboratories Ltd.

Quantities of the stock metals in the correct proportions for the alloy composition required, and sufficient to form a 5 gm button, were cut and weighed to an accuracy of ± 0.05 mg on a balance kept in an argon atmosphere in the glove box where all the metal cutting was performed.

These buttons were melted in the arc-furnace under a high purity argon atmosphere. This consists of melting together the desired quantities of the required metals on a water cooled copper hearth and a tungsten electrode (see Figure 2.1).

The arc-furnace was pumped down to a pressure of 10^{-3} torr several times and then flushed with high purity argon (Oxygen content less than 3 ppm). Again it was pumped down to 10^{-5} torr and then filled to 300 torr with high purity argon. Remaining oxygen was removed as far as possible by melting a mass of 100 gm of tantalum for about one minute as a getter before melting the sample components together. In order to minimise the loss of material by evaporation the melting of samples was performed at as low a temperature as possible. The buttons were turned over and remelted twice to ensure homogeneous distribution of the Ce solute. To check the homogeneity of the impurity ion in these alloys, the residual resistivity of two specimens which were cut from different parts of the same button were measured and there was not any measurable difference between them. Electron probe microanalysis of the alloys

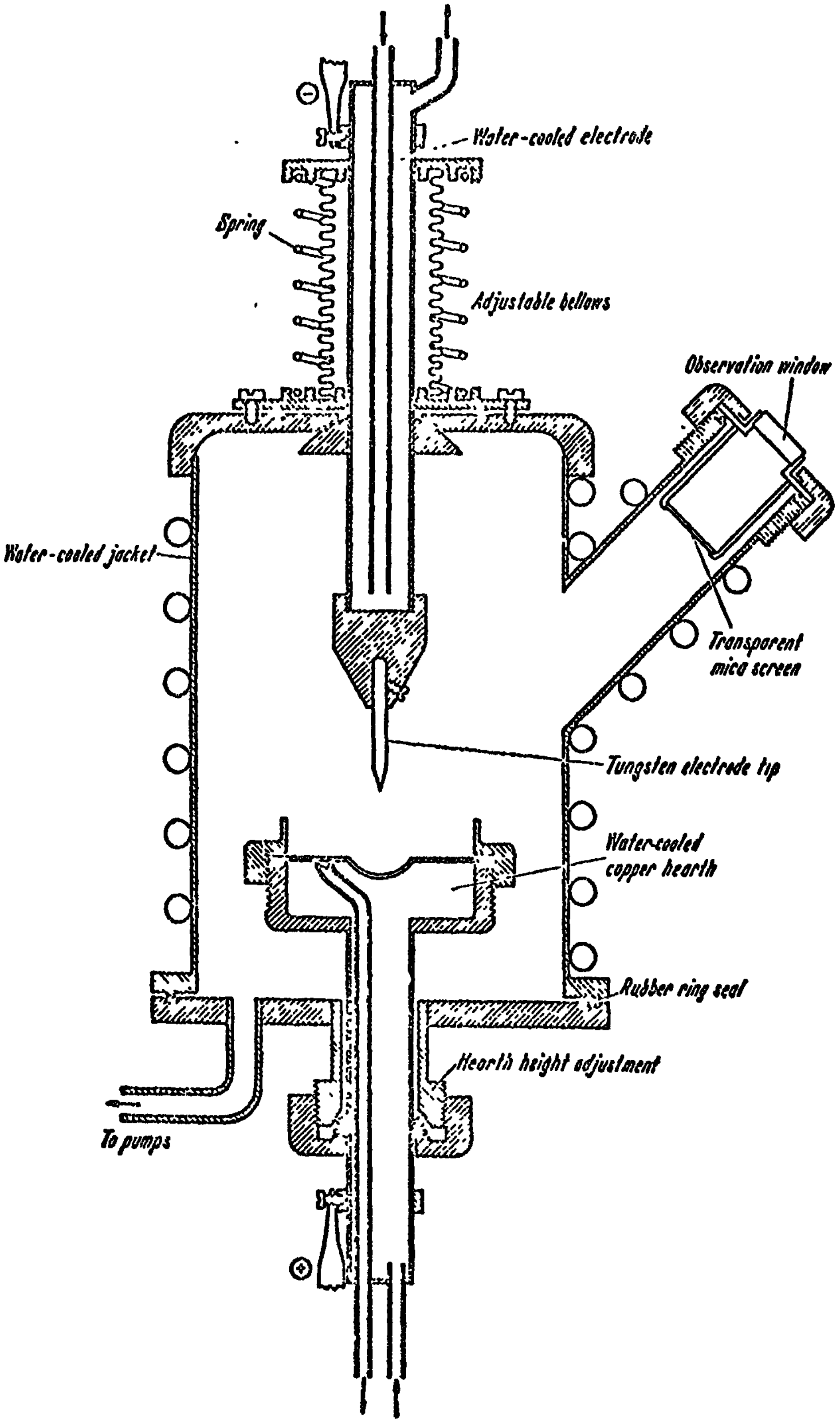

Fig. 2.1: The Arc furnace

verified the accuracy of the nominal Ce concentration, and checked the absence of contaminants from the melting process. Observed weight loss after melting of these alloys was less than 0.01% of the total weight. Surface contamination was checked visually. If present it was filed off in argon atmosphere before annealing the specimens.

2.2 The Preparation of the Powders for X-ray Work

The powders were obtained from the alloys by filing them under carbon tetrochloride to prevent oxidation. In order to improve the quality of the x-ray film the powders were given a stress relief anneal at 600°C for five hours and cooled down to room temperature at a rate of 1°C min^{-1} by a linear programmer. The following steps were taken for the stress relief anneal:

(a) Tantalum boats were prepared in cylindrical form of 3mm diameter with one end closed.

(b) The powders were loaded into the tantalum boats by a funnel and the open ends of the boats were roughly sealed.

(c) The boats containing the powders were transferred from the carbon tetrachloride to a vacuum annealing tube. The furnace temperature was increased slowly for degassing the tantalum boats and pressure did not exceed 6.10^{-5} torr. After five hours of annealing, the powders were cooled down at a rate of 1°C min^{-1}.

2.3 Annealing

The alloys were annealed prior to any resistivity measurements, at a slightly lower temperature ($\sim$100°C) than the expected crystallographic phase transition temperature to ensure phase purity. The specimens were placed in protective tantalum boats and sealed under a vacuum, better than 10^{-6} torr in individual quartz capsules prior to annealing for seven days at a temperature of 600°C followed by cooling to room temperature over a period of two days.

2.4 Samples for Resistivity Measurements

Specimens in the form of rectangular parallelepipeds were cut from the buttons using a high speed diamond saw equipped with vernier traverses. Typical specimen dimensions were 1.7 x 2.8 x 12 mm. The surfaces were sufficiently flat after cutting, that only rubbing on a fine emery paper was necessary to remove any surface oxide layers before applying the electrical contacts to the sample.

Four copper electrodes were lightly spot-welded by a 'Hirst' resistance welding machine to the broad face of each specimen along the central lengthwise dividing line. The current leads were located typically about 1.5 mm from the ends of the specimen, whilst the potential leads were located about 3.3 mm from the ends, thus leaving about 5.4 mm in the middle of the specimen across which the potential was measured. Spot welding of contacts in this way ensures a good metal to metal contact without a complex of intermediate layers.

The connections to all samples used at high temperatures were made with tantalum wire to avoid contamination of the samples. Accurate measurements of the specimen dimensions and lead positions were made for each specimen, using a travelling microscope.

2.5 Resistance Measuring System

The system generally employed for making the resistance measurements was an A.C. one, which had the advantage of eliminating the troublesome effects of thermal e.m.f's. in the leads. The signal current of about 50 mA at 1 kHz was supplied by a Farnell type LFM2 oscillator, and the specimen voltage was fed to a Brookdeal type 432 high input impedance differential preamplifier and then to a Brookdeal type 401 lock-in amplifier. Using a time constant of about 30 sec., this system had a resolution of about 3 nV, corresponding to a maximum resolution of about 5 x 10^{-3} $\mu\Omega$ cm for a typical specimen. However, the absolute resolution of the 401 is a few tenths of a percent of full scale-deflection so that at high temperatures ($\sim$300 K), the resolution is effectively limited at best to about 7 x 10^{-2} $\mu\Omega$ cm. For accurate data-logging, the 401 output was read using a general purpose digital voltmeter and the e.m.f. developed by a thermocouple in contact with the specimen was monitored on a Solartron type A200 digital voltmeter with 1 μV resolution, giving at worst a resolution of about 0.2 K at 70 K and at best about 0.03 K at 300 K. For general purpose data-logging, the amplifier and thermocouple voltages were fed to an X-Y recorder. The signal current was monitored by measuring the voltage across a 0.01 Ω standard resistor in series with the specimens. Occasional checks on the absolute accuracy of the A.C. measuring system were carried out by comparison of the measured A.C. resistance of a specimen at room temperature with that obtained by D.C. means; in this case a constant current of about 0.5 A was passed through the specimen, and voltage developed read with the Solartron digital voltmeter. There appeared to be a consistent difference between the two values so obtained, of rather less than 1% which no doubt can be ascribed to a calibration error in the gain of the 432 amplifier. Fortunately this error was constant from specimen to specimen, and so will have no influence on the comparison between specimens. Block diagram of the resistivity measuring system is shown in Figure 2.2.

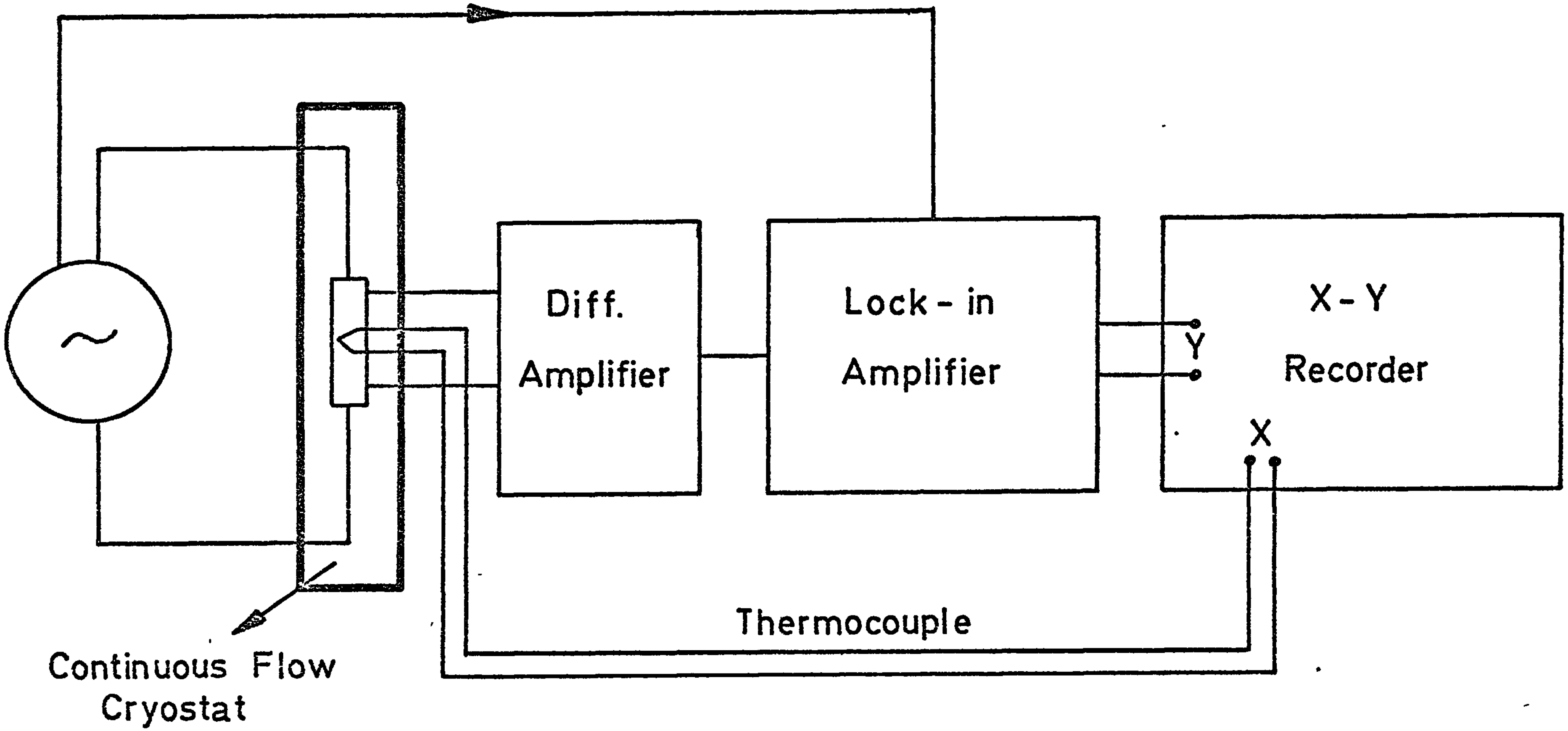

FIG. 2·2 Block diagram of the Resistivity Measuring System

2.6 Calculation of the Resistivity

Ideally, the specimens would have been long and thin with large separations between the ends of the specimen, the current probes, and the voltage probes. However, due to the limited size of the buttons available, a compromise had to be reached resulting in the necessity of making corrections for the non-uniformity of the current flow in the specimen. Stephens, Mackey and Sybert (1971) have treated the case of the geometry of our specimens (termed by them 'F_f') theoretically, and it can be shown that provided $\omega \sim t < \ell, d \ll s$ their calculation reduces to

$$\rho \simeq R \frac{2\omega t}{s} \left[1 - \frac{2}{\pi} \left(\frac{\omega}{s} \exp\left(-\pi d/\omega\right) + \frac{t}{s} \exp\left(-\pi d/t\right) \right) \right] \qquad (2.1)$$

where R is the specimen resistance, ω is the half-width, t is the thickness, s is the separation of the potential leads, d is the separation of neighbouring current and potential leads, and ℓ is the distance of the current lead from the end of the specimen; under these conditions the measured resistance is independent of ℓ.

No correction has been made in the resistivity for the change in dimensions of the specimens with temperature.

2.7 Cryostat Design

The cryostat for the electrical resistivity measurements between 1.3 - 300 K which was built by the author, in general resembles that of Lehmann and Meier (1970). A cross section of the cryostat is shown in Figures 2.3 and 2.4. The dewars were made from pyrex glass. It contains a simple heat exchanger in thermal contact with the sample holder and thermally insulated from the liquid coolant container.

The control of the liquid coolant passing through the heat exchanger is achieved by two Edward's needle valves. One was located

NOT TO SCALE

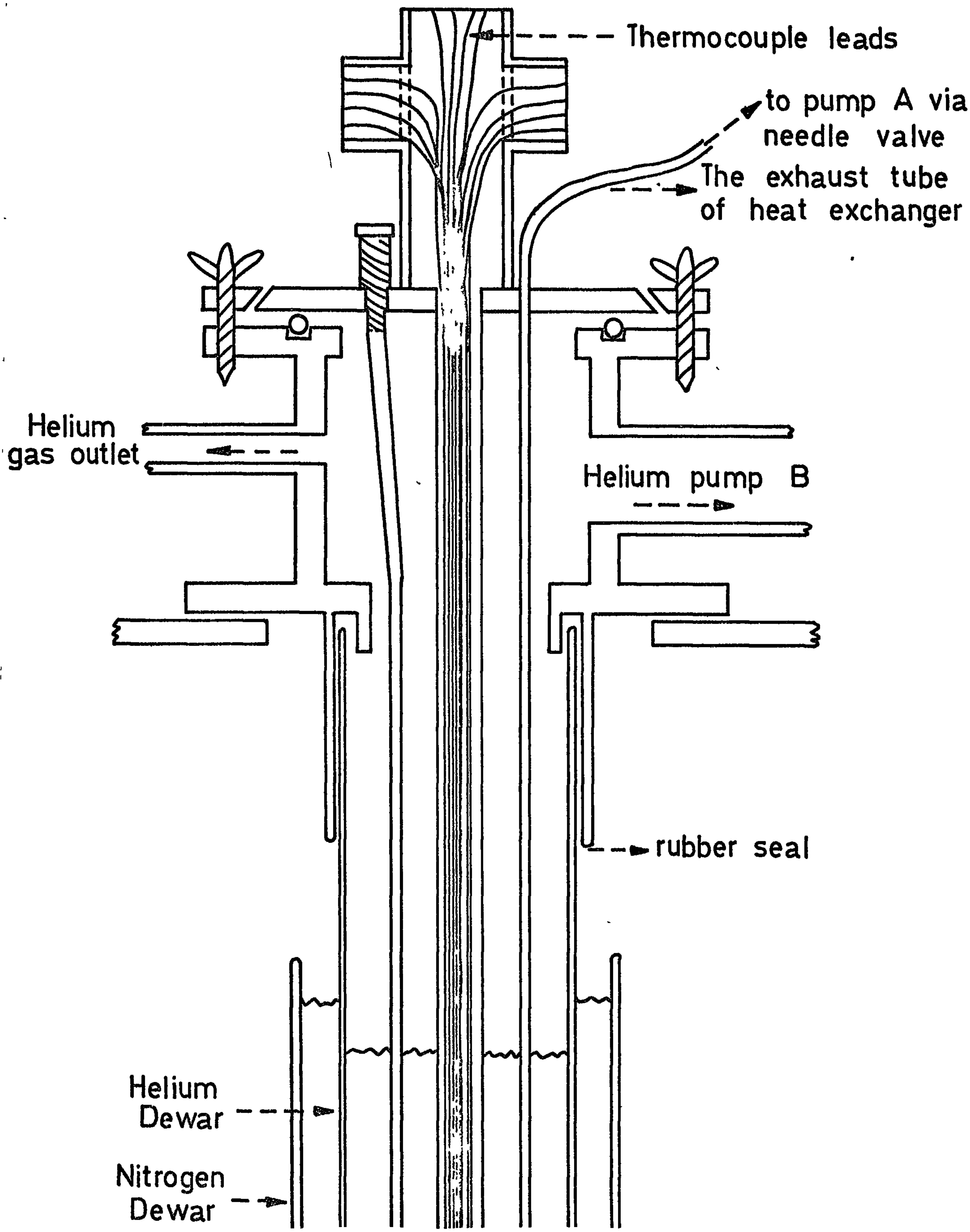

FIG. 2·3 Dewar Head

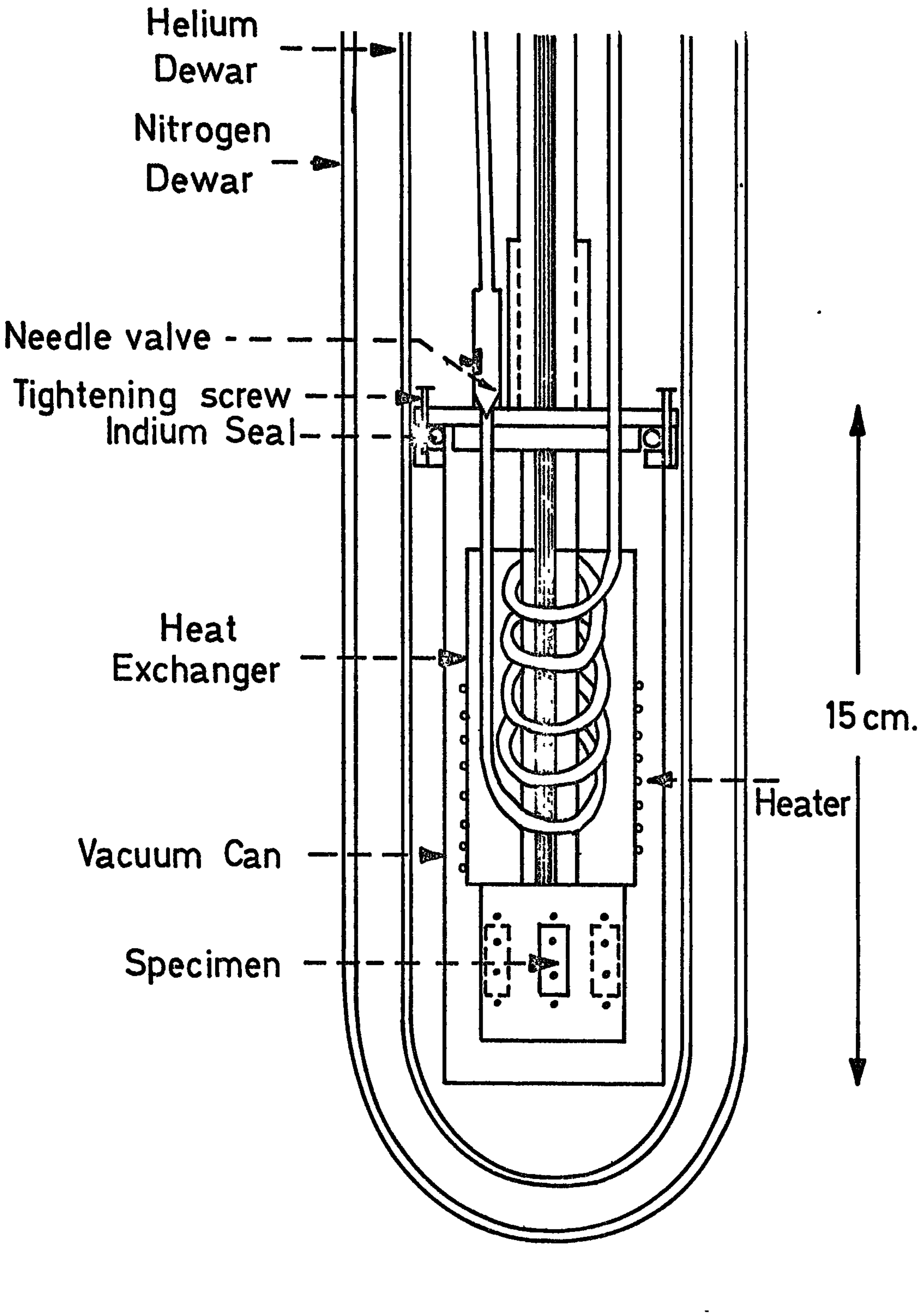

FIG. 2·4 Cryostat for Resistivity Measurements.

in the bottom of the cryostat which could be controlled from the top of the cryostat by means of a flexible steel cable. The other needle valve was inserted between the exhaust tube of the heat exchanger and pump A in Figure 2.3.

A thin walled stainless-steel tube (outside diameter 3.2 mm) connects the liquid helium reservoir and a helical copper tube. This copper tube is mounted around the stainless steel tube of outside diameter 13 mm, which extends up to the top of the cryostat and gives the necessary rigidity. The heat exchanger is made of copper. The thickness of copper sheet used for the end-plates of the heat exchanger was 2 mm. A kanthal resistance wire of 4 Ω is wound around the heat exchanger for the temperature region of 77 - 300 K, in the case of 4.2 - 77 K a constantan wire of 200 Ω was used in the same manner.

Accommodation was provided for a maximum of six specimens on a copper sink which is soldered to the heat exchanger in order to get a good thermal contact. This also provides rather uniform temperature for the specimens. The current leads of the specimens were connected in series and a pair of potential leads per specimen being taken via a multiple switch to the voltage measuring system. The broad faces of the prepared specimens were glued by varnish (G.E. 7031 supplied by Oxford Cryogenics) to the specimen holder to minimise the temperature gradient along the samples. This varnish maintains a good thermal contact in the required temperature region and at the same time works as an electrically insulating medium between the sample and the copper block.

The heat exchanger and the sample holder is surrounded by a vacuum can made of brass and in this way thermally isolated from the liquid coolant container. The vacuum can is attached to the cryostat by means of six tightening screws using an indium O-ring. The indium ring was formed from indium wire of 1.6 mm diameter. The ends were cut on a $\sim 10^{\circ}$ angle with a razor blade and two surfaces pressed together to form a cold weld joint. The dimensions of the vacuum can are 6 cm outside diameter x 18 cm long. A stainless-steel tube (outside diameter 3.2 mm) was used for the exhaust tube of the heat exchanger and leads along the liquid helium reservoir to the top of the cryostat where it is connected to a vacuum pump (A) via a needle valve.

2.8 Temperature Measurements

2.8a 1.3 - 4.2 K Region

The usual procedure for taking data in this temperature range was to remove the vacuum can from the cryostat and fill the inner dewar with He^4. It was possible to obtain a fine control of the pumping rate and therefore of the temperature by means of a needle valve between pump B and the liquid helium bath.

In order to measure the vapour pressure of helium and control the pumping rate, a combination of mercury and differential oil manometer was used. This is shown in Figure 2 5. The needle valve controls the pumping rate and it was possible to measure the vapour pressure from the mercury manometer. To obtain a particular temperature, the tap on the differential oil manometer (T) was closed so that the oil could follow the changes in the vapour pressure of the helium. The changes in the oil level were detected and controlled photoelectrically with an Adkins' stabilizer (1961). The associated circuit is shown in Figure 2.6. The signal resulting from the change of oil level was used to control the power for the heater in the bottom of the helium bath (200 Ω). Thus it was possible to take readings at every 0.25 K down

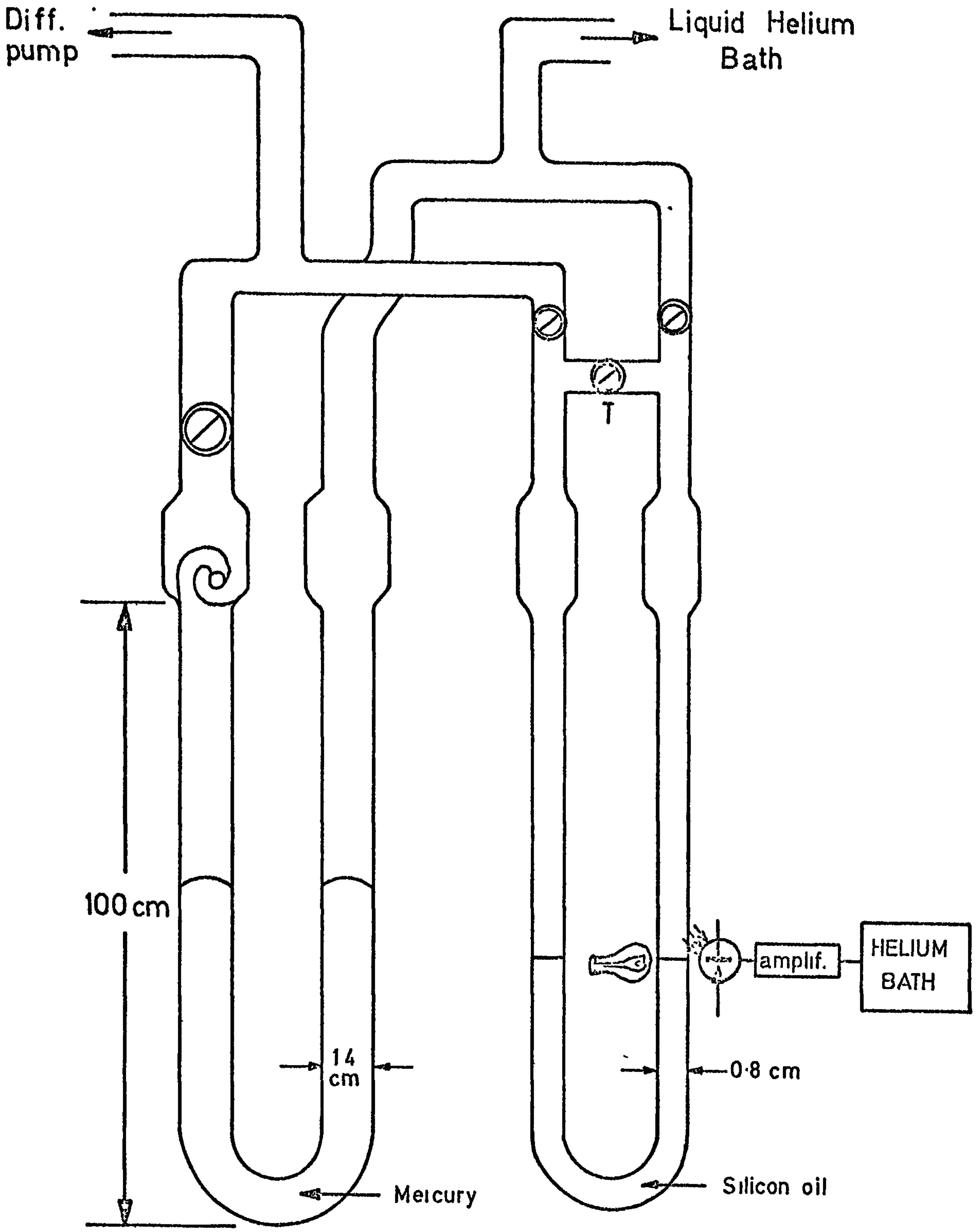

FIG. 2·5 Differential Manometer.

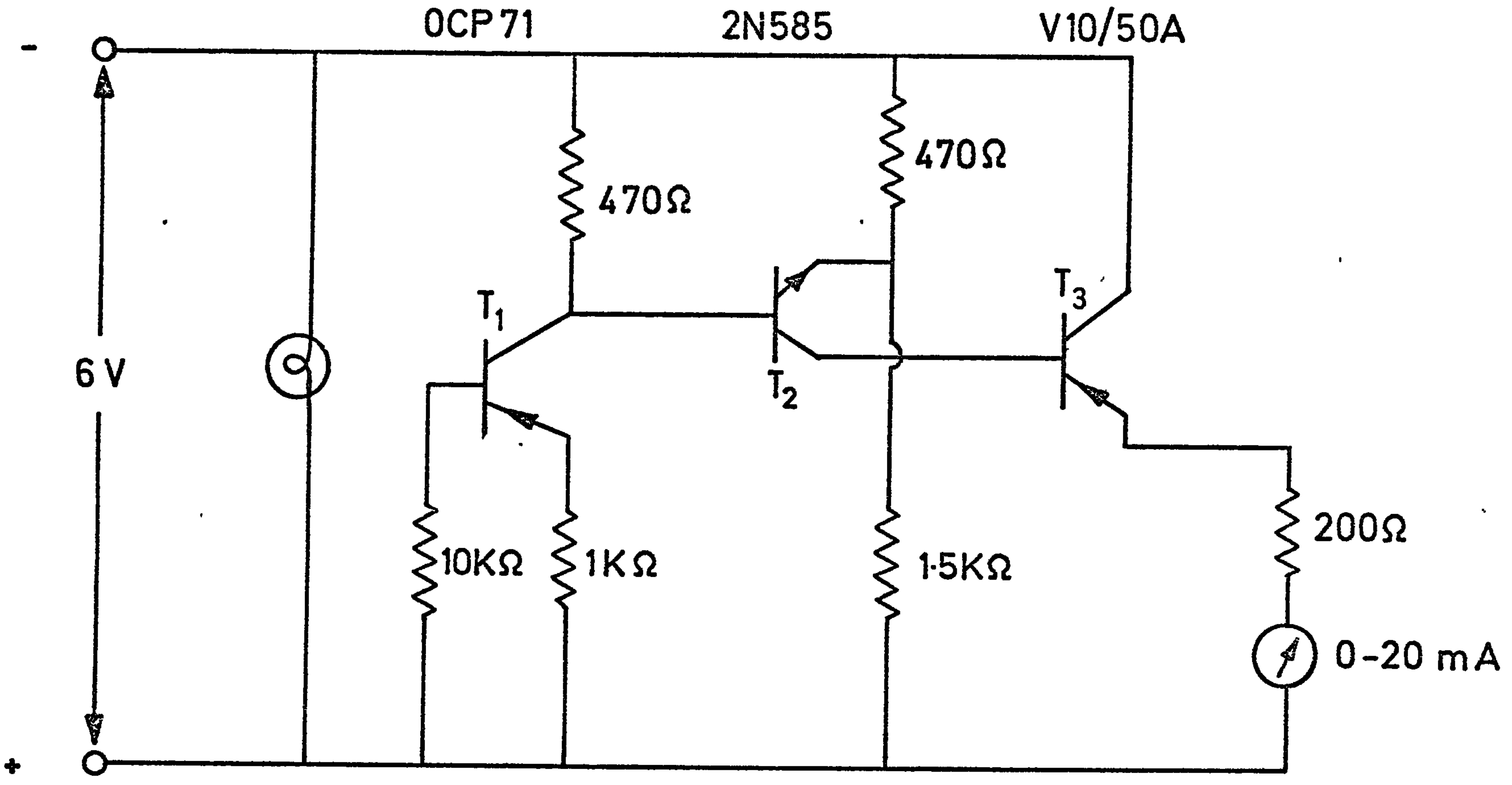

FIG. 2·6. The current amplifier and limiter. (After Adkins C.J., 1961) to 1.3 K, having a temperature stability of better than 10^{-4} degrees.

The mercury and oil manometers are made of pyrex tube with about 13 mm and 8 mm external diameters respectively. The oil manometer was filled with silicon oil (DC 200) and the light was obtained from a pea lamp (6 V, 150 mA).

2.8b 4.2 K - 77 K Range

To achieve temperatures in this range the vacuum can was placed around the heat exchanger. Both needle valves or the heat exchanger circuit were opened for the cooling of the samples down to the helium temperature. The desired temperature was obtained by the valve between the helium bath and the heat exchanger which controlled the amount of liquid circulating in the heat exchanger. The sample temperature is then raised above the temperature of the helium bath by closing this valve and passing an appropriate current through a resistance heater attached to the heat exchanger as mentioned earlier. The liquid helium loss rate increased with increasing temperature of the sample in this system.

The temperature of the heat sink was monitored by a calibrated Cu - (AuFe) thermocouple. The gold wire, available from Oxford Instruments Cryospares Division, had a small (0.2 %) iron addition, giving a thermoelectric power of about 10 μV per degree at helium temperature. The thermocouple voltage was measured by means of a digital voltmeter (Solartron A200).

2.8c 77 K - 300 K Range

The temperature range from 77 K to room temperature was obtained by using liquid nitrogen in the liquid helium reservoir with no liquid nitrogen in the outer dewar. The temperature of the heat exchanger was varied in the same manner as when liquid helium was used. The temperature of the samples were determined by a calibrated Cu-Constantan thermocouple. Both thermocouples were attached to the sample holder. The reference junctions of both thermocouples were at liquid nitrogen.

2.8d 300 K - 1200 K

The samples placed in a quartz tube in which the pressure was kept lower than 10^{-4} torr during the experiment. The specimens were heated in a 60 cm long Kanthal-wound horizontal resistance furnace.

Electrical connections were made of tantalum wire and electrically isolated by means of "Refrasil" high temperature insulation sleeving. The thermocouple wires and all other electrical connections emerge through a glass-metal seal.

Temperature control was achieved by a Eurotherm controller and achromel-alumel thermocouple was used to determine the temperatures and were believed to be correct to $\mp$ 3°C.

2.9 X-Ray Techniques

2.9a The Room Temperature Measurements

The annealed powders were sieved through a 250 grade mesh sieve and coated on to a greased silica fibre. A Debye-Scherrer camera was used for the room temperature x-ray diffraction patterns. The unsymmetrical method of film loading was employed because of accounting for the errors due to film shrinkage.

Cr K_{α} radiation was used. The accurate value of the lattice parameter was found by plotting the lattice parameters containing random and systematic errors against the Nelson-Riley function. (Nelson and Riley, 1945).

$$f(\theta) = \frac{1}{2}\left[\left(\frac{\cos^2\theta}{\sin\theta}\right) + \left(\frac{\cos^2\theta}{\theta}\right)\right] \qquad (2.2)$$

The corrected lattice parameters were obtained by extrapolating to $f(\theta) = 0$.

2.9b The High Temperature Measurements

The alloys were cast in the arc-furnace in the form of cylindrical rods of ∿1 mm diameter for the Unicam high temperature camera. The surface of the specimen was cleaned before mounting it at the axis of the furnace. The furnace was evacuated by a rotary-diffusion pump combination to a pressure of better than 10^{-5} torr. The temperature of the furnace was controlled by a Eurotherm controller. The temperature of the specimen was raised very slowly to avoid possible contamination. Cu $K\alpha$ radiation was used.

CHAPTER 3

THE PHASE TRANSFORMATIONS IN La, Ce AND Pr

3.1 Introduction

In this chapter, the effects of temperature, pressure and alloying on the crystal structures of La, Ce and Pr will be outlined. As mentioned in the first chapter, the light rare earth elements have more complex crystal structures than the heavy rare earths. The common crystal structure of La, Ce and Pr at room temperature is the double-hexagonal close packed structure which is formed by stacking close-packed hexagonal layers in the sequence ABACABAC... . A drawing of the observed crystal structures for the rare earth elements is shown in Fig. 3.1. One can easily see that the atoms in the B and C layers have the same environment as does an atom in an hcp lattice. The atoms in the A layers have the same environment as does an atom in an fcc lattice. Thus there are two non-equivalent sites in the dhcp lattice which makes it unique among the rare earth crystal structures.

There are four atoms in the unit cell of the dhcp lattice. These are located at (0,0,0), $(\frac{1}{3},\frac{2}{3},\frac{1}{4})$, $(0,0,\frac{1}{2})$ and $(\frac{2}{3},\frac{1}{3},\frac{3}{4})$ where x,y,z are the fractional co-ordinates of the atoms (see Appendix 2). The crystal translational vector is $x\vec{a}_1 + y\vec{a}_2 + z\vec{a}_3$ where the $\vec{a}_i$ are the fundamental translation vectors of the lattice. These three vectors can be written in terms of the lattice constants a and c as follows:-

$$\vec{a}_1 = a\vec{i}$$

$$\vec{a}_2 = -\frac{1}{2}a\vec{i} + \frac{\sqrt{3}}{2}a\vec{j}$$

$$\vec{a}_3 = c\vec{k}$$

where $\vec{i}$, $\vec{j}$ and $\vec{k}$ are a set of orthonormal base vectors.

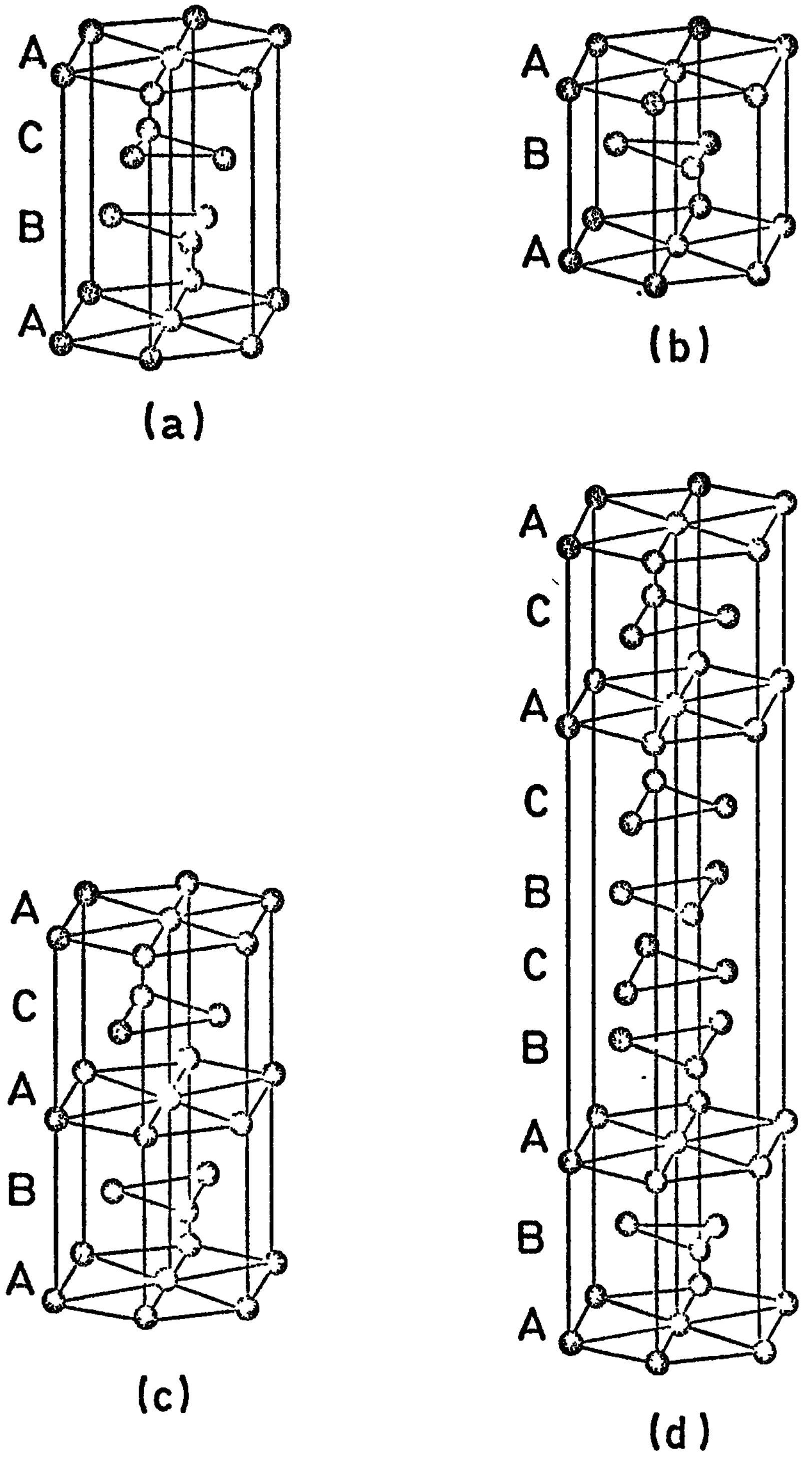

FIG. 3·1 The four close packed structures observed for the rare earth metals (a) fcc; (b) hcp; (c) dhcp; (d) Sm-type.

3.2 Lanthanum

The room temperature dhcp structure of Lanthanum (α - La) transforms to the fcc phase at approximately 322°C [Spedding, Daane, and Herrmann (1957), Zinov'ev, Gel'd, Morozova and Chuprikov (1974)]. In the present work, electrical resistivity measurements vs. temperature for La yielded two critical temperatures for the transformation, 315°C on heating and 225°C on cooling. The area of the hysteresis loop in the curve of resistivity vs. temperature seemed constant in La-Ce alloys up to 50% Ce concentration. The resistivity decrease during this transformation was about 3%. Spedding, Hanak and Daane (1961) found that the transformation of the dhcp structure to the fcc form was accompanied by a decrease of 0.5% in volume. This transition has also been detected by thermal expansion measurements of La at high temperature [Barson, Legvold and Spedding (1957)].

The fcc structure of Lanthanum (β- La) transforms to bcc structure at around 865°C with about a 10% rise in the resistivity. The atomic volumes of the three phases of La are shown in Fig. 3.2 [from Spedding et al (1961)].

Pressure induced phase transformation has been shown to occur in both the rare earth metals and the intra-rare earth alloys. See for example Klement and Jayaraman (1967). The P-T phase diagram is shown in Fig. 3.3a for La. The fcc-bcc transformation and the melting point temperatures increase with pressure. The volume decreases for the dhcp-fcc transitions induced by temperature and high pressure are close enough to assume that the transformations are identical.

3.3 Cerium

Cerium, the first metal of the 4f transition elements, has five different solid crystallographic phases. Because of the complex nature

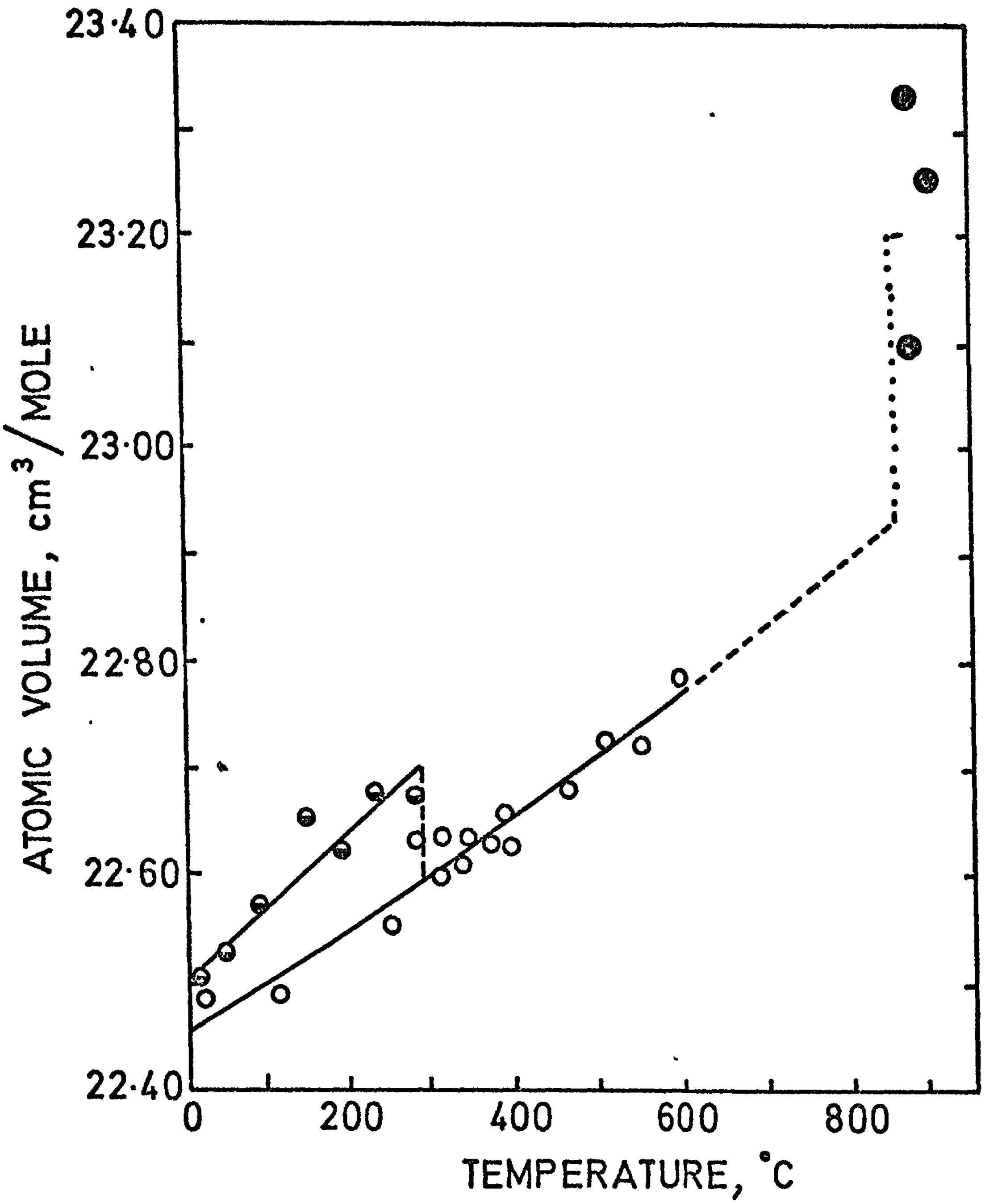

Fig. 3.2: Atomic volume vs. temperature plot for lanthanum, showing the three crystallographic forms: θ , hcp lattice; O, fcc lattice;, ●, bcc lattice [Spedding et al. 1961].

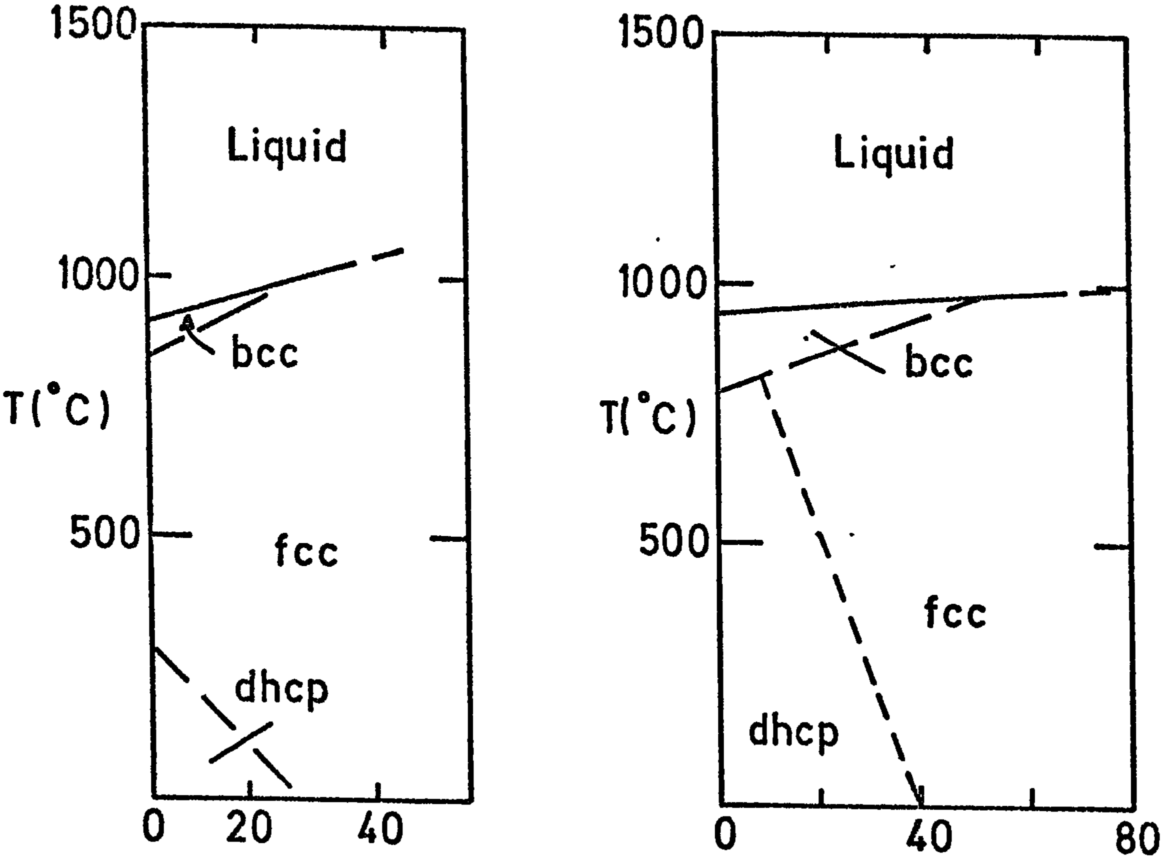

(a) La

(c) Pr

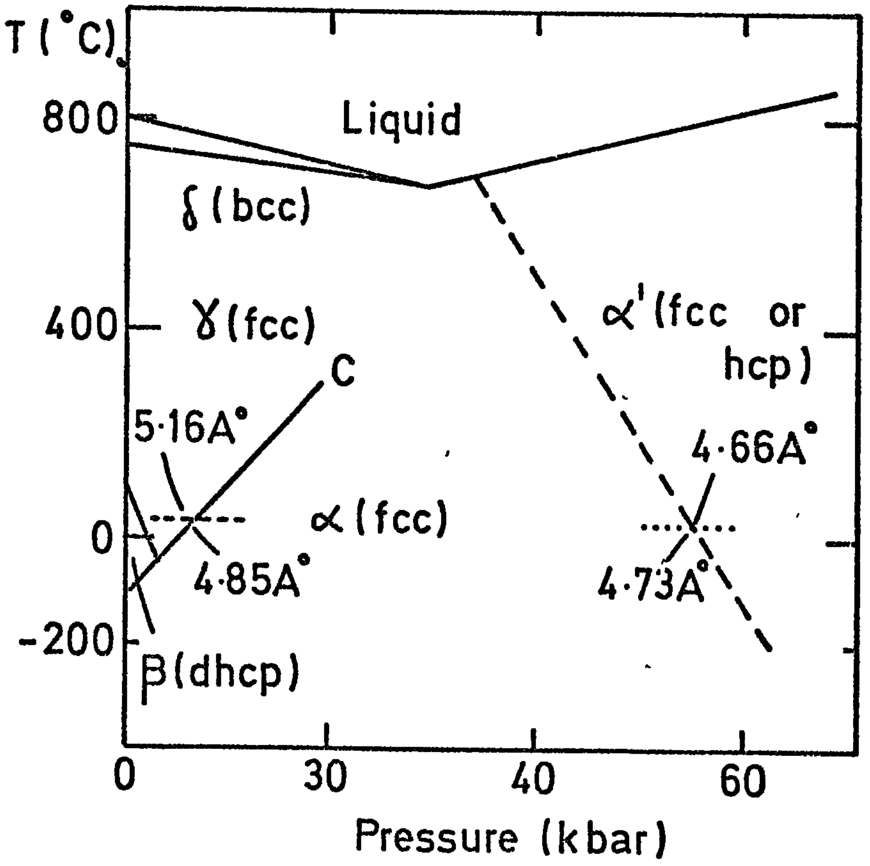

(b) Ce

Fig. 3.3: The p-T phase diagram of La, Pr, Ce [Klement and Jayaraman 1967]

of these structures, a great deal of effort has been given to understand this metal. Here, the information available in the literature will be given briefly. The crystal structure of Ce is fcc (γ- Ce) at room temperature when annealed at high temperature. The lattice parameter is a = 5.1612 Å [Gschneidner (1961)]. This structure starts transforming to dhcp cerium (β- Ce) just below room temperature. This transformation temperature is influenced by the thermal and mechanical history of the specimen [McHargue, Yakel, Jetter (1957)]. In the present work, as will be seen in Chapter 4, this transition began at about 10°C evidenced by the increase in the resistivity as the specimen was cooled down to liquid nitrogen temperature. This sample was annealed at 600°C for seven days. The β → γ- Ce transformation temperature was found to be 110°C when the specimen was heated up to 750°C. McHargue et al. found that the γ to β transformation does not occur isothermally and that the most favourable region of the β - Ce formation is 263 K - 230 K. From the sluggishness of the transition, it was concluded that the amount of β - Ce formed depended on the cooling rate, impurities, thermal cycles and cold work. For more information see Gschneidner (1961). The remainder of the room temperature γ - Ce transforms to the more dense fcc form (α - Ce) with a lattice parameter a = 4.85 Å around 100 K. It is also known that β - Ce transforms to α - Ce between 77 and 4.2 K.

Ce has two more solid phases bcc cerium (δ - Ce) above 730°C and α' - Ce above 50 k bar. The P-T phase diagram is shown in Fig. 3.3b. At room temperature and at a pressure of 7 k bar the lattice parameter of γ - Ce changes discontinuously from 5.16 Å to 4.85 Å for the α - Ce [Franceschi and Olcese (1969)]. This is the same α - Ce induced by lowering the temperature below 100 K at atmospheric pressure. The high pressure phase α' is stable above 50 k bar at room temperature.

Fcc [Franceschi and Olcese (1969)] and hcp [McWhan (1970)] structures have been reported for the α' - Ce phase. α' - Ce is superconductive below 1.8 K [Wittig (1968)] and the superconducting transition temperature decreases linearly with pressure.

The phase transition line between the γ and α phases ends in a critical point C corresponding to p_c = 17.5 - 20 k bar and T_c = 550 - 630 K [Beecroft and Swenson (1960), Ponyatovskii (1958), Jayaraman (1965)]. Thus it is possible to go continuously from the magnetic γ-phase to a more dense non-magnetic α phase.

The γ - Ce → β - Ce transformation has been explained in terms of the movement of certain planes of atoms [McHargue and Yakel (1960)]. This can explain why the favourable temperature range is 263 to 230 K for this γ - β transformation, because at low temperatures the driving force for this kind of transition gets smaller.

Several theories have been put forward to explain the $\gamma \rightleftarrows \alpha$ transition in Ce. The increase in density (decrease in volume) accompanying the γ → α transformation has been attributed to an electronic transition by Pauling (1950), and Zachariasen (1949). They suggested the promotion of one electron from an f orbital in the γ phase to an s - d hybridized conduction band orbital in the α phase, i.e. the electronic configuration of the Ce atom changed from $4f^1(sd)^3$ to $4f^o(sd)^4$ during the γ → α transition. Neutron diffraction data [Wilkinson et al (1961)] and Hall coefficient studies [Kevane, Legvold and Spedding (1953),,Likhter and Venttsel (1962)] are consistent with the presence of the localized magnetic moment in γ- Ce and zero magnetic moment in α - Ce. However, there is also evidence that the large volume change at the $\gamma \rightleftarrows \alpha$ transition corresponds to the transfer of less than one electron to the conduction band [Lock (1957), Gschneidner and Smoluchowski (1963)].

Gschneidner and Smoluchowski have found an effective valency of 3.06 ∓ 0.06 for γ and β phases at room temperature and 3.67 ∓ 0.09 for α - Ce at low temperatures. They have calculated these valencies, the exact values depending upon the temperature and pressure, from the metallic radii and magnetic data.

In support of the promotion of the 4f electron to the conduction band, Blandin and co-workers(1965), Coqblin and Blandin (1968) have proposed a model based on the hybridization of the f shell and the conduction band with a strong spin orbit interaction. In this model the localized f-like energy levels were assumed to be strong functions of temperature and pressure.

Ramirez and Falicov (1971) presented a somewhat different model for the $\gamma \rightleftarrows \alpha$ transition. They assumed both localized f states and itinerant conduction band states. They included the electron-electron matrix elements between f states and conduction band states in the calculations of the occupation probability of localized electrons in f states. This occupation number was found to be a function of temperature and pressure.

Two different types of electron states were assumed by Ramirez and Falicov (1971). (i) an extended band, obtained from hybridized s- and d-like Bloch states. They have assumed, for the sake of simplicity, a conduction band with a constant density of states of about 20 states/Ry atom and a total bandwidth W = 8.16 eV. In addition to this it was assumed that in the α phase at T = 0 there are four electrons per atom in the conduction band, and energies are measured from the Fermi energy $\varepsilon_F = 0$. Then the conduction bands extend from $-W_h = -2.72$ eV to $W_e = 5.44$ eV. (ii) Localized f-states. These states with an energy E (measured from $\varepsilon_F = 0$), being highly localized accept only one electron per atom. It was also assumed that the energy necessary in order to place a second electron in the same localized f states was infinite. The following figure shows a schematic diagram of the density of states of this model.

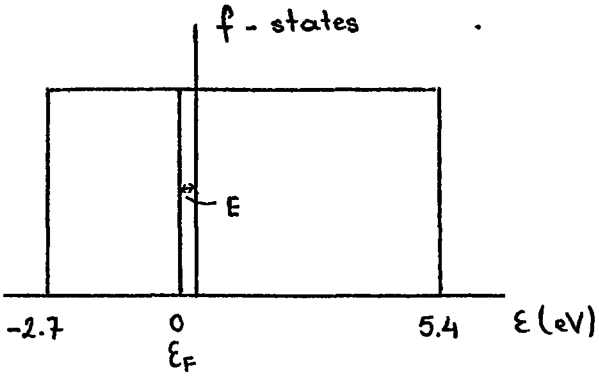

The quasiparticle excitations of the system are:

(i) Electron excitations in the conduction band with energies $0 \leqslant \varepsilon \leqslant W_e$

(ii) Hole excitations in the conduction band with energies $0 \geqslant \varepsilon \geqslant -W_h$

(iii) Localized electrons in the f shell, with energy $\varepsilon = E$.

After making several assumptions about the excitation energy of a given many-electron state, they have obtained the equilibrium values of the occupation functions $n_e(\varepsilon)$, $n_h(\varepsilon)$ and n_c for conduction electrons, conduction holes and localized electrons respectively as follows:

$$n_e(\varepsilon) = \left\{ a^{-1} \exp\left[(\varepsilon - E + 2Gn_c)/k_B T\right] + 1 \right\}^{-1} \tag{3.1}$$

$$n_h(\varepsilon) = \left\{ a \exp\left[(\varepsilon + E - 2Gn_c)/k_B T\right] + 1 \right\}^{-1} \tag{3.2}$$

where

$$a \equiv n_c / (2J+1)(1-n_c)$$

and

$$n_c = \frac{12\, k_B T}{W} \,\ell n \left| \frac{A_1 + e^{-Q_1}}{A_o + e^{-Q_o}} \; \frac{A_o + 1}{A_1 + 1} \right| \tag{3.3}$$

where

$$A_o = 1/A_1 \equiv a \exp\left[(E - 2Gn_c)/k_B T\right] ,$$

$$Q_o \equiv W_h/k_B T ,$$

$$Q_1 = W_e/k_B T \quad .$$

E is an energy difference between the energies of an f level and a hybridized s-d conduction band and varies appreciably with pressure. G represents the interaction between an electron in the f shell and a hole in a Wannier orbital. J is the angular momentum quantum number.

The occupation function of localized electrons given by equation 3.3 is shown in the figure on the right as a function of temperature. They have assumed the values of G and E as 0.44 eV and 0.1899 eV respectively. This curve shows critical behaviour corresponding to Ce at a critical pressure $P_c = 19.5$ k bar with a critical temperature T_c = 579 K (see Fig. 3.3b).

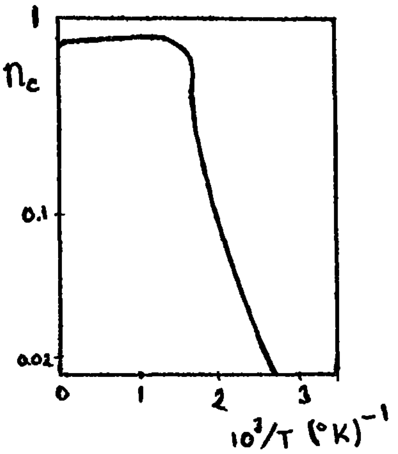

Therefore a relationship between transition temperatures and transition pressures might be found by varying E.

The number of conduction electrons per Ce ion is given by

$$n(p.T) = 4 - n_c(p.T) \qquad (3.4)$$

Ramirez and Falicov have also presented several points to improve this method.

1. A more realistic density of state function D(ε).
2. A hybridization term, mixing f and conduction band states can be included.
3. Interactions between itinerant quasiparticles should be taken into account.

The difference between the model by Coqblin and Blandin (1968) and Ramirez and Falicov (1971) is the treatment of the secondary effects accompanying to the promotion of 4f electron.

In connection with the α-γ transition in cerium, Johansson (1974) has recently argued that this is a Mott transition of the 4f state. γ-Ce is on the low density side of a Mott transition with the localized nature of its 4f electron. He argues for an itinerant behaviour of the 4f electron in the α phase which is assumed on the high density side of Mott transition (i.e. 4f band states). This localization-delocalization transition of the 4f state has been put forward by discussing the inter-atomic interactions and the general behaviour of cohesive energies of the elements. Therefore he rejects any promotion type model for the γ-α transition in cerium. He points out that, in the α' phase the 4f band becomes sufficiently broad to permit the observed superconductivity.

3.4 Phase Stability in Ce and its alloys

Considering the five different allotropic forms of Ce one can examine the effects of impurity, thermal treatment, cold work and alloying on the stability of these phases. Several investigations have been carried out to clarify these points. Gschneidner et al (1962) have investigated the effects of total impurity content on the $\alpha \rightleftarrows \gamma$ transformation. They have also discussed the effect of cycling on the formation of β phase. This is shown in Fig. 3.4. Dillamore, Harris and Smallman (1964) have shown that deformation, created by decreasing the thickness more than 70% by rolling, caused partial transformation of γ to β-Ce. They interpreted this result to indicate a nearly zero stacking-fault energy for γ-Ce.

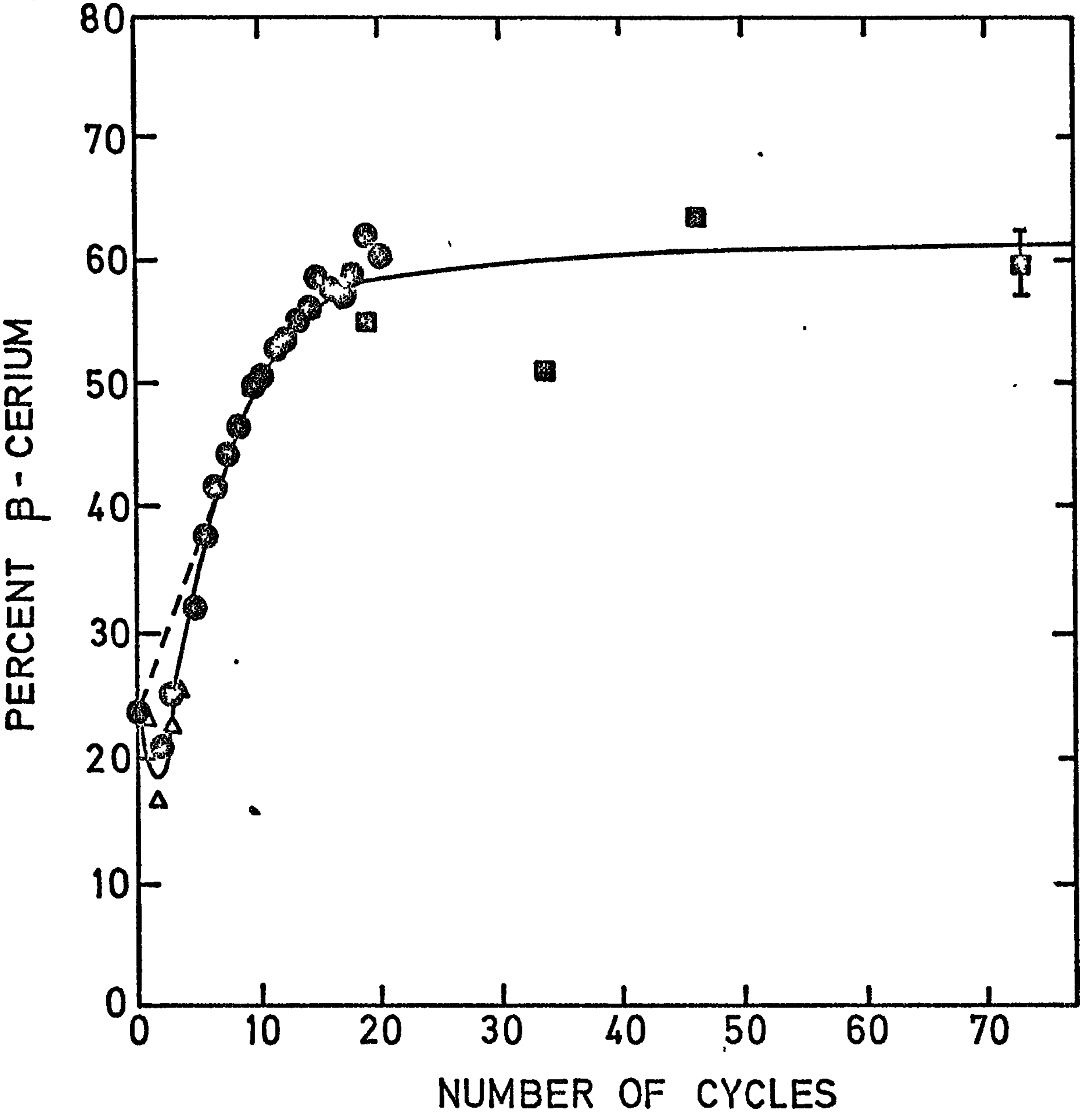

Fig. 3.4: Effect of cycling on the amount of β-cerium present in the sample. ● Dilatometric data; Δ dilatometric data for a second Ce sample from the same manufacturer, ■ X-ray data. [Gschneidner et al. 1962].

Otte and Chessin (1965) have observed the formation of extrinsic stacking faults[†] by deforming Ce at room temperature. The stacking sequence is ABCABCABC... for fcc γ-Ce and ABACABAC... for dhcp, β-Ce. Thus, deformation of γ-Ce at room temperature will cause extrinsic faults, which are regions of ABAC stacking (i.e. ABC[ABAC]ABC...). That is why it is generally believed that the formation of β by thermal cycling is related to the deformation and faulting in γ-Ce during the γ → β transformation.

Clinard (1967) has shown that some rare earth solutes in Ce enhance β formation. Two graphs from his work are presented in Fig.3.5. From this resistivity data he showed that the amount of dhcp β-phase formed at low temperatures was maximum for Ce-2 at.% La and Ce-2 at.% Lu, minimum with those rare earths near Gadolinium except for Eu. The presence of β phase is evidenced by a steep rise in the resistivity vs. temperature curves around 12 K which is associated with the paramagnetic antiferromagnetic transition [Wilkinson (1961)].

3.5 Praseodymium

The room temperature structure of Pr is double-hexagonal close packed (α-Pr) with lattice parameters of a = 3.6721 ± 3 Å and c = 11.8330 ± 6 Å [Beaudry and Palmer (1974)]. Neutron diffraction work on polycrystalline samples has shown that α-Pr is antiferromagnetic below 25 K [Cable et al (1964)]. Bucher and co-workers (1969) reported that they were able to retain the high temperature fcc phase of polycrystalline Praseodymium (β-Pr) at room temperature and below by

---

[†] The insertion of an extra close-packed layer of atoms [Howie and Valdre (1963)]

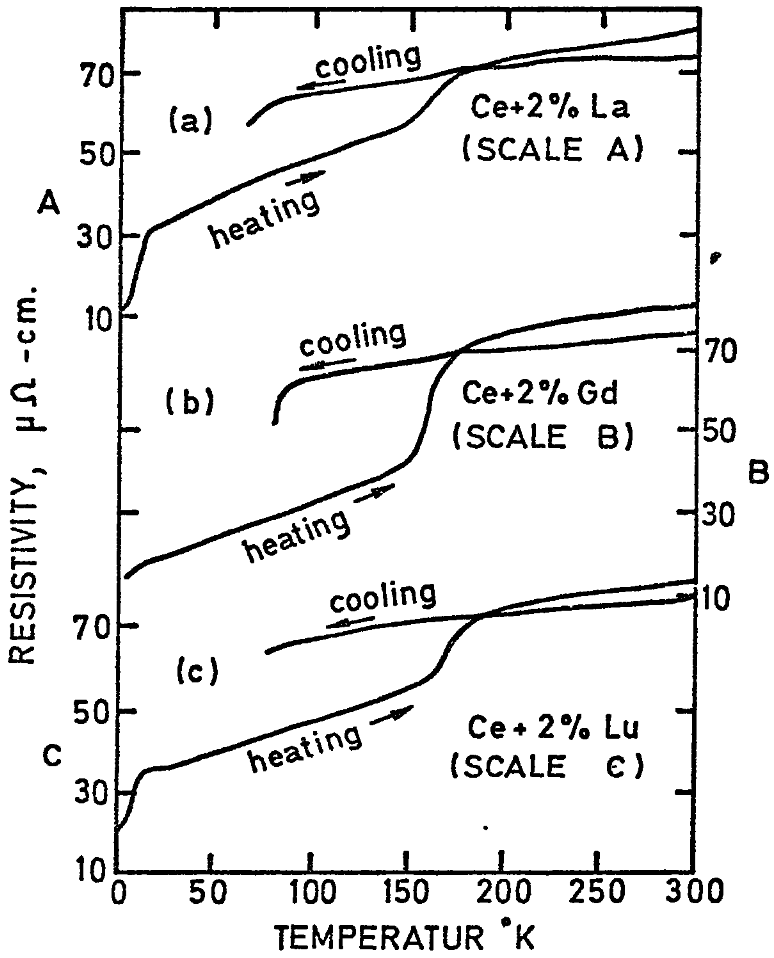

Fig. 3.5a: Resistivity vs. temperature curves between room temperature and 1.5 K for three cerium alloys in the annealed condition [Clinard 1967].

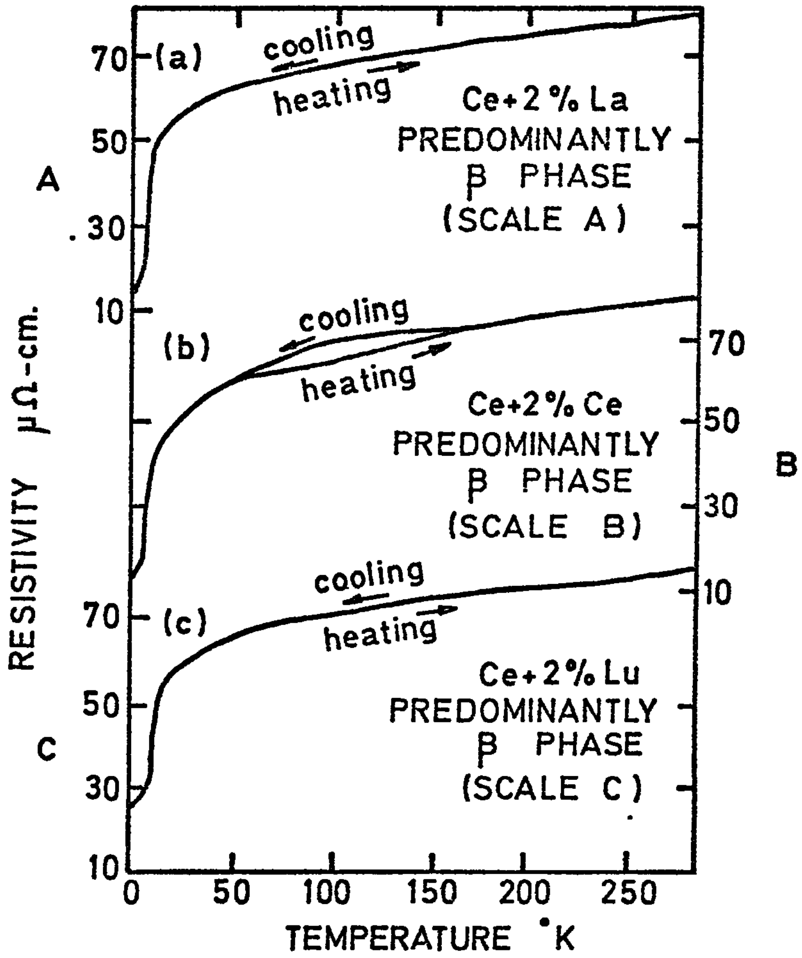

Fig. 3.5b: Resistivity vs. temperature curves between room temperature and 1.5 K for three cerium alloys after repeated thermal cyling to convert them to β phase.

quenching in the arc-furnace. They found a ferromagnetic transition in this metastable structure at 8.7 K. It was mentioned that when samples which had been quenched were subsequently heated to temperatures greater than 560°C partial conversion to the dhcp phase took place. They could not detect the dhcp-fcc transition by means of differential thermal analysis (D.T.A.) suggesting that it could be a sluggish one in their high purity Pr. This metastable fcc Pr has also been observed electrically by Meaden, Sze, Krithivas and Zuckermann (1971).

Pr transforms to bcc (γ-Pr) at high temperatures. In the present work, this transformation was found to be at 795°C from resistivity measurements which is in good agreement with Spedding et al (1957). But Bucher et al (1969) have found 860°C as a fcc-bcc transformation temperature in their two high purity samples and 792°C in the less pure Pr by means of differential thermal analysis (DTA). Meaden et al. (1971) have reported 855 ± 1°C for this β-γ transition in Pr without its dependence on impurities.

Piermarini and Weir (1964) have found the fcc structure (β-Pr) at pressures above 40 k bar at room temperatures. But this fcc phase has not been detected in the high pressure work by Stephens (1965). A P-T phase diagram for Pr is shown in Fig. 3.3c. The change in the slope of the dhcp-bcc transition line was interpreted as the meeting point of the dhcp-fcc boundary line. The triple point co-ordinates for fcc-bcc-liquid and dhcp-fcc-bcc are (48 k bar, 938°C) and ($\sim$8 k bar, $\sim$810°C) respectively [Jayaraman (1965)].

The lattice parameter was found to be 5.18 Å for temperature induced fcc Pr at room temperature [Bucher et al (1969)] which is higher than one would extrapolate from data concerning the Th-Pr (fcc) system [Norman, Harris, Raynor (1966)].

3.6 Crystal structure sequence in rare earth metals and intra-rare earth alloy systems

On the basis of pressure induced phase transition experiments, Jayaraman and Sherwood (1964) showed that in rare earth metals transitions between different phases were in the order hcp—Sm-type—dhcp—fcc with increasing pressure in the trivalent rare earth metals. If h represents the hcp lattice (stacking sequence ABAB...) and c represents the cubic structure (stacking sequence ABCABC) then the sequence of structures becomes:

(hhh...) - (hhchhc...) - (hchc...) - (cccc...)

i.e. $\text{hcp} — \frac{2}{3}\,\text{hcp}\,\frac{1}{3}\,\text{fcc} — \frac{1}{2}\,\text{hcp}\,\frac{1}{2}\,\text{fcc} — \text{fcc}$

This means that the amount of fcc layering is increasing according to this sequence [Taylor and Darby (1972)].

It can be seen that the observed structure sequence in intra-rare earth alloys is fcc — dhcp — Sm-type — hcp. This is just the opposite direction of the pressure induced structure sequence mentioned above which indicates that the effect of pressure acted in the same way as the addition of a light rare earth to a heavy rare earth. Thus, when a light rare earth such as Ce is alloyed with a heavy rare earth, such as Gd, the structure sequence at room temperature is fcc — dhcp — Sm-type — hcp with increasing gadolinium [Burov, Terekhova and Savistskii (1963)].

Several workers have investigated the relation between the structure sequence and either the atomic size or c/a ratio. Harris and Raynor (1969) considered the correlation between c/a ratios and structure types as a function of atomic number. This is shown in Fig. 3.6. From this figure one should be able to predict the structure of a given intra-rare earth alloy by calculating its "average" atomic

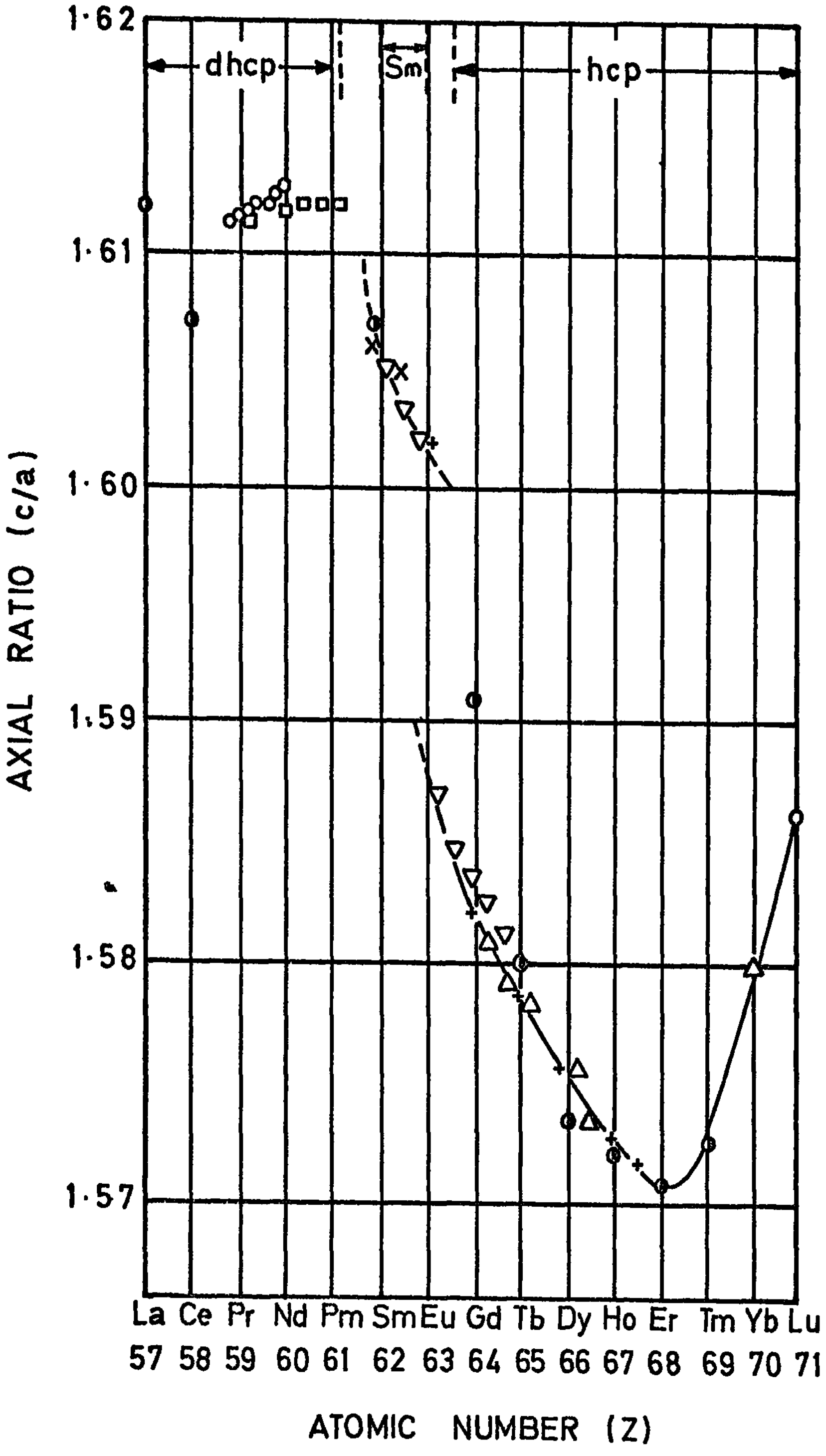

Fig. 3.6: The variation of axial ratio with atomic number of the pure rare earth metals and of some cerium - rare earth alloys. [Harris and Raynor 1969]

◐	Pure rare earth	X	Ce-Gd alloys
▲	Lu - 7.7 at.% Ce alloy	▽	Ce-Tb alloys
⊙	Ce-Nd alloys	△	Ce-Ho alloys
⊡	Ce-Sm alloys	+	Ce-Er alloys

number by considering the composition. Since the c/a ratio does not change much with pressure, the above method of determining the phase cannot be a useful criterion [McWhan and Stevens (1967)].

Although it was mentioned in the first chapter that the wave functions for the 4f electrons are nearly zero beyond half the nearest neighbour distance, it has been suggested that at least a fraction of 4f electrons take part in the bonding in the rare earth metals. The light rare earths are known to possess larger extension in their 4f orbitals than the heavy rare earth metals because of the lanthanide contraction. The contribution of 4f electrons in the bonding will be expected to decrease with increasing atomic number because the amount of decrease of the metallic radius across the series is less than that of 4f radius.

Considering the decrease in the metallic radius with pressure, McWhan and Stevens (1965) suggested that the sequence of crystal structures formed at high pressure could be explained by the decrease in the localization of the 4f electrons with increasing pressure. Because, the participation of 4f electrons in the bonding will be increased with increasing pressure of the metals and alloys.

In support of this idea, Gschneidner and Valletta (1968) have calculated the ratio of metallic radius to 4f radius for the rare earth metals. They explained the structure sequences induced by temperature and pressure by the variation of this parameter in metals and alloys. The variation of the four crystal structures of the rare earth metal and alloys as a function of the metallic to 4f radius ratio is shown in Fig. 3.7 which is taken from their paper. From the figure, one can see that the radius ratio is about 3.25 for the fcc — dhcp phase boundary, 3.6 for the dhcp — Sm-type boundary and 3.65 for the Sm-type — hcp phase boundary. This is in good agreement with experimental data.

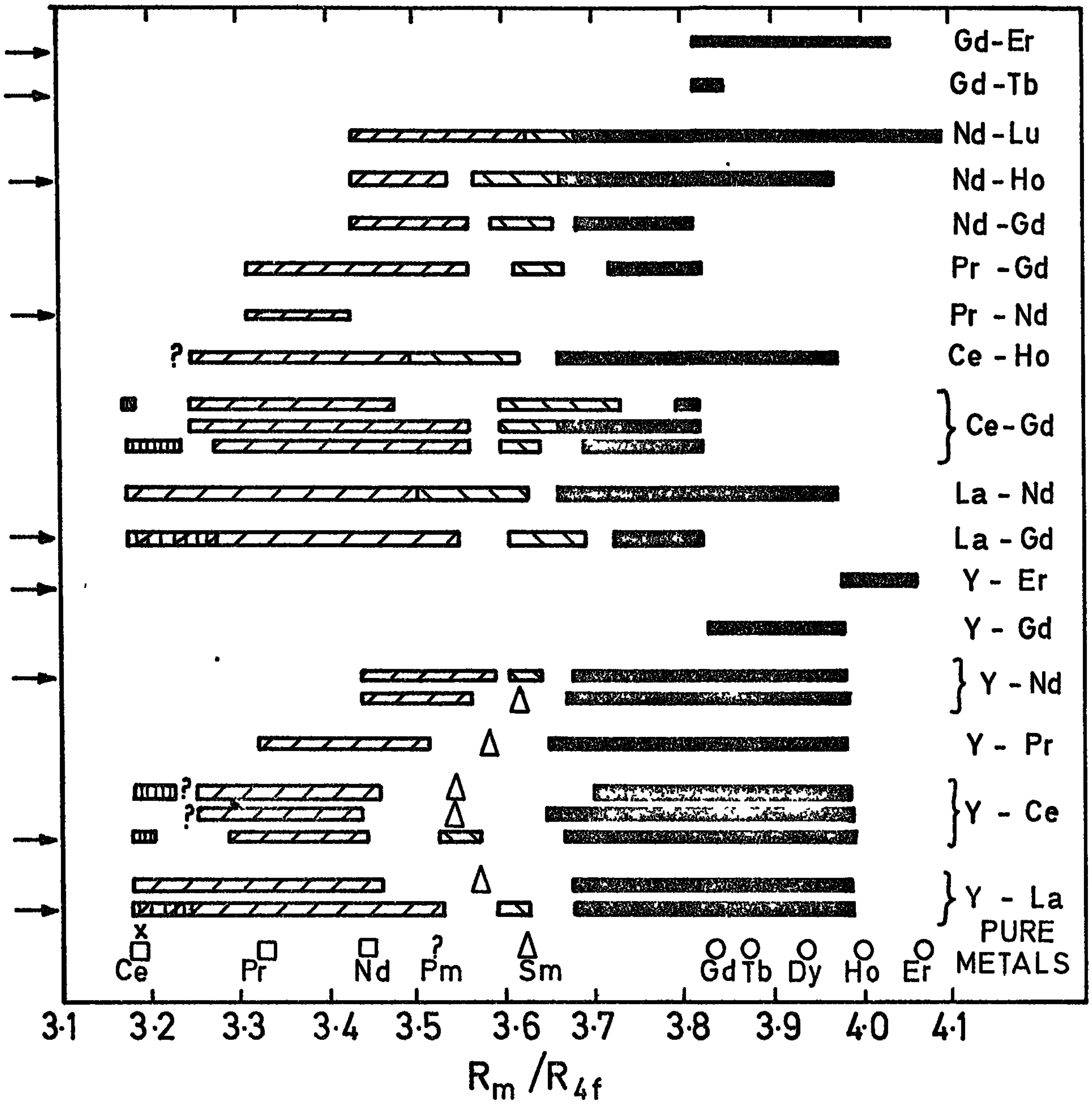

FIG.3·7 The variation of the four metallic crystal structures of the rare earth metals and alloys as a function of the metallic to 4f radius ratio. fcc. x ▥ ; dhcp. □, ▨ ; Sm-type Δ, ▧ ; and hcp. ○, ▩
(Gschneidner and Valetta, 1968)

In order to explain the crystal structure sequence at high pressures they made the following assumption:

1. the 4f radius is independent of pressure,

2. the metallic radius decreases with increase of pressure which was calculated from the known compressibility data. The high pressure data are shown in Fig. 3.8. It can be seen that the dhcp → fcc transformation of Pr and Nd agree well with the dhcp - fcc phase boundary obtained from alloying data. Thus one can conclude from this classification of the experimental data that at least a small fraction of 4f electrons contributes to the bonding and therefore has a stabilizing effect on the various close-packed phases, particularly fcc.

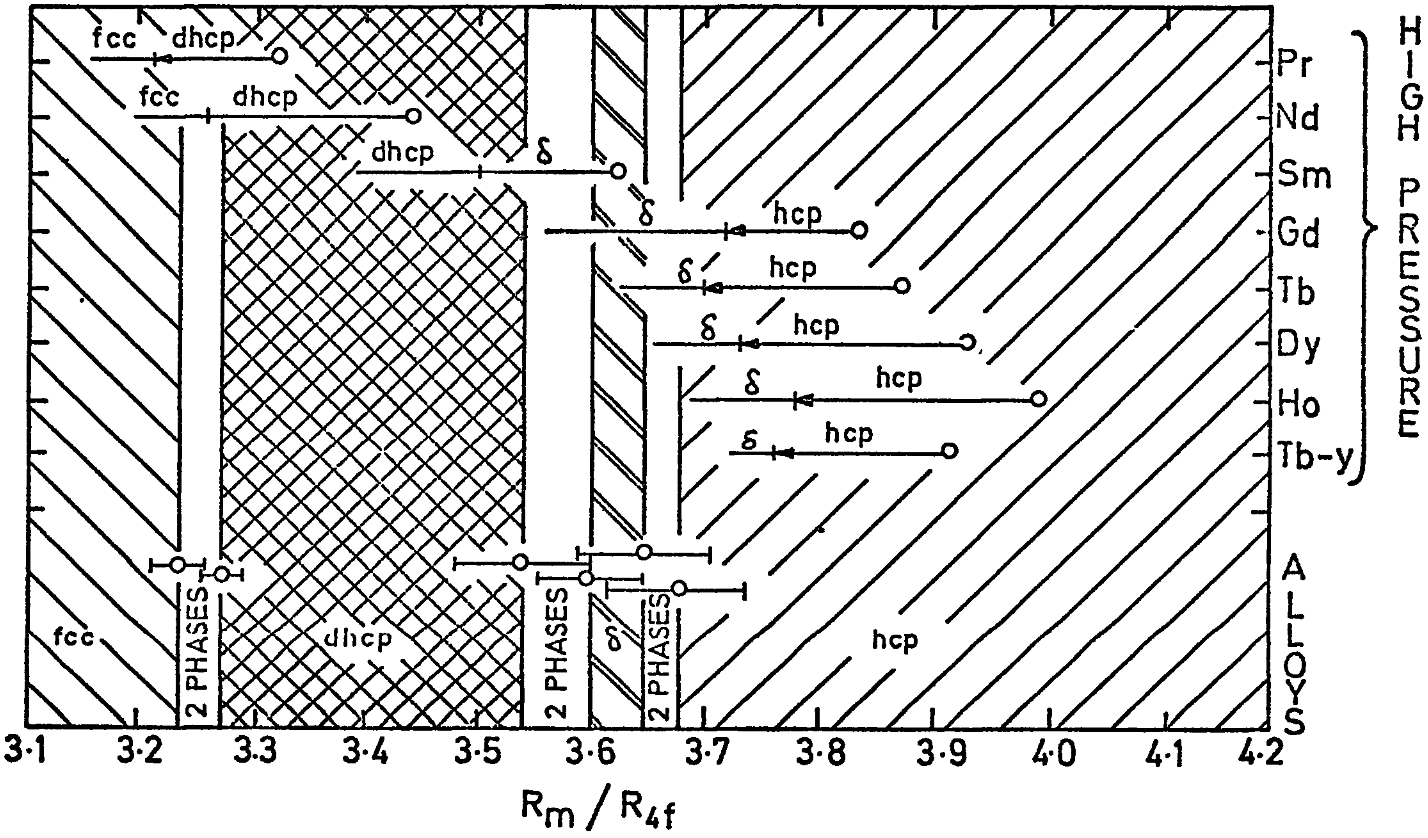

Fig. 3.8: Comparison of the intra-rare earth alloy correlation with the variation of the high pressure polymorphic structures as a function of the metallic to 4f radius ratio. The data points for the alloys indicate the average value of the phase boundaries. The error bar indicates the deviation from the average value. The open circle for the high pressure materials indicates the radius ratio value for the atmospheric pressure form. The short vertical line intersection the horizontal lines indicates the radius ratio value at which the high-pressure polymorphic transformation occurs. [Gschneidner and Valetta 1968].

CHAPTER 4

RESULTS AND DISCUSSION OF STRUCTURAL PROPERTIES OF PR-Ce ALLOY

Essentially nothing has been published concerning the phase relationships in the Pr-Ce system. This is mainly due to the expected similarity in the phase diagrams between Pr-Ce and other intra-light rare earth binary alloys (i.e. La-Nd, Ce-Nd...) . The first detailed investigation of structural properties of the Pr-Ce alloys was carried out by Harris in Birmingham University. In order to determine the phase boundaries of this system, it was thought that further information might be obtained from resistivity data, since the formation of a new phase will, in most cases, be evidenced by a change in slope in the resistivity vs. temperature curves.

Measurements of the electrical resistivity of Pr-Ce alloys have been carried out in the temperature range 1.3 K to 1100 K and the results are shown in Fig. 4.1 for the high temperature region. These curves present two types of anomaly, the negative and positive steps in ρ (T) associated with structural phase transformations and a considerable nonlinearity (convex upwards). A similar departure from linearity has been observed particularly in light rare earth metals and explained by anomalous variation of the phonon resistivity (Meaden 1972).

The electrical resistivity curves for most of the alloys seemed to be more or less linear with temperature in the initial heating run and the resistivity values were lower than those obtained on cooling. The cooling curves which showed the nonlinearity characteristic of the light rare earths were reproducible in the second thermal cycle. The increase of resistivity on thermal cycling is in contrast to what one would expect from a process involving the relief of strains incurred during the specimen preparation (i.e. cutting from the annealed bulk, polishing and spot-welding).

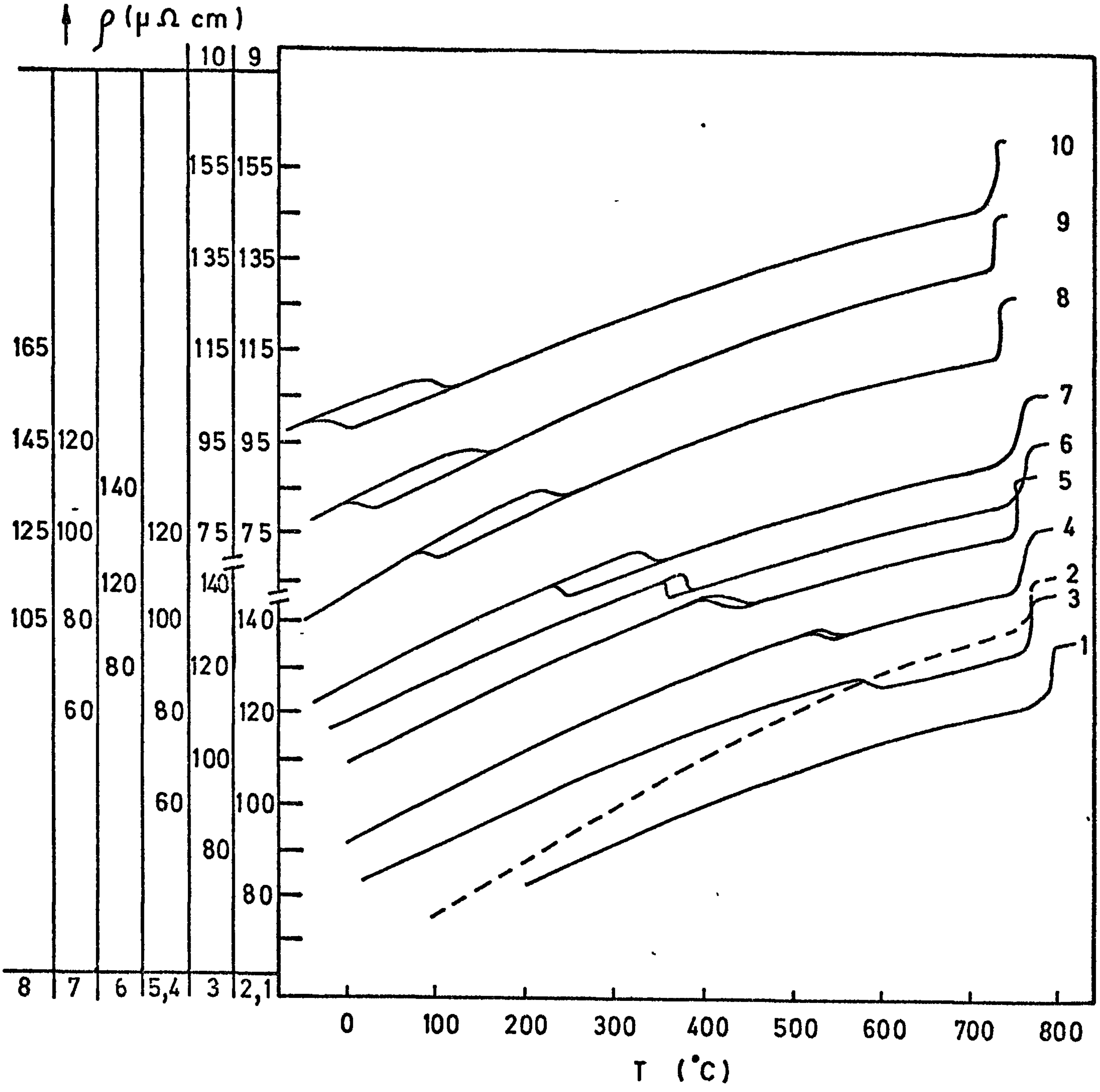

Fig. 4.1: The resistivity of Pr-Ce alloys at high temperature [1, pure Pr; 2, 8 at.% Ce; 3, 10 at.%; 4, 15 at.%; 5, 30 at.%; 6, 40 at.%; 7, 50 at.%; 8, 80 at.%; 9, 95 at.%; 10, pure Ce].

It is clear from Fig. 4.1 that Pr and $Pr_{.92}Ce_{.08}$ show only one phase transformation (dhcp - bcc) but that the other alloys and pure Ce exhibit two transitions with an increasing hysteresis loop as Ce concentration increases (i.e. dhcp - fcc and fcc - bcc). The resistivity decreased about 3% in the case of the proposed dhcp - fcc transition. In the case of the fcc - bcc or dhcp - bcc transition, the increase in the resistivity was about 10% which is in good agreement with the reported data of Spedding et al (1957). These steps for two different transitions seemed constant (within the experimental error) across the alloys. (Error bars calculated from the scatter of the observed dimensional data are typically of the order of 2%). Table 4.1 shows the structural transition temperatures for the Pr-Ce system obtained from examination of the resistivity vs. temperature curves.

Table 4.2: The γ ⇄ β-Ce transformation temperatures in Ce

γ → β-Ce	β → γ-Ce	Hysteresis	Purity (a/o)	Reference
-23° ± 3°C	168° ± 7°C	191°C	99.53	Gschneidner et al (1962)
10° C	100°C	110°C	98.967	McHargue and Yakel (1960)
10° ∓ 5°C	100° ∓ 5°C	100°C	99.9	Present data
1° ± 3°C	81° ± 7°C	80°C	96.41	Gschneidner et al (1962)

The γ ⇄ β-Ce transition temperatures for two cerium samples at different purity were investigated by Gschneidner et al (1962) and shown in Table 4.2 with the available data from the other sources. These figures show that the presence of impurity decreases the hysteresis between the γ → β and β → γ transformation temperatures in cerium, i.e. the higher the purity of the Ce the larger is the hysteresis between the β → γ and γ → β transformations. Gschneidner et al (1962) have also

Table 4.1: The structure transformation temperatures in PrCe system obtained from the resistivity vs. temperature curves.

Alloy	dhcp → fcc	fcc → dhcp	Hysteresis dhcp ⇄ fcc	fcc ⇄ bcc	dhcp ⇄ bcc
Pr					795°C
$Pr_{.92}Ce_{.08}$					775
$Pr_{.90}Ce_{.10}$	600°C		-	755°C	
$Pr_{.85}Ce_{.15}$	535	545°C	10°C	765	
$Pr_{.70}Ce_{.30}$	415	435	20	760	
$Pr_{.60}Ce_{.40}$	380	365	15	770	
$Pr_{.50}Ce_{.50}$	335	255	80	765	
$Pr_{.20}Ce_{.80}$	225	105	120	740	
$Pr_{.05}Ce_{.95}$	125	35	90	738	
Pure Ce	110	10	100	735	

investigated the pressure dependence of the $\gamma \rightleftarrows \beta$-Ce hysteresis and found that the hysteresis loop does not change much but shifts to lower temperatures.

In the case of Pr-Ce alloys, the addition of Pr to Ce up to 20 at.% does not change the area of the hysteresis loop significantly but shifts it to the higher temperatures (Fig. 4.1). For concentrations more than 50 at.% Pr in Ce, the hysteresis loop decreases with increasing amounts of Pr and vanishes in the $Pr_{.90}Ce_{.10}$ alloy at around 600°C. Further increase of Pr causes the disappearance of the dhcp $\rightleftarrows$ fcc transition.

In view of the existence of metastable fcc-Pr at high temperatures (see Chapter 3.3), one would expect to see evidence of this dhcp $\rightleftarrows$ fcc transition at concentrations more than 90 at.% Pr in Pr-Ce alloys and even in pure praseodymium. It is tempting to postulate a relation, if any, between the area of hysteresis loop and the driving force for the dhcp $\rightleftarrows$ fcc transformation. In line with this, one can conclude that the driving energy for this transformation decreases towards the Pr end. This point will be discussed later in this chapter in the light of x-ray data.

The values for the lattice parameters a, c, axial ratio and atomic volume determined by means of x-ray powder-diffraction by Harris are listed in Table 4.3. These values were obtained at room temperature after rapid cooling of the filings from the annealing temperature of 600°C. The lattice parameter against composition curves in the fcc phase and the dhcp phase are shown in Fig. 4.2 and Fig. 4.3 respectively. The atomic volume vs. composition is plotted in Fig. 4.4.

The initial investigation of Gschneidner, Elliott and Prince (1962) showed that the lattice constants follow Vegard's linear approximation

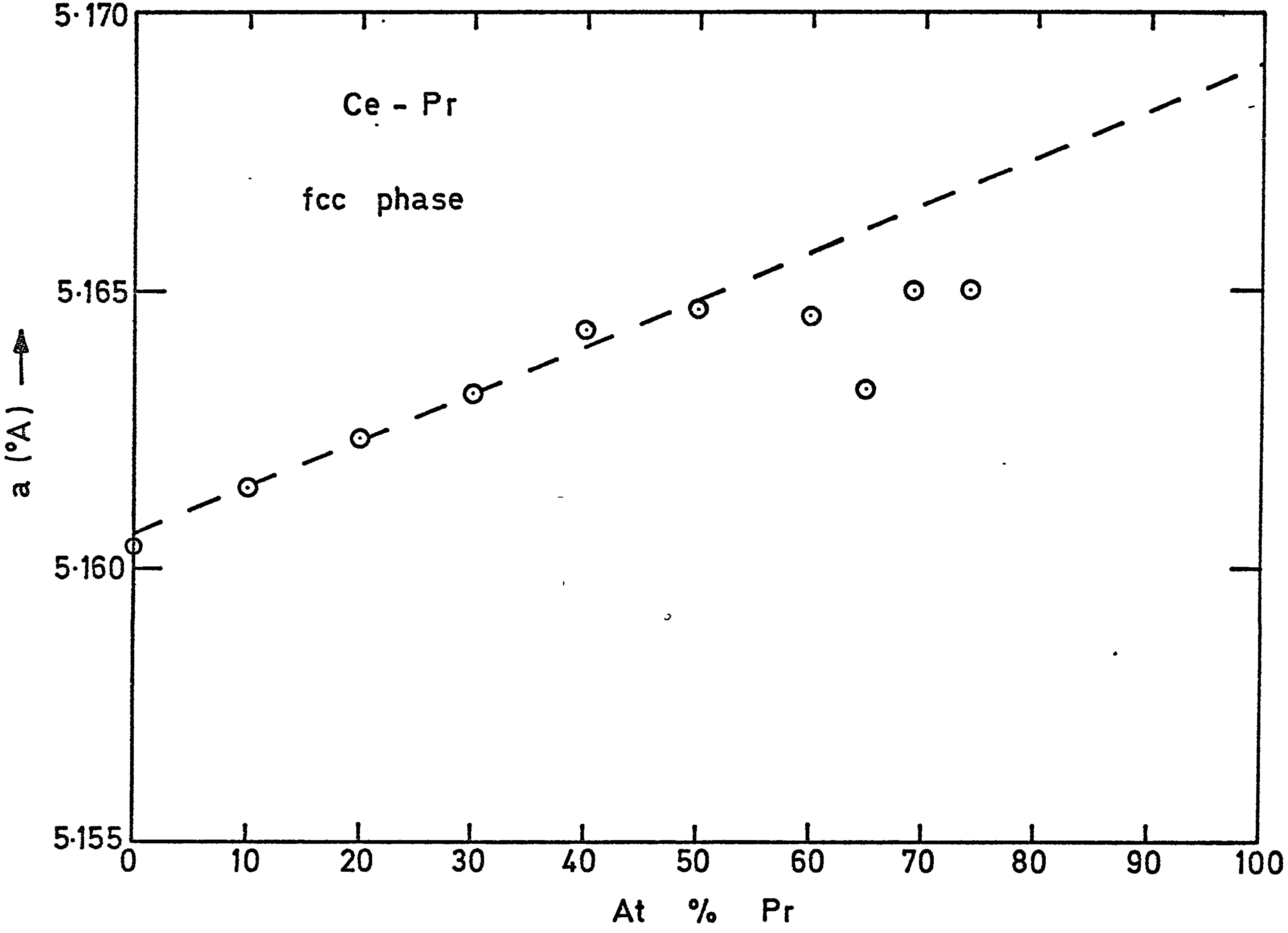

Fig. 4.2: The lattice parameter against composition in the fcc phase

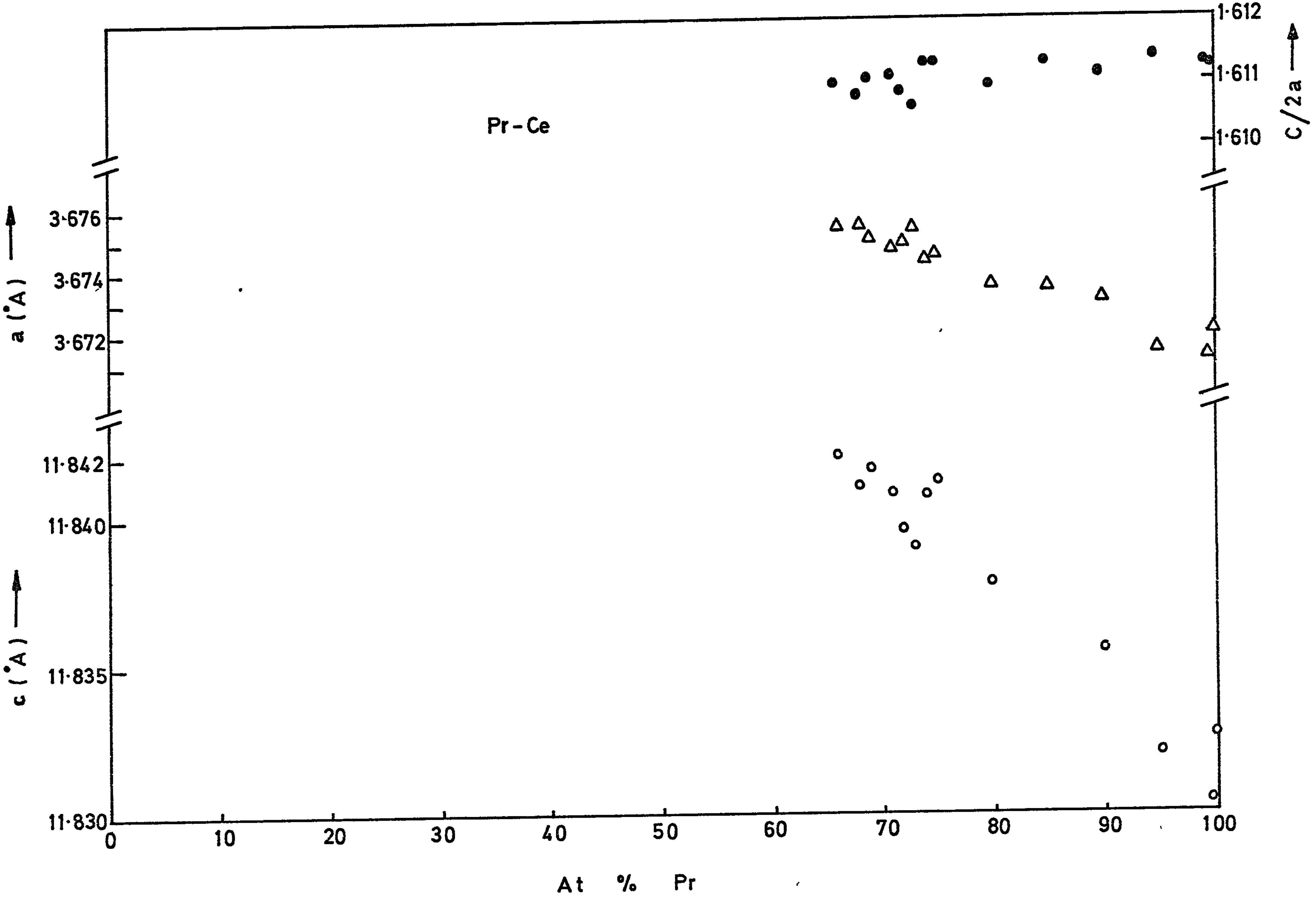

Fig. 4.3: The lattice parameters against composition in the dhcp phase

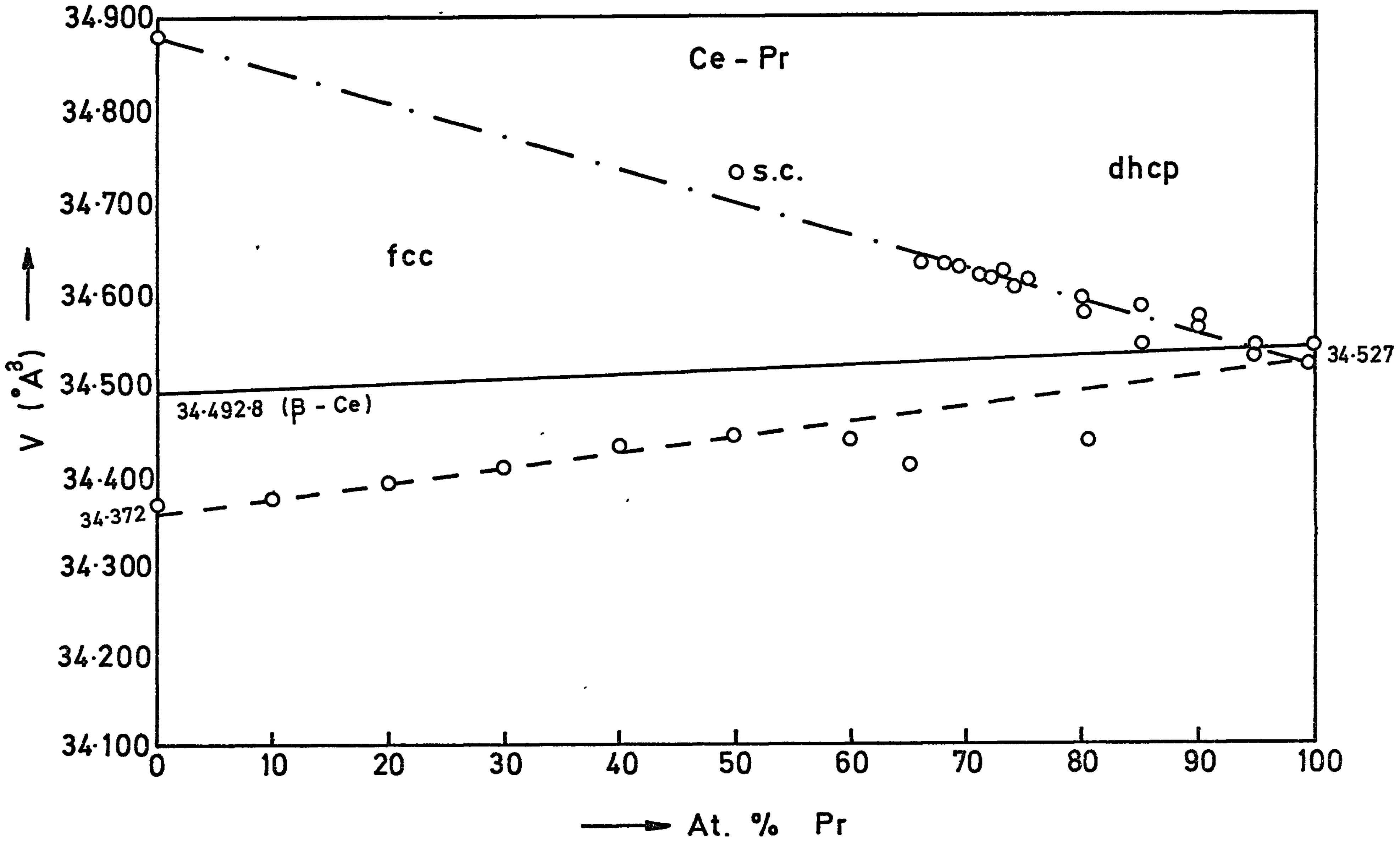

Fig. 4.4: The atomic volume against composition

Table 4.3: The lattice parameters of Pr-Ce system determined by Harris, I. R.

Praseodymium - Cerium Lattice Parameters of Main Phases						
Atomic % Pr	Double - hexagonal				Face - centred	
	a(°A)	c(°A)	c/a	Atomic Volume (°A^3)	a(°A)	Atomic Volume (°A^3)
0					5.15200	34.18751
10					5.16143	34.37559
20					5.16231	34.39317
30					5.16315	34.40997
40					5.1643	34.43296
50					5.16446	34.44016
60					5.16451	34.43716
65					5.1632	34.41096
66	3.67539	11.84195	3.22196	34.63387	N.M.†	
68	3.67544	11.84098	3.22165	34.63254	N.M.	
69	3.67502	11.84153	3.22217	34.62622	5.165	34.44697
71	3.67467	11.84077	3.22227	34.61741	N.M.	
72	3.67487	11.83951	3.22175	34.61750	N.M.	
73	3.67527	11.83889	3.22123	34.62322	N.M.	
74	3.67428	11.84065	3.22258	34.60970	5.165	34.44697
75	3.67442	11.84110	3.22258	34.61366	-	
80	3.67344	11.83566	3.22196	34.57961	-	
85	3.67339	11.83777	3.22258	34.58452	-	
90	3.67300	11.83541	3.22227	34.57030	-	
(-196°C) 90	3.67200	11.8338	3.22227	34.55620	-	
95	3.67135	11.83199	3.22279	34.52926	-	
99.5	3.67110	11.83042	3.22258	34.51999	-	
100	3.67192	11.83269	3.22248	34.54204	-	

†not measured.

up to 5 at.% Pr addition to Ce. (i.e. The lattice constants of solid solutions vary linearly with composition). In Fig. 4.2 it is seen that the lattice constant of Ce increases almost linearly by the solid solution of praseodymium up to Pr concentration of 50.% and then decreases with increasing Pr content when the fcc phase becomes unstable. The double-hexagonal solid solution of Ce in Pr becomes more stable with further increase of Pr. Atomic volume vs. composition curve (Fig. 4.4) indicates that the phase boundary between fcc and dhcp is approximately 67 at.% Pr.

Norman, Harris, Raynor (1966) found an extensive solid solution in the Th-Pr system in which the structures involved are the same as those in the Ce-Pr system. The stable fcc solid solution extended from thorium to 96 at.% Pr. They extrapolated the lattice constant vs. composition curve for Th-Pr alloys to 100 at.% Pr and found 5.15940 Å for the lattice constant of the hypothetical fcc form of praseodymium. This is identical within the experimental error with the lattice constant of γ-Ce (5.16120 Å). The relative volume change between the atomic volume of the double-hexagonal form of praseodymium and the hypothetical face-centered form was found to be 0.4% by the same group.

In the case of the Ce-Pr system, the linear extrapolation of the lattice constant vs. composition curve (Fig. 4.2) in the fcc phase to 100 at.% Pr gives a value of 5.169 Å for the lattice constant of a hypothetical fcc form of Pr. This is somewhat higher than that obtained from the Th-Pr system. A lattice constant of 5.18 Å (determined from flakes which had been splat cooled) for the fcc Pr was given by Bucher et al (1969) which is the highest value among the available data for the fcc form of Pr. This difference is unlikely to be due to a change in the electronic structure of Pr [Norman et al (1966)].

In the dhcp phase of the Ce-Pr system, the atomic volumes of the alloys increases linearly with increasing cerium up to the phase boundary at approximately 67 at.% Pr and fall sharply to the values in the fcc phase. The extrapolation of the linear part of the curve to 100 at.% gives 34.88 $\mathring{A}^3$ which is 1% higher than the atomic volume of β-Ce (34,49218 $\mathring{A}^3$). This positive deviation from the line connecting the atomic volumes of dhcp-Pr and dhcp-Ce is quite similar to the situation in the Ce-Nd system [Speight, Harris, Raynor (1968)]. However, in the Pr-Nd system [Lundin, Nachman, Yamamoto (1963)] have found complete solid solubility and no deviation from the line joining the atomic volumes of Pr and Nd. In view of these three systems, the positive deviation of the atomic volumes of the Pr-Ce alloy could be due to the change of effective valency of Ce from 3.1 to 3 as suggested by Speight et al (1968) for the Ce-Nd system, the atomic diameter of 3-valent cerium being larger than that of β-Ce of 3.1.

Now if we extrapolate the atomic volumes of Ce-Pr alloys in the fcc phase to 100 at.% Pr, 34,527 $\mathring{A}^3$ will be obtained for the atomic volume of the hypothetical fcc Pr. This is almost identical to the atomic volume of dhcp Pr (34,54204 $\mathring{A}^3$) within the experimental and extrapolation errors. So the relative difference between the atomic volume of the dhcp Pr and the hypothetical fcc form is considerably less than that value of 0.4% obtained from the Th-Pr system [Norman et al (1966)].

The similarity between the atomic volumes of dhcp Pr and fcc Pr and the disappearance of dhcp-fcc transition in the Pr-Ce system containing more than 90 at.% Pr, leads one to conclude that there must be a delicate relationship in favour of the dhcp phase towards the Pr end. (i.e. The free energy of the observed double-hexagonal form of Pr must be only slightly lower than that for a hypothetical face-centered form of Pr).

THE EFFECT OF SLOW COOLING OF FILINGS ON THE POSITION OF THE dhcp-fcc PHASE BOUNDARY

It can be seen from the examination of the resistivity data (Fig. 4.1) that Pr and Pr-Ce alloys containing cerium up to a concentration of 80 at.% do have dhcp structure at room temperature. This contradicts what has been said about the dhcp-fcc phase boundary in the Pr-Ce system based on the atomic volume data. However, it must be borne in mind that the lattice parameters were determined from filings which were rapidly cooled from 600°C to room temperature. It should be noted that this procedure is not a proper quenching to obtain the high temperature phases at room temperature; nor is it the proper treatment of the filings to investigate the phase relations in Pr-Ce alloys at room temperature. This is because of the phase transitions occurring below the annealing temperature of 600°C in most of the Pr-Ce alloys.

Therefore it was decided to determine the lattice parameters of some Pr-Ce alloys from the filings which were homogenized at 650°C and cooled down to room temperature at a rate of 1°C min^{-1}. It was observed that the phase boundary tends to shift towards the lower concentrations of Pr in the system. The x-ray powder photograph of $Pr_{.50}Ce_{.50}$ showed predominantly the dhcp form with some cubic lines. The atomic volume of this alloy was found to be 34.73039 $°A^3$ which is in good agreement with expected phase of this alloy considering its resistivity behaviour at high temperatures. The atomic volume of this alloy is marked as s.c. (slow cooled) in Fig. 4.4. It should be noted that $Ce_{.80}Pr_{.20}$ is fcc, despite the expected existence of a dhcp phase from the resistivity data, therefore one is forced to conclude that the transition towards the cerium end evidenced by the resistivity data is a partial one rather than a 100% transformation from dhcp to fcc or vice versa.

In an attempt to identify the high temperature fcc phase of $Pr_{.85}Ce_{.15}$, some x-ray powder diffraction photographs were obtained at 650°C by means of a high temperature camera. The pattern was found to be characteristic of a fcc structure for this temperature and the structure converted to dhcp when the specimen cooled down to room temperature. This is in good agreement with the resistivity data which indicated that the dhcp-fcc transition occurred at around 540°C. It was not possible to measure the lattice parameter accurately due to inadequate quality of the films for Bragg angles approaching 90°. Therefore, there is no information about the volume change accompanying the dhcp-fcc transition.

CALCULATION OF THE POSITION OF THE PHASE BOUNDARY IN THE Pr-Ce SYSTEM BY THE RADIUS RATIO METHOD

In view of partial participation of the 4f electrons in the bonding of the rare earth metals and alloys, we might be able to calculate the approximate phase boundary of Pr-Ce alloys by means of the relation between radius ratio and crystal structure sequence in rare earth given by Gschneidner and Valetta (1968) , (see Chapter 3.6). The calculated 4f radius and the metallic radius to 4f radius ratios for cerium and praseodymium are given in Table 4.3.

Table 4.3: The 4f radius and radius ratios

Rare earth Metals	4f radius (°A)	Metallic to 4f radius ratio
Ce	0.580	3.18
Pr	0.551	3.32

The radius ratio values for the Pr-Ce alloys were obtained by summing the products of the mole fraction and radius ratio of Pr and Ce which make up the alloys, i.e. for $Pr_{1-x}Ce_x$, the radius ratio is

$$\left(\frac{R_M}{R_{4f}}\right)_{Pr_{1-x}Ce_x} = \left(\frac{R_M}{R_{4f}}\right)_{Pr} (1-x) + \left(\frac{R_M}{R_{4f}}\, x\right)_{Ce} \qquad (4.1)$$

The calculated radius ratios for a number of Pr-Ce alloys are given in Table 4.4.

Table 4.4: The radius ratios of some Pr-Ce alloys

Alloys	Metallic to 4f radius ratio	Alloys	Metallic to 4f radius ratio
Pr	3,32	$Pr_{.60}Ce_{.40}$	3.26
$Pr_{.90}Ce.10$	3.31	$Pr_{.50}Ce_{.50}$	3.25
$Pr_{.85}Ce_{.15}$	3.30	$Pr_{.30}Ce_{.70}$	3.22
$Pr_{.70}Ce_{.30}$	3.28	$Pr_{.10}Ce_{.90}$	3.19
$Pr_{.65}Ce_{.35}$	3.27		

According to the classification of Gschneidner and Valetta (1968), the regions of existence for fcc and dhcp phases are listed in Table 4.5. From the examination of the calculated radius ratios for the alloys, one can deduce that the dhcp-fcc transition boundary can occur at any concentration of cerium between 15 at.% and 40 at.%. Bearing in mind the somewhat arbitrary method of calculating the radius ratios for the alloys, the determination of the dhcp-fcc phase boundary cannot be as reliable as the other methods.

Table 4.5: Regions of existence for dhcp and fcc phases

Phase	R_M/R_{4f} Radius Ratio	
	Lower Limit	Upper Limit
fcc	< 3.18	3.24 ± 0.03
dhcp	3.28 ± 0.02	3.54 ± 0.06

PHASE DIAGRAM

So far the dhcp ⇄ fcc phase transition in the Pr-Ce alloys and the absence of this transition in pure praseodymium were discussed on the basis of electrical and x-ray diffraction data. Because of the close similarity of these two elements (electronic structure, atomic diameter, valency effect etc.) and the possibility of having a metastable fcc praseodymium, it was expected that there was a high probability of forming complete solid solutions in the solid state. However this does not appear to be in the Pr-Ce system as discussed in the earlier sections.

Despite having very little information on the phase boundaries in the solid state for the Pr-Ce alloys, it would be a useful step to propose a phase diagram for this system. The transition temperatures obtained from the resistivity data (Fig. 4.1) are plotted against composition in Fig. 4.5. The error in the determination of the dhcp ⇄ fcc transition temperatures is estimated to be about $\pm 7^{o}$C and in the case of the fcc ⇄ bcc, $\pm 3^{o}$C from several runs on the same specimen. This is because of the sensitivity of the transition temperatures to the heating and cooling rates. The hysteresis loop for the dhcp ⇄ fcc transition decreases with increasing praseodymium concentration and vanishes beyond 90 at.% Pr indicating that pure praseodymium does not transform to fcc structure.

In the Lanthanum-Cerium alloys the hysteresis loop for dhcp ⇄ fcc transition seemed to be more or less constant which is evident from the electrical resistivity of La-Ce alloys up to 50 at.% cerium (Fig. 4.6). This is in good agreement with the phase diagram of the La-Ce system [Gschneidner (1961)].

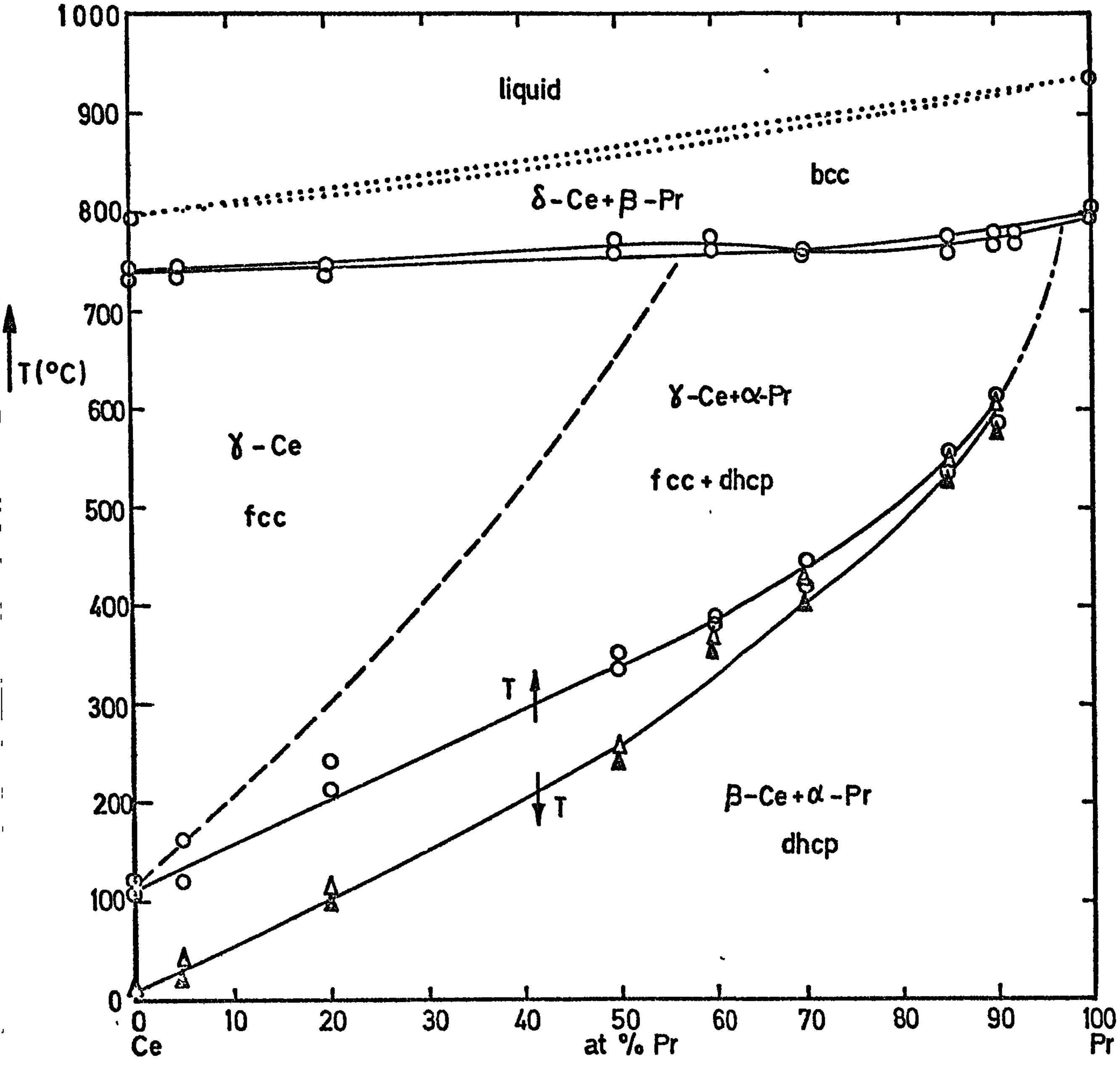

Fig. 4·5. Phase diagram of Pr - Ce system.

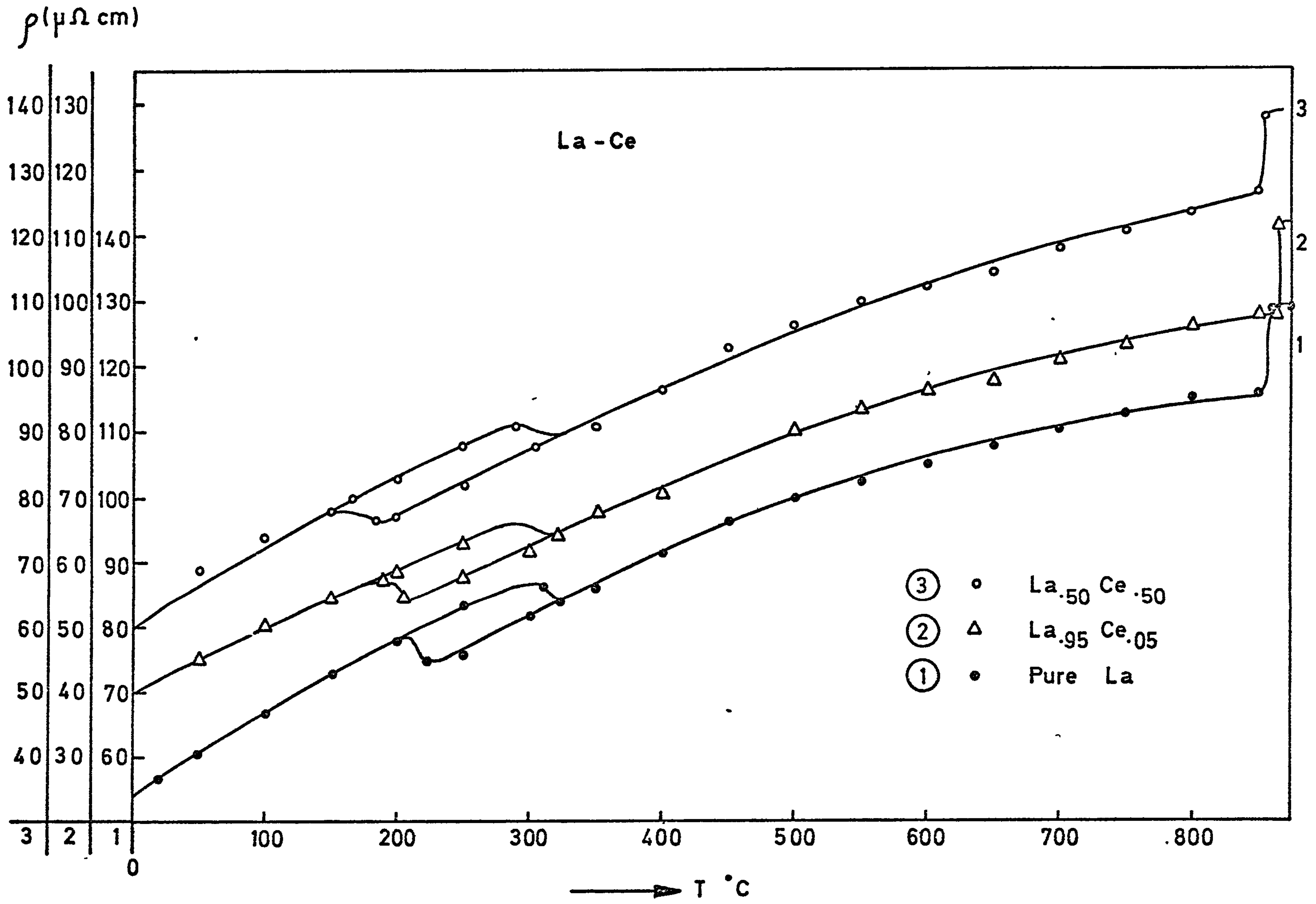

FIG. 4·6. The resistivity of La - Ce alloys against temperature.

A proposed phase diagram for the Pr-Ce system is sketched in Fig. 4.5. The δ-Ce (bcc), β-Pr (bcc) solid solution decomposes eutectoidally at around 760°C with γ-Ce (fcc) forming a closed field, the approximate position of its boundary being shown by a broken line, and β-Ce (dhcp) and α-Pr (dhcp) forming a complete solid solution below 110°C. The position of the boundary between the mixed phase and the dhcp regions appears to depend on the direction in which the temperature is changed. This type of construction emphasizes that the so-called dhcp $\rightleftarrows$ fcc transition in the alloys is a partial one rather than 100% transition as discussed earlier. Although the x-ray pattern of the $Pr_{.85}Ce_{.15}$ alloy at 650°C was predominantly fcc, the extra faint dhcp lines might support the above notion.

In fact this diagram is in good agreement with the high pressure diagram for praseodymium (Fig. 3.3c). The thing to note from this p-T diagram is that it indicates no fcc phase at high temperatures and atmospheric pressure in praseodymium. It is obvious that one needs a combination of metallographic, thermal, x-ray diffraction, density electrical resistivity etc. data to delineate the phase boundaries in the solid and liquid state of the system.

Lastly, mention must be made of the close similarity between the proposed phase diagram for the Pr-Ce system and the La-Nd phase diagram given by Gschneidner (1961).

CHAPTER 5

5.1 The formation of Magnetic Moments and the Kondo Effect

In this chapter, a brief summary of the physical concepts related to the formation of magnetic moments in metals and some of their properties (the Kondo effect) will be given. The literature is extensive and many of the recent theories involve sophisticated calculations.

The main question is this, "What are the conditions under which the transition metal impurity atom may retain its magnetic moment in a nonmagnetic host metal?" An isolated atom generally has a spin and orbital angular momentum according to Hund's rules. If the perturbation that acts in a metal on the impurity atom is not strong, the impurity atom may retain the magnetic moment which existed in free space.

Friedel (1958) introduced the concept of a virtually bound state for impurities by considering the bandwidths of the free electron states in metals. This virtually bound state is strongly admixed with the free electron states of the host metal. Such a state is not localized in the strict sense since it has a finite energy width.

As an example of the nearly localized impurity state let us consider a potential shown in Fig. 5.1.

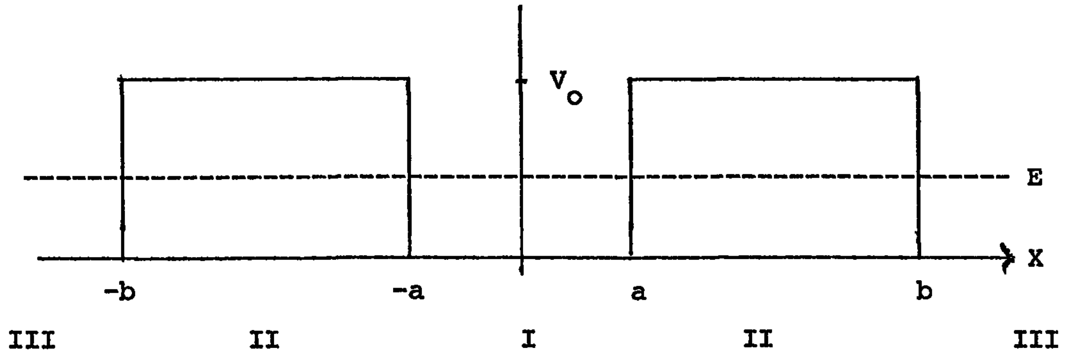

Fig.5.1: A one-dimensional square well potential.

The solution is expressed by $\psi = \cos kx$, $(E = \hbar^2k^2/2m_o$ in region I and by $\psi = A \exp(k_1x) + B \exp(-k_1x)$, $V_o - E = \hbar^2k^2/2m_o$ in region II for $E < V_o$. A and B are determined by the continuity condition at $x = \pm a$. In region III, the solution is expressed by $\psi = C \cos kx + D \sin kx$. C and D are also determined by the continuity condition at $x = \pm b$. When $k_1(b-a) \gg 1$ i.e. region II is sufficiently large

$$C^2 + D^2 \cong (V_o/E) \cosh^2 \left[k_1(b-a)\right] . \left[\cos ka - (k/k_1) \sin ka\right]^2 \qquad (5.1)$$

when the condition

$$\cos ka = \left(\frac{k}{k_1}\right) \sin ka \qquad (5.2)$$

is satisfied, the wave function is largest in the region of the potential well. Equation 5.2 determines the discrete energy levels in the potential well. One may consider that region I corresponds to the impurity atom and region III to the host metal. It is expected that the level in the perturbed lattice will be deviated from the pure Bloch orbital and concentrated around the impurity. This is the state called a virtually bound state. Region II allows the electrons to tunnel from region I to region III or vice versa (Kondo 1969).

It would be useful to look at the effect of impurity on the electronic properties of the material. Imagine that a transition metal impurity ion is placed in a noble metal, i.e. CuFe or CuMn. Suppose for the moment that the broad s-band is completely absent, so we consider only the behaviour of electronic states in the d-band. The effect of the s-electrons will be considered later. The host matrix has been idealized to the point where the electrons move in a single, narrow d band of width W., In the case of large lattice constant, each unit cell of the host has a single Wannier state characterized by an energy ε_o. In the impurity cell, an electron has an energy $E_d = \varepsilon_o + V_I$. The density of states of this idealized system is given below (Mills 1972).

$$\rho_A(\varepsilon) = (N-1)\ \delta(\varepsilon - \varepsilon_o) + \delta\ (\varepsilon - E_d) \qquad (5.3)$$

If the energy difference V_I satisfies the condition $V_I > W/2$, then the impurity level will remain outside the d-band of the host. The density of states of this simple model is given in Fig. 5.2a. Now if we superimpose on this picture the density of states of the s-electrons, the impurity level at E_d will fall within the s-band so long as V_I is not extremely large. This is shown in Fig. 5.2b. A given electron in the impurity level is free to move into the conduction band of the material. Thus, the impurity state acquires a finite lifetime ($\tau = \hbar/\Delta$). In this case, the contribution to the density of states from the life time broadened impurity level may be written as (Anderson 1961)

$$\rho_d(\varepsilon) = \frac{1}{2\pi} \frac{\Delta}{(\varepsilon - E_d)^2 + (\frac{\Delta}{2})^2} \qquad (5.4)$$

Δ, the width of the virtual level is given by

$$\Delta = \pi\ |V|^2\ N_s(\varepsilon) \qquad (5.5)$$

where V is the matrix element that describes the amplitude for the electron to hop from the impurity level into the conduction band. It is this mixing interaction which broadens the localized state into a virtual state. $N_s(\varepsilon)$ is the total s-electron density of states.

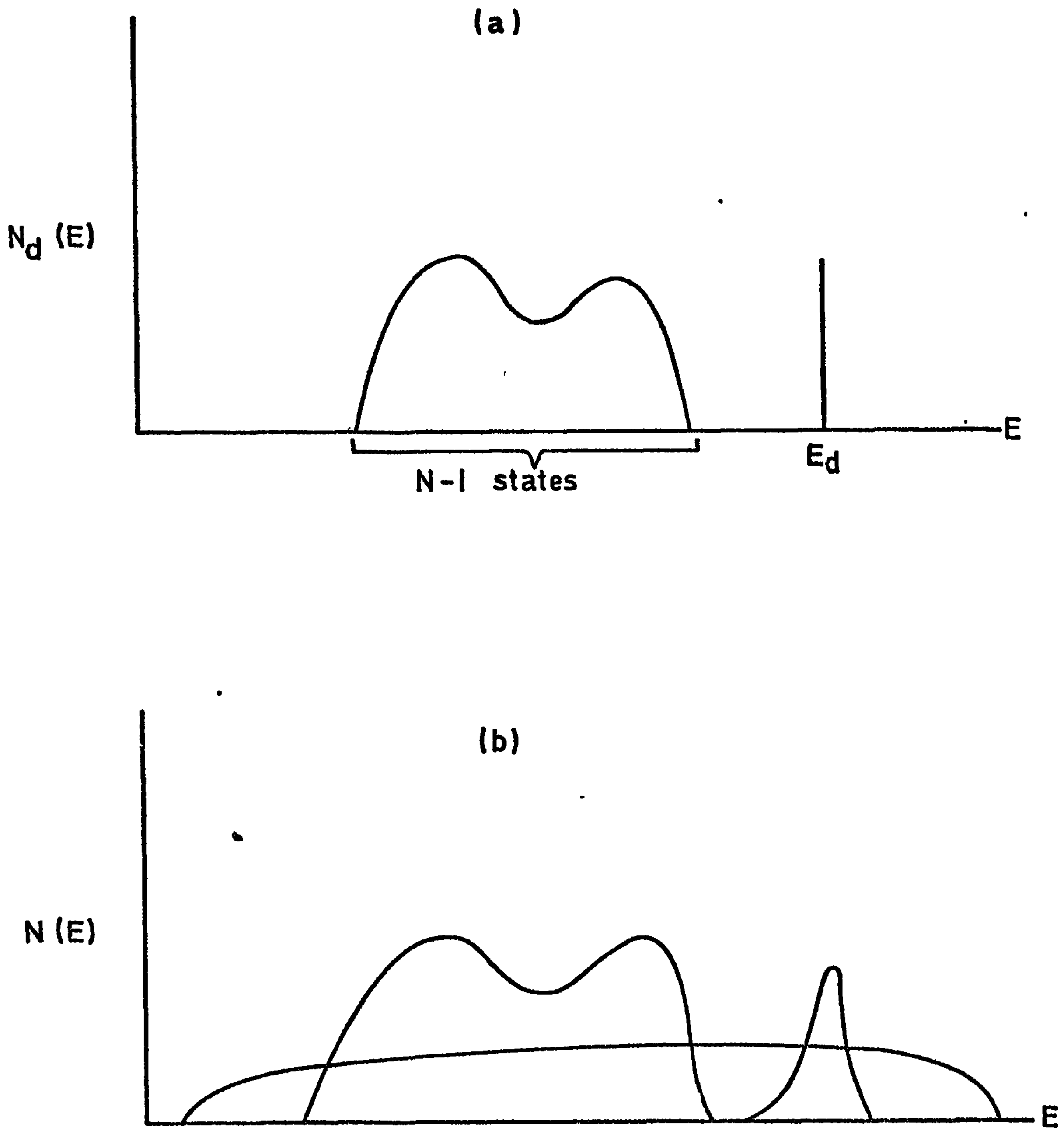

Fig.5.2: (a) Schematic illustration of the effect of a repulsive impurity potential on the density of states of a metal.

(b) The effect of the presence of the s-band is to broaden out the discrete peak at E_d in Figure (a) into a virtual level (D.L. Mills 1972).

If one alloys a given host with a sequence of impurities, the virtual level shifts its position in Fig. 5.2b. When it coincides with the Fermi energy, the electronic density of states of the alloy becomes very large. The increase in density of states has important effects on the magnetic contribution to the resistivity of the alloy as well as the specific heat and Pauli spin susceptibility. The magnetic contribution to the resistivity arises because the conduction electron is scattered strongly by the impurity when the virtual level lies close to the Fermi level. The above properties can be explained in terms of the effect of the magnetic impurities on the electronic density of states within the framework of one electron theory. This picture needs modifications as soon as electron-electron interactions are introduced.

So far, the localized electronic states of the impurity have been described in terms of virtual bound states. In the Hartree-Fock theory of atoms, the Coulomb interactions between electrons play the primary role in providing an atom with a magnetic moment. Similarly, as pointed out by Friedel (1958), the Coulomb interaction between two electrons in the virtual level can produce a localized magnetic moment at the impurity site.

The total contribution of the Coulomb interaction to the energy of the system is $U < n\downarrow > < n\uparrow >$ in the Hartree-Fock picture. $< n\downarrow >$ and $< n\uparrow >$ are the number of electrons with spin down and spin up respectively in the virtual level, and U is the strength of the intra atomic Coulomb interaction. By making a state with

$$< n\downarrow > \neq < n\uparrow > \qquad (5.6)$$

the Coulomb energy of the system is reduced. But this unbalance in the spin density will increase the kinetic energy of the system. It can be shown that when

$$U \rho_I (E_F) > 1 \qquad (5.7)$$

the gain in kinetic energy will be smaller than the saving in Coulomb energy, and a state with the virtual level spin polarized lies lowest in energy. In other words, one can divide the impurities into magnetic and nonmagnetic according to the ratio of the two parameters U and the width Δ of the impurity states. The region of validity of the Hartree-Fock approximation for magnetic moment formation is limited as

$$\frac{U}{\Delta} > 1 \qquad (5.8)$$

In this region a given electron remains localized on the site for a relatively long time while tending to keep other electrons away via the Coulomb interaction and thereby forms a moment. Friedel (1958) described this moment formation qualitatively and Anderson (1961) introduced the mathematical formalism. The above description of the moment formation is incomplete, because it omits the time scale over which a moment exists (Heeger 1969).

The existence of magnetic moments in dilute alloys can be understood experimentally if the impurity contribution to the susceptibility is temperature dependent in the form of a Curie-Weiss law. Impurities which do not possess magnetic moment have temperature independent susceptibility at low temperatures. The second experimental evidence for the existence of magnetic moments is obtained from the resistance minimum phenomenon observed in dilute alloys. Sarachik, Corenzwit and Longinotti (1964) showed a one-to-one correspondence between the existence of temperature dependent susceptibility and a minimum in the resistivity against temperature. This resistivity minimum in magnetically dilute alloys will be described in Section 5.3.

Another approach has appeared in the literature, this is called the localized spin fluctuation (LSF) theory. According to this theory the appearance of the magnetic moment is the consequence of fluctuations at the impurity site. This model, which was supposed to work for nearly magnetic impurities, can also lead to anomalous electrical and magnetic properties [Levine and Suhl (1968), Heeger (1969]].

5.2 The Anderson Hamiltonian

Since it was found that most systems including anomalous rare earths[†] could be described by the Anderson Hamiltonian, it will be briefly introduced here (Anderson 1961).

The Anderson Hamiltonian for the localized d orbitals (f orbitals in the case of rare earths) and host metal conduction electrons is

$$H = H_s + H_d + H_{sd} \tag{5.9}$$

where

$$H_s = \sum_{k\sigma} \varepsilon_k \, c_{k\sigma}^{+} \, c_{k\sigma} \tag{5.10}$$

[†] Cerium, ytterbium, europium and probably lanthanum are "anomalous" rare earth metals. Their valency is different from 3 and they have a non integral number of 4f electrons which can vary with pressure and temperature (Coqblin 1971).

$$H_d = \sum_{m\sigma} E_m c_{m\sigma}^+ c_{m\sigma} + \frac{1}{2}(U - \Gamma) \sum_{m \neq n} c_{m\sigma}^+ c_{m\sigma} c_{n\sigma}^+ c_{n\sigma}$$

$$+ U \sum_{m,n} c_{m\sigma}^+ c_{m\sigma} c_{n-\sigma}^+ c_{n-\sigma} \tag{5.11}$$

$$H_{sd} = \sum_{km\sigma} (V_{km} c_{k\sigma}^+ c_{m\sigma} + V_{mk} c_{m\sigma}^+ c_{k\sigma}) \tag{5.12}$$

In the Anderson Hamiltonian (5.9), the impurity states are introduced as extra orbitals; in the most simple case one orbital with two spin directions $\sigma = +, -$ and energy E_m is considered. H_s is the Hamiltonian for the conduction electrons. $c_{k\sigma}^+$ and $c_{k\sigma}$ are the creation and annihilation operators of the electron with wave vector $\vec{k}$ and spin σ, ε_k being its energy. H_d is the Hamiltonian for the d electrons. U and Γ are the Coulomb exchange integrals between two electrons localized on the impurity atom in the metallic environment. V_{mk} is the admixture matrix element between d states and conduction electrons. The second term in equation 5.11 corresponds to the Coulomb interaction between electrons of parallel spin on different orbitals. The last term in equation 5.11 describes the Coulomb interaction between the arbitrary electrons with opposite spins.

It should be noted that the Anderson Hamiltonian does not include the following:

(a) Electron-electron interactions except for electrons in the localized state,

(b) Spin-orbit and orbit-orbit interactions,

(c) The crystalline electric field terms, responsible for the crystalline splitting, are not included.

An extensive theoretical review was given by Kondo about dilute magnetic alloys (1969). Also a detailed review by Heeger (1969) covers recent developments and gives references to the experimental literature.

5.3 The Kondo Effect

After having given an extremely simplified picture for local moment formation, some of their properties will be given here.

Schrieffer and Wolff (1966) found that Anderson's Hamiltonian can be replaced by the s-d exchange model used by Kondo (1964) when the Coulomb repulsion between opposite spin electrons located on the d orbitals is large. In the s-d exchange model, a spin angular momentum $\vec{S}$ is assigned to the impurity spin and the s-d Hamiltonian is given as

$$H_{ex} = -\Gamma \vec{S} \cdot \vec{s} \qquad (5.13)$$

where $\vec{s}$ is the conduction electron spin, Γ is the negative (i.e. anti-ferromagnetic coupling) s-d exchange integral. This model was proposed by Zener (1951) and has been widely used in consideration of transition metals and alloys. Since this model implies the existence of a well defined impurity spin $\vec{S}$ which is expected in the infinite Coulomb limit, one should consider the validity of the s-d model for real impurities in metals.

The scattering of conduction electrons from the impurity produced by H_{ex} leads to a contribution to the electrical resistivity. This magnetic contribution is often called spin-disorder resistivity. The scattering can either lead to a flip of the conduction electron and impurity spin or without a spin flip. The spin flip processes allow the impurity moment to exchange energy with the conduction electrons.

For most alloy systems, the exchange integral Γ in equation 5.13 is quite small with a value of the order of 0.1 eV in typical cases (Béal-Monod and Weiner 1968). Thus the term H_x in the Hamiltonian can be regarded as a weak perturbation since it is small compared to the kinetic energy of the electrons. Such a term can be treated by perturbation theory. But Kondo (1964) found that this is not the case. He showed that the interaction (H_{ex}) cannot be treated satisfactorily in the framework of one-electron theory, but leads to a many-body problem. Two very important conclusions came out from Kondo's work:

(i) The contribution to the resistivity in the second-order perturbation theory can explain the occurrence of a well defined minimum in the electrical resistivity of alloys at low temperature.

(ii) The scattering amplitude diverges logarithmically at T = 0.

Thus, even though H_{ex} is a small term in the Hamiltonian, these results indicate that low-order perturbation theory is inadequate at low temperatures.

Before giving Kondo's result for the contribution to the resistivity in the second-order perturbation theory, let us see the typical temperature dependence of resistivity of alloys. If the impurity is nonmagnetic, the resistivity of the alloy will be similar to curve a in Fig. 5.3. The extrapolation of this curve to T = 0 will give the residual resistivity which is due to the impurity potential. The variation with temperature comes from lattice scattering. In the case of magnetic impurities, the variation of the resistivity curves looks like b and c in Fig. 5.3. The resistance minimum occurs mostly at around 10 - 20 K which varies from alloys to alloys. When the concentration of the magnetic impurity is increased beyond a limit,

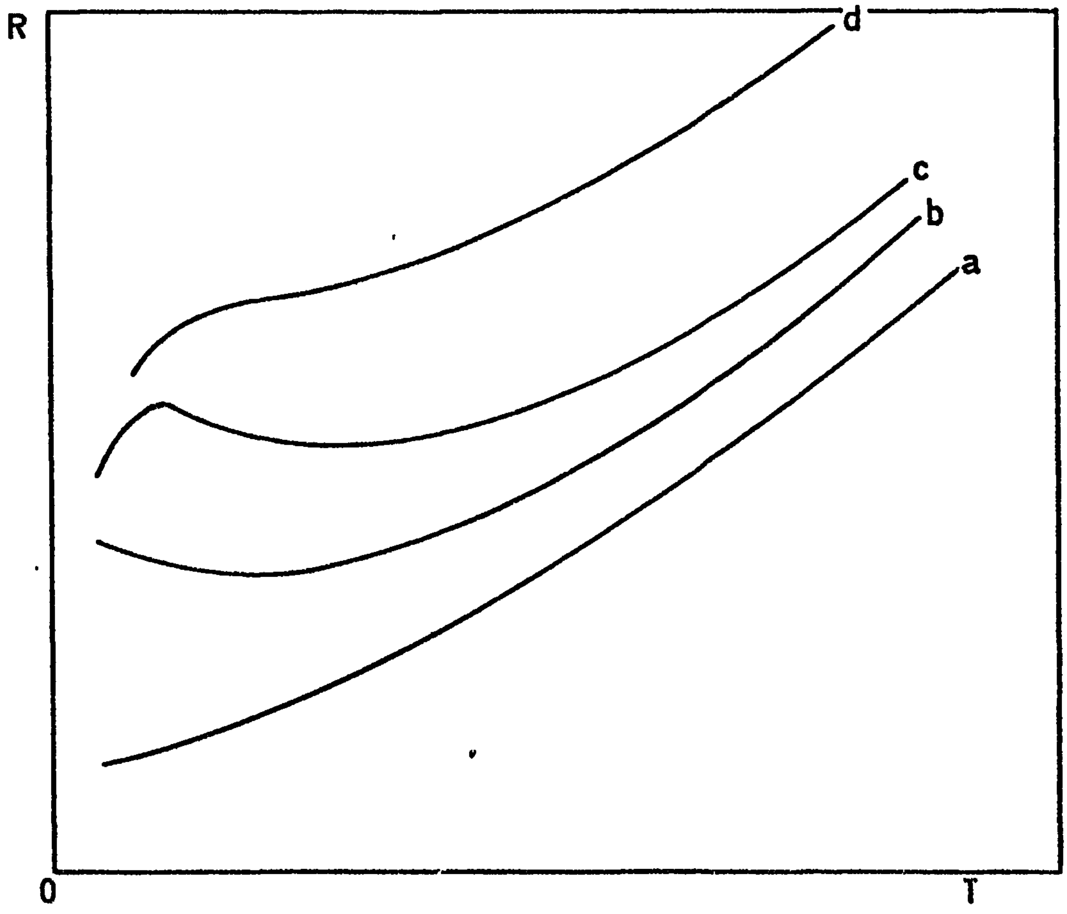

FIG. 5-3. Typical R-T curves of alloys.
(a) Nonmagnetic case.
(b) Case of magnetic impurities (Kondo effect).
(c) Large fraction of magnetic impurities.
(d) Still larger fraction.

the resistivity minimum disappears as shown in curve d in Fig. 5.3.

Now the main result of Kondo's work will be outlined. Consider an electron of wave vector $\vec{k}$ and spin up (which will be denoted by $\vec{k}\uparrow$), and let it scatter off the impurity by means of H_{ex} (equation 5.13), Suppose no spin flip occurs in the scattering process. If the electron $\vec{k}\uparrow$ is scattered to $\vec{k}'\uparrow$, then to lowest order in Hamiltonion, the matrix of scattering theory is given by

$$T^{(1)} = -\frac{\Gamma}{N} S_z \qquad (5.14)$$

where S_z is the impurity spin operator and N is the number of atoms in unit volume. The scattering cross section is proportional to $\left[(-\Gamma/N).S_z\right]^2$. The impurity-impurity scattering is neglected.

Now consider the second order contributions to the conduction electron scattering amplitude. Let ε_k be the energy of the electron in the initial state $(\vec{k})$, and $\varepsilon_{k''}$ the energy of the electron in the intermediate state. There are two successive scattering processes. As far as the intermediate state is concerned there are two possibilities:

(i) First the electron with the wave vector $\vec{k}$ is scattered from the initial state into the intermediate state with the wave vector $\vec{k}''$, and then this electron with $\vec{k}''$ is scattered into the final state with $\vec{k}'$.

(ii) In the first scattering process an electron-hole pair is created by the spin of the impurity, and in the second process the created hole annihilates the electron with the wave vector $\vec{k}$, leaving the created electron in the final state.

These processes are represented by diagrams in Fig. 5.4(a) and (b) respectively (Grüner and Zawadowski 1974). The second order contribution to the T scattering matrix from the processes in Fig. 5.4(a) and (b) are given respectively by $T^{(2a)}$ and $T^{(2b)}$ in equation 5.15 and equation 5.16 (Kondo 1969).

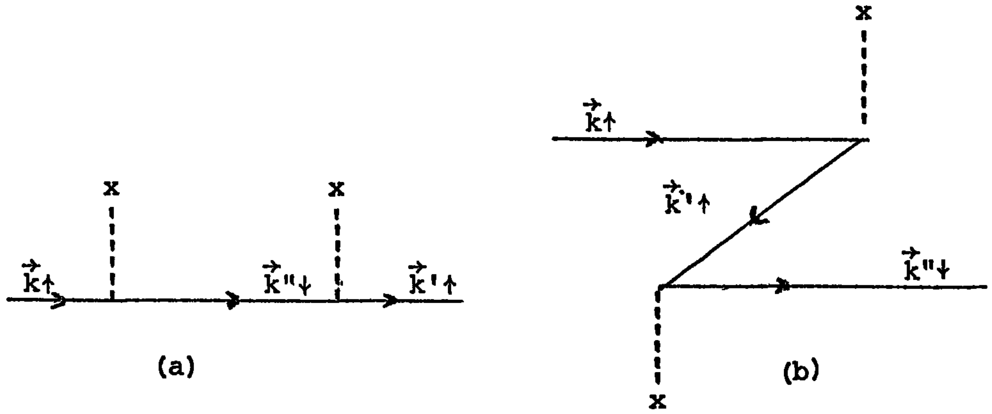

Fig.5.4: Two time-ordered diagrams corresponding to second order scattering processes with spin-flip in the intermediate state. The full lines represent electrons or holes; the broken lines with a cross at the end represent the exchange interaction. These are the processes responsible for the Kondo effect.

$$T^{(2a)} = \left(-\frac{\Gamma}{N}\right)^2 \left(S_z^2 + S_- S_+\right) \sum_{k''} \frac{1 - f_{k''}}{\left(\varepsilon_k - \varepsilon_{k''}\right)} \qquad (5.15)$$

$$T^{(2b)} = -\left(-\frac{\Gamma}{N}\right)^2 \left(S_z^2 + S_+ S_-\right) \sum_{k''} \frac{f_{k''}}{\left(\varepsilon_{k''} - \varepsilon_{k'}\right)} \qquad (5.16)$$

The quantity $f(\varepsilon_{k''})$ is the Fermi-Dirac distribution function and S_+ and S_- are the step up and the step down spin operators respectively. The minus sign in equation 5.16 enters because of the Pauli principle; the final state electron $(\vec{k}'\uparrow)$ is created before the initial state electron is destroyed in Fig. 5.4(b). The opposite is true in Fig. 5.4(a). This is equivalent of interchanging the initial and final state electrons $(\vec{k}\uparrow)$ and $(\vec{k}'\uparrow)$, and the two matrix elements differ by minus sign as a consequence of the anti-symmetric character of the wave functions of Fermi systems.

Considering the energy conservation $\varepsilon_k = \varepsilon_{k'}$, the matrix elements $T^{(2a)}$ and $T^{(2b)}$ combine to give

$$T^{(2)} = \left(\frac{\Gamma}{N}\right)^2 \left[S_z^2 + \frac{1}{2}(S_+S_- + S_-S_+)\right] \sum_{k''} \left(\frac{1}{\varepsilon_k - \varepsilon_{k''}}\right)$$

$$+ \left(\frac{\Gamma}{N}\right)^2 \left(S_-S_+ - S_+S_-\right) \sum_{k''} \frac{\left(f_{k''} - \frac{1}{2}\right)}{\varepsilon_{k''} - \varepsilon_k} \qquad (5.17\ )$$

The first term in this equation does not depend on ε_F (Fermi energy). The second term in equation 5.17 is the crucial term. In the theory of electrical resistivity, one is concerned with the scattering from an impurity of electrons with energy ε_k very close to ε_F. It should be noted that $S_-S_+ - S_+S_- \neq 0$ because of the uncommutativity of the spin operators (Kondo 1964). The resistivity in the second order perturbation is given below as derived by Kondo (1969)

$$R = c\ \rho_M \left[1 + 4\ \Gamma\ \rho\ \ln\left(\frac{k_B T}{D}\right)\right] \qquad (5.18\ )$$

where

$$\rho_M = \frac{2\pi\ \rho\ m}{z\ N\ e^2\ \hbar}\ \Gamma^2\ S(S+1)$$

In this equation, ρ_M is a measure of the strength of the exchange scattering; c the impurity concentration; m the mass of electron and z is the number of conduction electrons per atom. The density of states is specified as:

$$\rho(\varepsilon) = \rho \qquad -D \leqslant \varepsilon \leqslant D$$

$$= 0 \qquad \text{otherwise .}$$

It means that the density of states $\rho(\varepsilon)$ assumes a value ρ within a band of width 2D.

Equation 5.18 is the basis of Kondo's explanation of the resistivity minimum observed in a large number of dilute alloys. For example the temperature dependence of the resistivity of Cu containing Fe impurities is shown in Fig. 5.5. On theoretical grounds, one expects $\Gamma < 0$ for many alloy systems (Schrieffer and Wolff 1966). Assuming $k_BT < D$, (which is well satisfied in practice) the contribution to the resistivity from magnetic impurity scattering (spin disorder scattering) increases with decreasing temperature. This is just the opposite of what one expects from other mechanisms which contribute to the electrical resistivity of metals. The origin of this phenomenon comes from the dynamical nature of the spin system and is associated with the sharpness of the Fermi surface (Kondo 1964).

When one combines the various contributions to the total resistivity (= residual resistivity + spin-disorder resistivity + phonon resistivity), a minimum appears, as one passes from the region where electron-phonon scattering makes the dominant contribution to the resistivity, to the region where the temperature dependent magnetic scattering dominates. The ℓnT variation of the resistivity below the resistivity minimum temperature is observed in many alloy systems. Daybell and Steyert (1968) reviewed the data on a large number of alloys which exhibit the Kondo effect.

5.4 The Kondo Temperature

As is seen from equation 5.18, the resistivity will continue to increase with decreasing temperature and becomes unphysical for

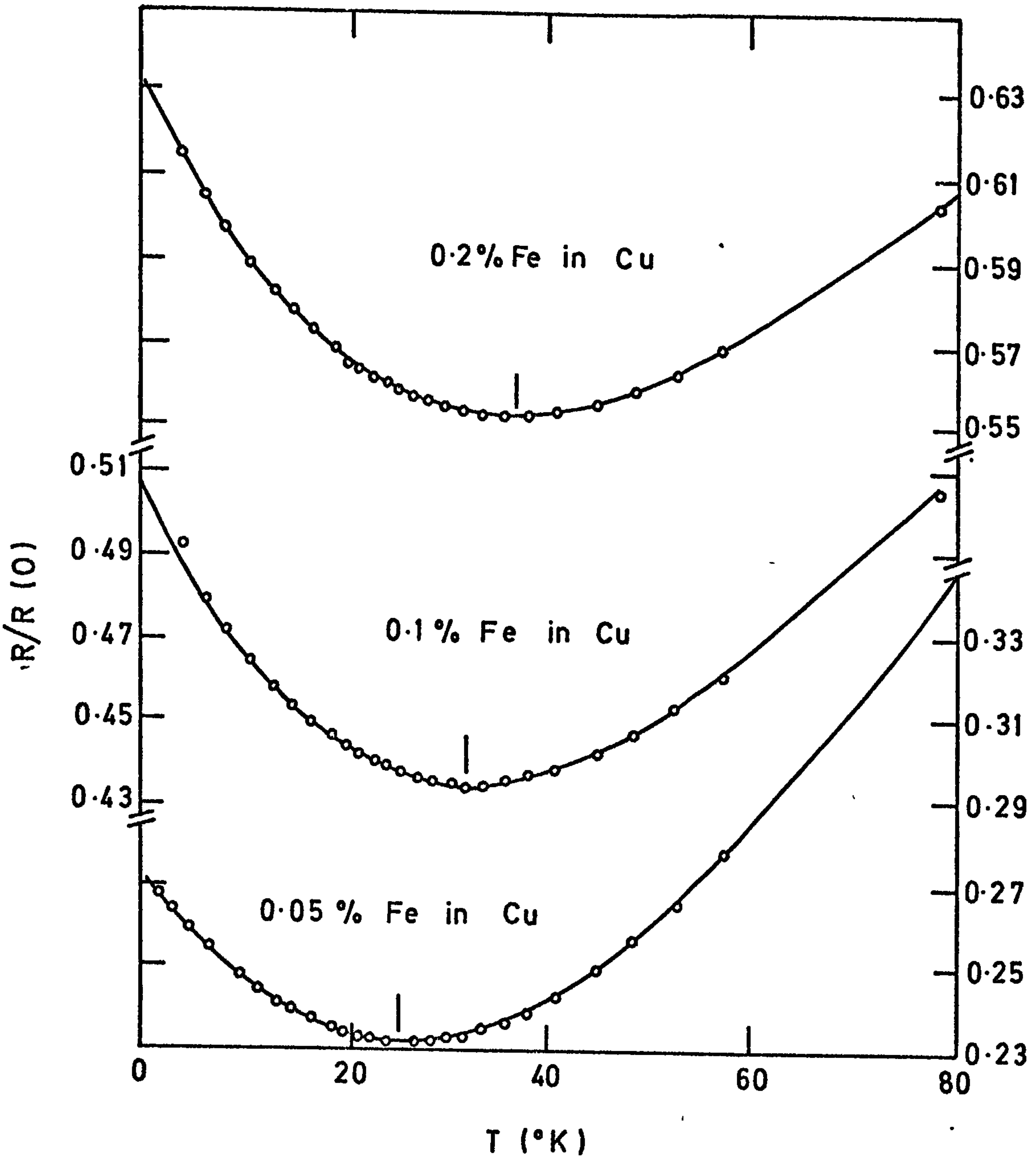

FIG. 5·5. The resistance as a function of temperature for CuFe [Franck et al. 1961]

$T \to 0$. This means that second order perturbation theory becomes invalid below a certain temperature:

$$T_K = \frac{D}{k_B} \exp\left(- \frac{1}{|\Gamma|\,\rho} \right) . \qquad (5.19)$$

This characteristic temperature is usually called the Kondo temperature and varies widely from alloy to alloy. The temperature dependence of the impurity contribution to the susceptibility varies with temperature roughly like $C/T_k + T$, where C is the curie constant, and a well-defined peak appears in the specific heat when $T \approx T_k$.

Suhl (1967) and Nagaoka (1967) have shown that the electrical resistivity increases with decreasing temperature for $T > T_k$ and turns over, flattens out, and approaches a constant value as $T \to 0$, i.e. the spin-disorder resistivity saturates to the "Unitarity limit". Grüner and Zawadowski (1974) suggested that a strong correlation between the impurity spin and conduction electrons with opposite spin direction is built up for $T < T_k$. This correlation leads to the "Spin compensation cloud" in the conduction electron gas. The energy associated with the formation of the compensation cloud is of the order of the Kondo energy $k_B T_k$.

Several sophisticated theories of the region, where $T \lesssim T_k$ have appeared in the literature and reviewed by Kondo (1969), Heeger (1969), Fischer (1971), Grüner and Zawadowski (1974).

So far, the magnetic impurity ion has been treated as a degenerate system. Praseodymium possesses crystalline electric fields which are sufficiently strong to modify the behaviour of the magnetic resistivity contribution to the total electrical resistivity. So, the effect of the crystalline electric field on the Kondo exchange scattering will be discussed in the next chapter.

CHAPTER 6

THE INFLUENCE OF THE CRYSTALLINE ELECTRIC FIELD ON THE KONDO EFFECT OF ALLOYS WITH CERIUM IMPURITIES

6.1 Introduction

In Chapter 5, a simple description of localized magnetic moments and some of their properties in alloys were outlined. It was clear from Kondo's work that the s-d exchange interaction between the spins of the conduction electrons and the localized magnetic moments of the transition elements leads to an increase of spin disorder resistivity (magnetic resistivity) with decreasing temperature. This anomaly comes out when one calculates the resistivity in second order perturbation theory and under certain conditions. These conditions are:

(i) the freedom of the localized moments to flip

(ii) an effective s-d exchange integral with a negative sign.

It should be noted that interactions between the magnetic impurities have been neglected in magnetically dilute alloys showing the Kondo effect. Correlation between the localized magnetic moments prevents the freedom of these moments to flip and can eventually quench the Kondo effect. The disappearance of the Kondo effect in AuFe at Fe concentrations more than 1 at.% was attributed to short-range order effect by Harrison and Klein (1967). However, in rare earth systems direct magnetic coupling between the localized moments is negligibly small because of the localized character of the 4f electrons. The 4f state of the rare earth atom will have a magnetic moment close to that of the free ion. In the absence of strong indirect coupling it is conceivable that rare earth metallic systems could show a

Kondo effect in the non-dilute case too. Evidence for the occurrence of Kondo effect has been found in non-dilute alloys of LaCe [Sugawara, Eguchi (1966), Arajs, Anderson (1969) and Edelstein (1968)] and in Y-Ce [Sugawara (1965) and Hill, Miner, Elliot (1969)].

In this chapter, an outline will be given of the effect of the crystalline electric field on the Kondo exchange scattering. Some relevant data with regard to the alloys and compounds with cerium impurities showing the Kondo effect will also be presented.

6.2 Kondo Sideband Model

So far, the magnetic ion has been treated as a degenerate system. The effect of the crystalline electric field from its environment is such as to lift partially the (2J + 1)-fold degeneracy. [For example, in the Pr-Ce alloys the hexagonal crystalline electric field splits the ground state multiplet of the Ce^{3+} ion ($J = \frac{5}{2}$) into three Kramers' doublets, i.e. $|\pm\frac{1}{2}>$, $|\pm\frac{3}{2}>$ and $|\pm\frac{5}{2}>$ see Appendix 1]. This is capable of profoundly modifying the magnetic resistivity as has been shown by a number of authors, [Hirst (1967), Watabe and Kasuya (1969), Maranzana (1970), Maranzana and Bianchessi (1971)].

Let us consider the Ce^{3+} ion in the presence of a hexagonal crystalline electric field. As was seen in Chapter 5, in the Kondo exchange scattering the z component of the localized spin moment in the intermediate state differs by one quantum from the corresponding initial and/or final state. In a normal Kondo system, the localized spin, e.g. the doublet $|\pm\frac{1}{2}>$, can flip in the paramagnetic range without energy expenditure. If the s-f exchange integral is negative, the magnetic resistivity diverges logarithmically at $T = 0$ for scattering of the conduction electrons at the Fermi level.

In the presence of hexagonal crystalline electric field, scattering processes involving the pairs of doublets such as $|\pm\frac{5}{2}>$, $|\pm\frac{3}{2}>$ or $|\pm\frac{3}{2}>$, $|\pm\frac{1}{2}>$ become inelastic. Maranzana (1970) showed that for each pair of doublets Kondo exchange scattering leads to a sharp resonance peak at $T = 0$ in the magnetic resistivity (transition probability) at an energy shifted away from E_F of an amount equal to the energy separation of the pair. These resonance peaks are called "Kondo Side-Bands". Thus one expects the existence of two peaks in the $\rho - T$ curve at temperatures equivalent to the distances of the energy level in the two pair of doublets. The higher the temperature at which they occur, the broader are the peaks. This is due to the Fermi level becoming diffuse at higher temperatures [van Daal, Maranzana and Buschow (1971)].

6.3 Modifications in the Kondo Sidebands Theory

Maranzana (1970) considered the crystalline electric field effects on the Kondo resistivity using the usual exchange Hamiltonian $\vec{s}\cdot\vec{S}$ (Eq. 5.13). Since this restricts transitions to $\Delta m = 0,1$, some transitions become energetically unfavourable in the presence of a crystalline electric field. For example, if the lowest doublet has $J = \pm\frac{5}{2}$ or $\pm\frac{3}{2}$, transitions within the doublet are no longer possible, so that there is no divergency appearing at energy $\varepsilon \to E_F$ and consequently no Kondo effect for temperatures much lower than Δ (Δ is the energy separation between the lowest two doublets).

Cornut and Coqblin (1972) used a generalized Hamiltonian,

$$H = \sum_{k,m} \varepsilon_k c^+_{km} c_{km} - \sum_{\substack{k,k' \\ m,m'}} \Gamma_{mm'} c^+_{k'm'} c_{km} c^+_m c_{m'}$$

$$+ \sum_{k,k',m} v_{mm} c^+_{k'm} c_{km} \qquad (6.1)$$

which permits transitions $\Delta m = 0, \pm 1, \ldots \pm 2J$. They have found in addition to the Kondo sidebands that there is also always a singularity at E_F, whatever the nature of the ground state. Thus resistivity should again increase at low temperatures. Careful resistivity measurements of suitable rare earth alloys will be able to clarify the situation.

The Hamiltonian (Eq.6.1) is considerably different from the s-f (Eq.5.13) exchange Hamiltonian and describes spin and orbit exchange scattering. The third term in Eq.6.1 represents direct interaction coming from the impurity potential.

6.4 Alloys with Ce Impurities

The alloys with cerium impurities can be classified according to the position of the narrow 4f level relative to the Fermi level (Coqblin 1971).

(i) Magnetic Cerium Alloys

If the 4f level is below the Fermi level the cerium alloy is magnetic. According to Kondo (1962) the effective exchange integral between the conduction electrons and the localized moments is written as

$$\Gamma = \Gamma_1 + \Gamma_2 \quad . \tag{6.2}$$

where Γ_1 is the integral for direct interaction and is small, positive and almost pressure independent. Γ_2 comes from the effect of mixing and given by

$$\Gamma_2 = -\frac{2\,V_{kf}^2}{|\varepsilon|} \tag{6.3}$$

$\varepsilon(\varepsilon < 0)$ is the distance from the 4f level to the Fermi level. The sign of Γ depends on the relative magnitude of the two terms, and becomes negative if the amount of mixing is large. The magnitude of Γ_2 of the rare earth ions in dilute alloys depends on the electronic structure of the host metal. Γ_2 varies with pressure, because $|\varepsilon|$ decreases (Coqblin 1971).

As was mentioned in the first chapter, the classical Hamiltonian for rare earths is given by Eq.1.4 [de Gennes (1962)]

$$H = -\Gamma(g-1)\,\vec{J}.\vec{s} \tag{1.4}$$

However, it was pointed out by Coqblin and Schrieffer (1969) that the Hamiltonian (1.4) leads to a rather puzzling result. In fact in the case of cerium impurities (g - 1) is negative so that Hamiltonian (1.4) would give a Kondo effect only for $\Gamma > 0$ in contrast to transition metal alloys for which $\Gamma < 0$.

This situation has been clarified by Coqblin and Schrieffer (1969) by following a different approach to the problem. Starting from the Anderson model of a $4f^1$ configuration of Ce, they treated the exchange interaction taking into account spin-orbit interaction. The new Hamiltonian (Eq. 6.1) leads to a Kondo effect when the exchange interaction constant is negative, as it is in the case of transition metal impurities.

The examples for the magnetic alloys (with cerium impurities) which show Kondo effect are Y-Ce, La-Ce, $LaAl_2Ce$ ... In this case Γ is negative and $|\Gamma_2| > \Gamma_1$.

Some magnetic alloys with cerium impurities such as Mg-Ce, Ag-Ce do not show Kondo effect, i.e. Γ is positive and $|\Gamma_2| < \Gamma_1$. Hedgcock and Petrie (1970) have explained the absence of a Kondo effect in their Mg-Ce alloys as being due to a large energy gap (ε) between the Fermi level and the cerium 4f levels resulting in a negligible s-f exchange interaction.

(ii) Nonmagnetic Alloys

When the 4f level is above the Fermi level, the mixing term is negligible and cerium alloys behave as normal nonmagnetic alloys. The absence of the Kondo effect in Lu-Ce and Sc-Ce [Sugawara, Yamase, and Soga (1965)] may be attributed to the instability of the 4f electron of cerium.

As we have seen in Chapter 3, the magnetic γ-Ce stable at room temperature and atmosphere pressure transforms to α-Ce at low temperature and high pressure. The decrease in volume accompanying the $\gamma - \alpha$-Ce transformation has been attributed to the change of valency of the Ce ion towards the nonmagnetic tetravalent state. The same transition has been suggested when cerium is dissolved in

Lutetium and Scandium, as these host metals have atomic volumes smaller than that of the magnetic cerium. This leads to the large residual resistivities of Lu-Ce and Sc-Ce reported by Sugawara et al. (1965).

6.5 Lanthanum-Cerium Alloys

Sugawara and Equchi (1966) have observed a Kondo effect in Lanthanum-Cerium alloys containing up to 3.1 at.% Ce. Resistance minima were found at about 6.5 K in fcc La-Ce alloys and at about 5.8 K in dhcp La-Ce alloys as is shown in Figure 6.1. They state that the temperature at which the minimum occurs, is independent of cerium concentration. Arajs and Anderson (1969) have extended these results up to a cerium concentration of 8.5 at.% for the temperature range of 4 - 30 K. From their work which is presented in Figure 6.2, it is clear that all the samples show the Kondo effect. The specimens were of fcc structure. T_{min} increases very slowly with increasing concentration of cerium.

In addition, Elliot, Hill and Miner (1969) have found minima in the resistivity-temperature curves in some nondilute Ce-La (14 to 18 at.% La) alloys. Figure 6.3 shows the resistivity behaviour of some nondilute La-Ce alloys taken from Elliot et al. (1969). The minimum occurs at around 17 K, is most pronounced in the alloy containing 18 at.% La and disappears at solute concentrations below 14 at.% and above 18 at.%. The sharp change in slope of the resistivity curves around 9 K has been attributed to the antiferromagnetic transition of the alloys.

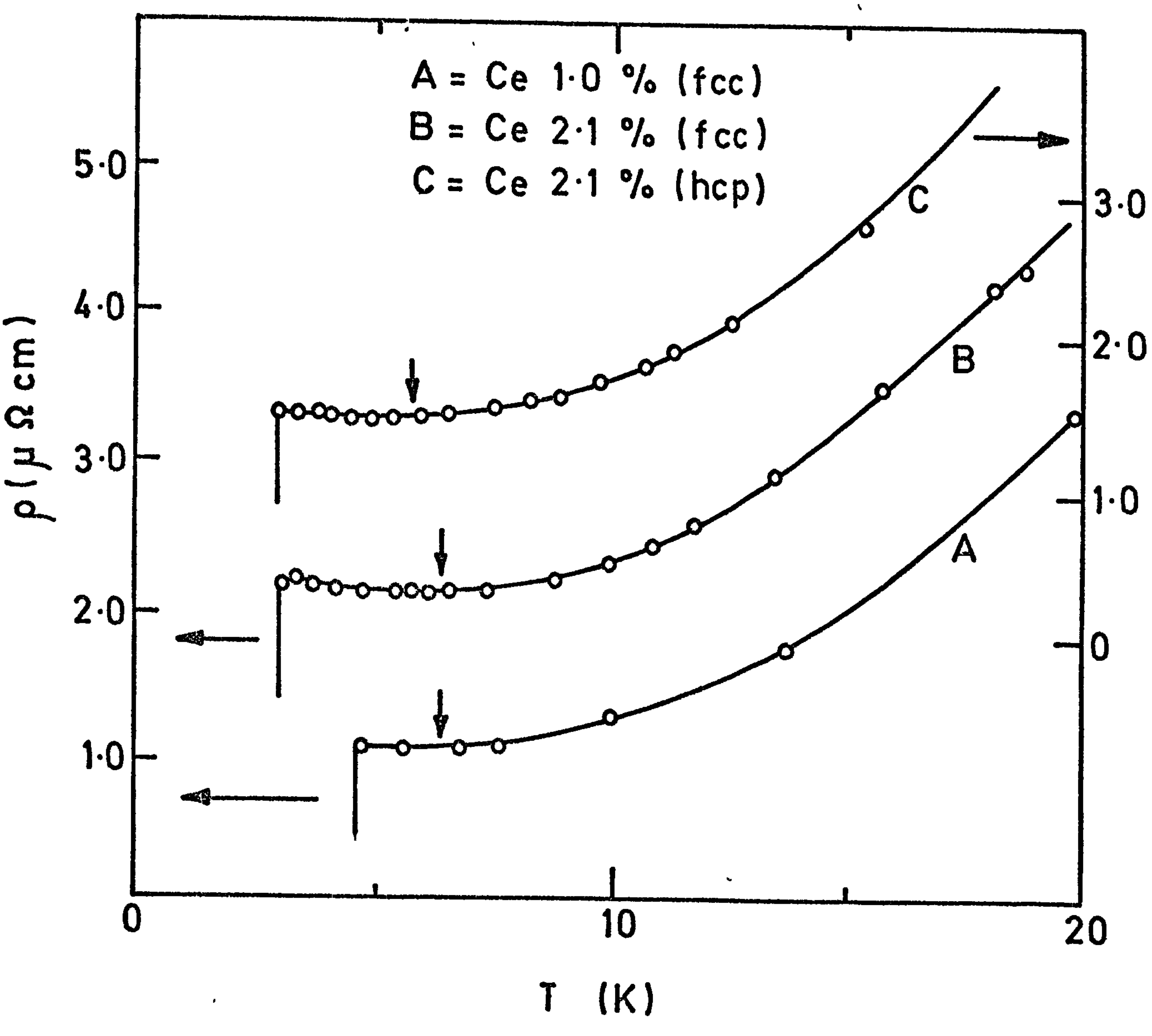

FIG. 6·1. Resistivities of fcc and hcp La-Ce alloys less the residual resistivity of La. The arrow indicates the minimum.

[Sugawara and Eguchi 1966]

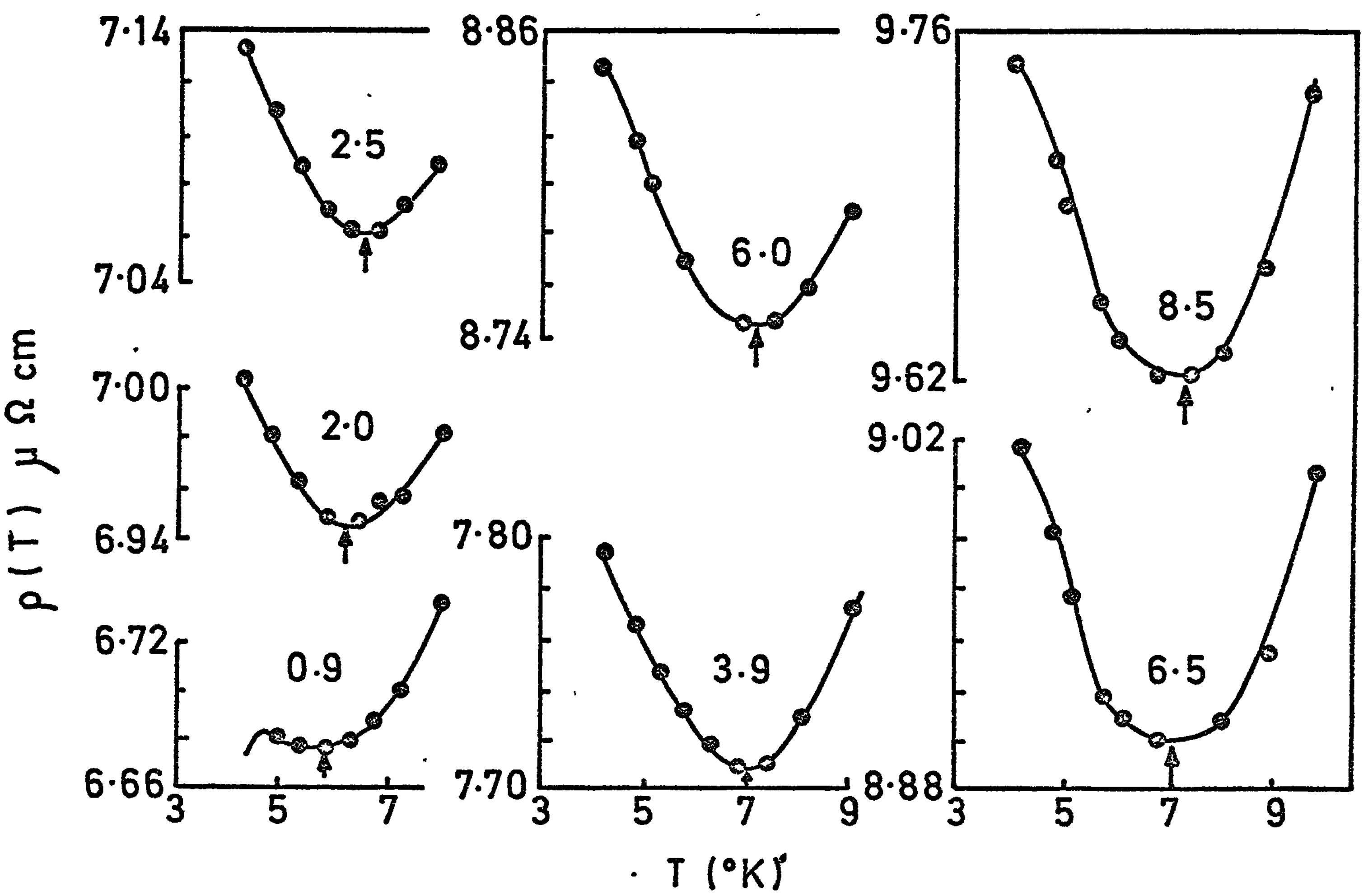

FIG. 6·2. Resistivity of La-Ce alloys. The number, associated with each curve, gives the cerium concentration in at. %. [Arajs and Anderson 1969]

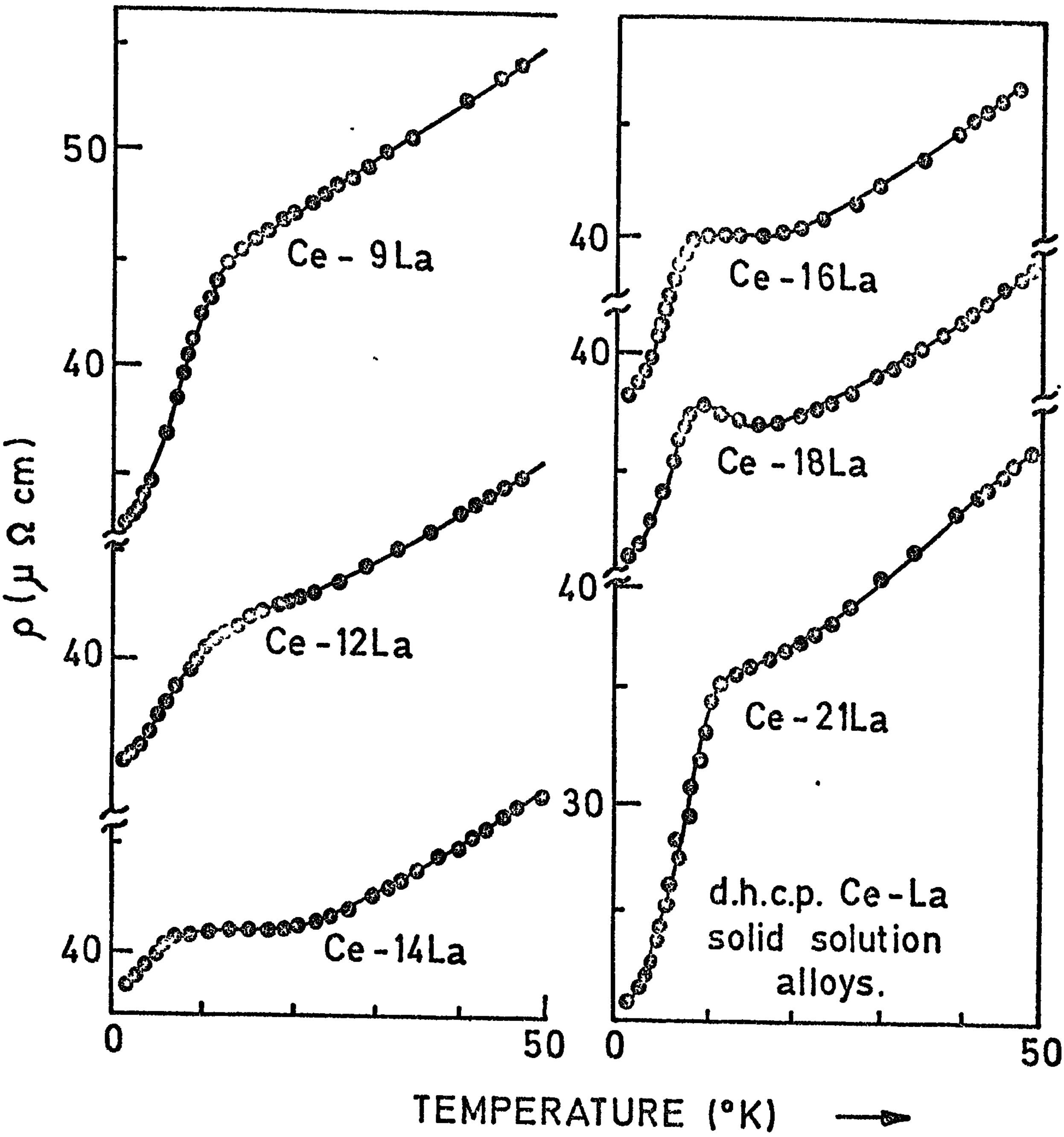

FIG. 6·3. Resistivity of d.h.c.p. Ce-La alloys. Indicated alloy compositions are in at % La. [Elliott et al. 1969]

Sugawara and Eguchi (1966) have interpreted the logarithmic dependence of the resistivity (the Kondo effect) in terms of the s-f exchange interaction, $(-\Gamma \vec{s}.\vec{S})$ between the cerium ion and conduction electrons. This logarithmic variation is shown in Figure 6.4. From this figure they have concluded that T_K, the Kondo temperature should be much lower than 0.4 K, because in the lower concentration sample the resistivity is proportional to $\ell n\, T$ down to 0.4 K. In the higher concentration sample, the resistivity at low temperatures shows a tendency of saturation due probably to the magnetic interaction between Ce ions.

The magnetic susceptibility measurements on the La-Ce alloys give departures from a Curie-Weiss law around 20-30 K and lead to an extrapolated Curie temperature of -27 K [Edelstein, Windmiller, Ketterson and Culbert (1971)]. They have found that the magnetic moment of a cerium atom dissolved in Lanthanum at low temperatures is smaller than that expected from a localized f electron. This results from the formation of a spin compensating electron cloud in the vicinity of the magnetic impurity. In fact, the magnetic susceptibility per gram of cerium of La-Ce alloys follows the $T^{-\frac{1}{2}}$ law in the temperature range $30 > T > 1.4$ K. Anderson (1967) has suggested this temperature dependence in the case of spin compensation.

Edelstein et al. (1971) have concluded from the susceptibility measurements that the Kondo temperature of La-Ce alloys was of the order 10 - 20 K. This is significantly different from the Kondo temperature value determined from the resistivity data.

The same uncertainty on the value of the Kondo temperature of La-Ce alloys could come from the interpretation of thermoelectric

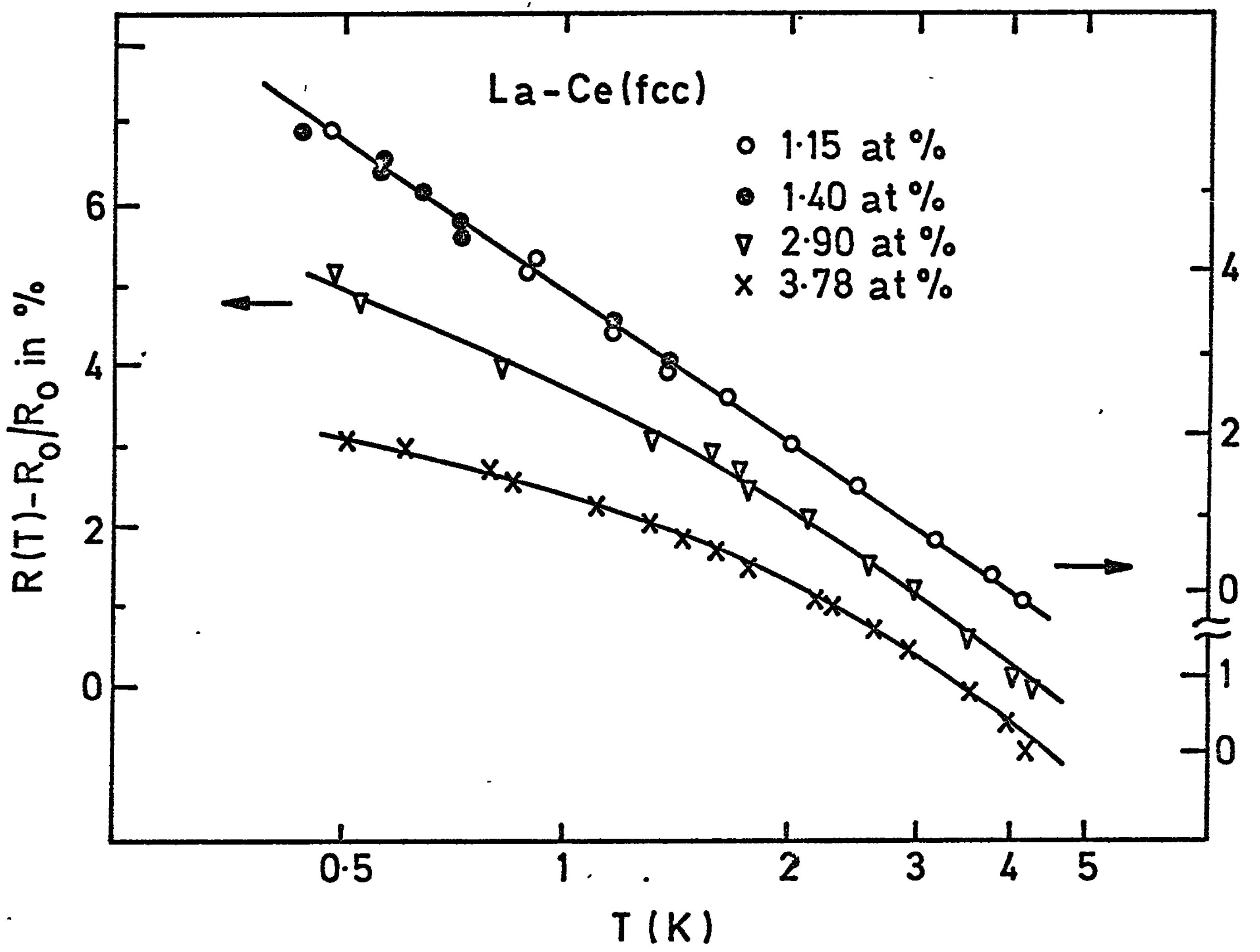

FIG. 6·4 Resistivity of fcc La-Ce alloys, normalized to the value at 4·2K. [Sugawara and Eguchi 1966] power experiments. Sugawara and Eguchi (1969) measured the thermoelectric power of La - 1.15 at.% Ce and found a monotonous variation between 7 - 30 K. They concluded that the Kondo temperature T_K cannot be in this temperature range because of the absence of a peak in the thermoelectric power. However, Grobman (1971) has found a negative peak in the thermoelectric power of La-Ce alloys at about 20 K and has suggested that this is the Kondo temperature. Cornut and Coqblin (1972) have suggested that this peak might be connected to the crystalline electric field rather than the Kondo temperature. In view of this notable difference between the Kondo temperatures of La-Ce alloys obtained from different sources, further experiments would be helpful to clarify the situation.

Studies of the pressure dependence of the resistivity and superconducting temperature T_c showed that the position of the 4f level could be increased relative to the Fermi level by applying pressure. This is the case in the La-Ce system. The 4f level moves above the Fermi level and the transition of the cerium impurity from a magnetic to a nonmagnetic state can be located at around 30 K bar [Maple, Wittig and Kim (1969)].

6.6 Yttrium-Cerium Alloys

Sugawara (1965) first investigated the resistivity of Yttrium-Cerium alloys in the temperature region between 1.6 and 300 K and found a resistance minimum at around 18 K. His result on Y-Ce alloys is shown in Figure 6.5. He reported that the depth of the minimum, $\rho\ (0^{\circ}\ K) - \rho\ (T_{min.})$, was nearly proportional to the cerium concentration.

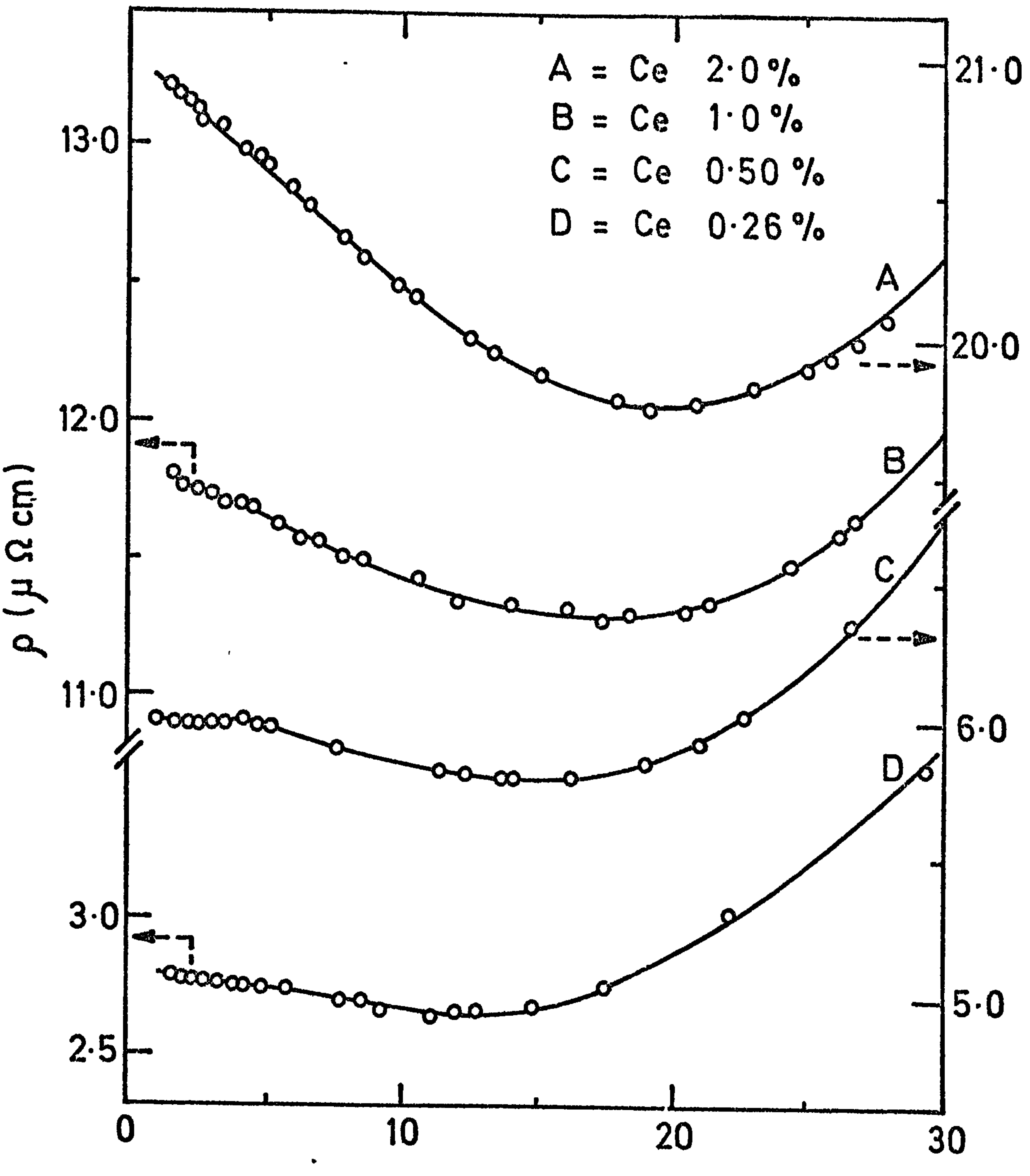

FIG. 6·5. Resistivity of Y-Ce. The residual resistivity of Y has been subtracted. [Sugawara 1965]

Sugawara and Yoshida (1968) have extended the measurements of the resistivity of Y-Ce alloys to lower temperatures down to 0.4 K. The temperature variation of the normalized solute resistivity $\Delta R(T)/\Delta R(0)$ of Y-Ce alloys is presented in Figure 6.6, where $\Delta R(0)$ is the value of the solute resistivity at 0 K. We can see from this figure that the solute resistivity increases as the temperature is lowered and remains constant at temperatures below 1.5 K. One can also notice the same temperature variation of the $\Delta R(T) / \Delta R(0)$ for every specimen. These observations are in qualitative agreement with the theoretical resistive behaviour of the spin compensated systems (Nagaoka 1967).

Hill, Miner and Elliott (1969) have observed the resistance minima indicative of a spin compensated state in hcp Yttrium-Cerium alloys containing up to 44 at.% cerium. Their result is presented in Figure 6.7. They have found the same logarithmic variation for the magnetic resistivity in nondilute alloys at low temperatures as Sugawara and Yoshida (1968) did find for dilute Y-Ce alloys.

These resistance minimum (the Kondo effect) in nondilute alloys have led to speculations that even pure cerium may exhibit a spin compensated state (Edelstein 1968).

It should be noted that the data presented so far for La-Ce and Y-Ce were obtained on polycrystalline specimens. In order to get further information, particularly about the effect of crystalline electric field on the Kondo system, Sugawara and Yoshida (1971) have carried out a detailed study of dilute Y-Ce single crystals. They found that the temperature variation of the normalized solute

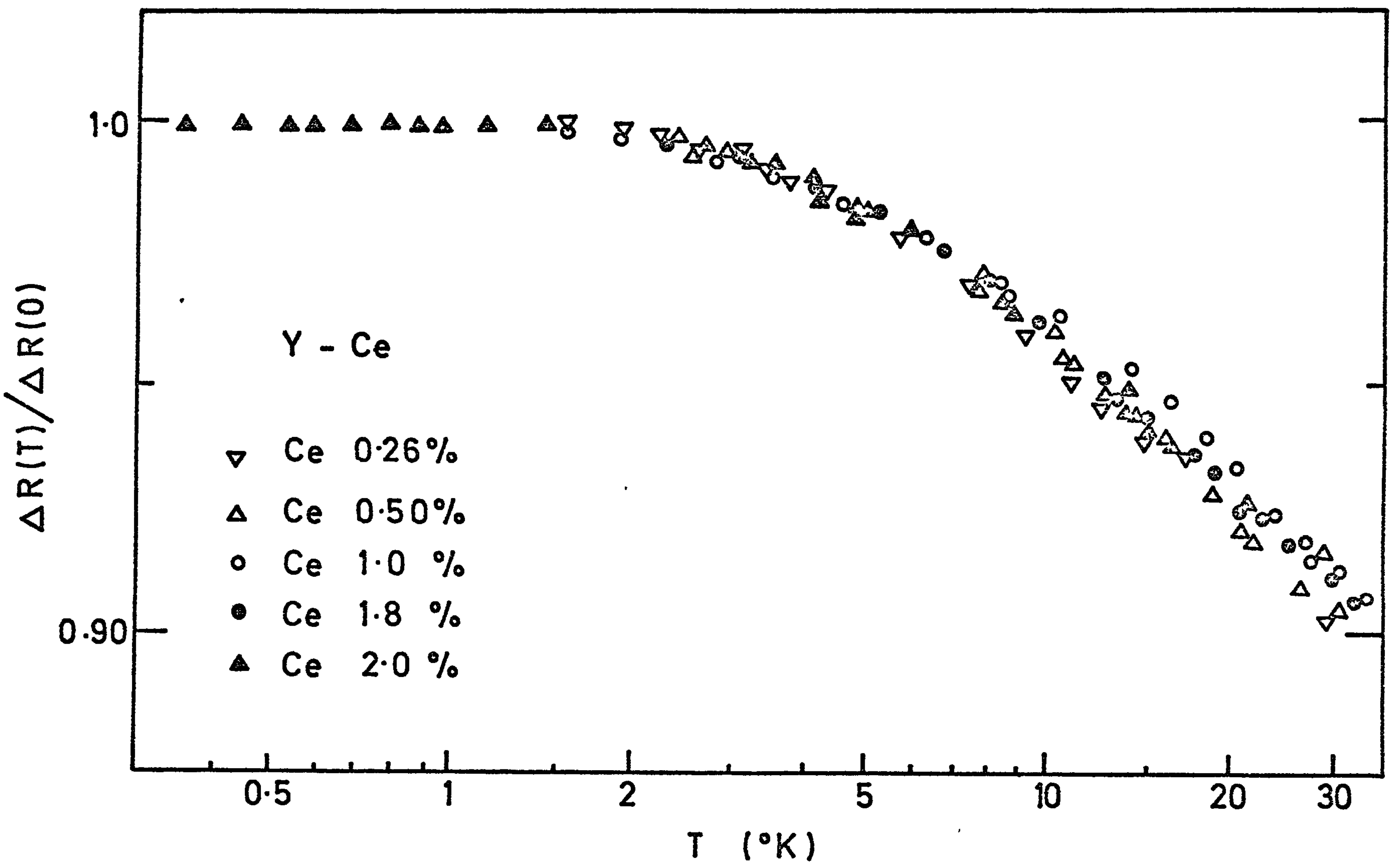

FIG. 6·6. The normalized solute resistivity in dilute Y - Ce alloys. [Sugawara and Yoshida 1968]

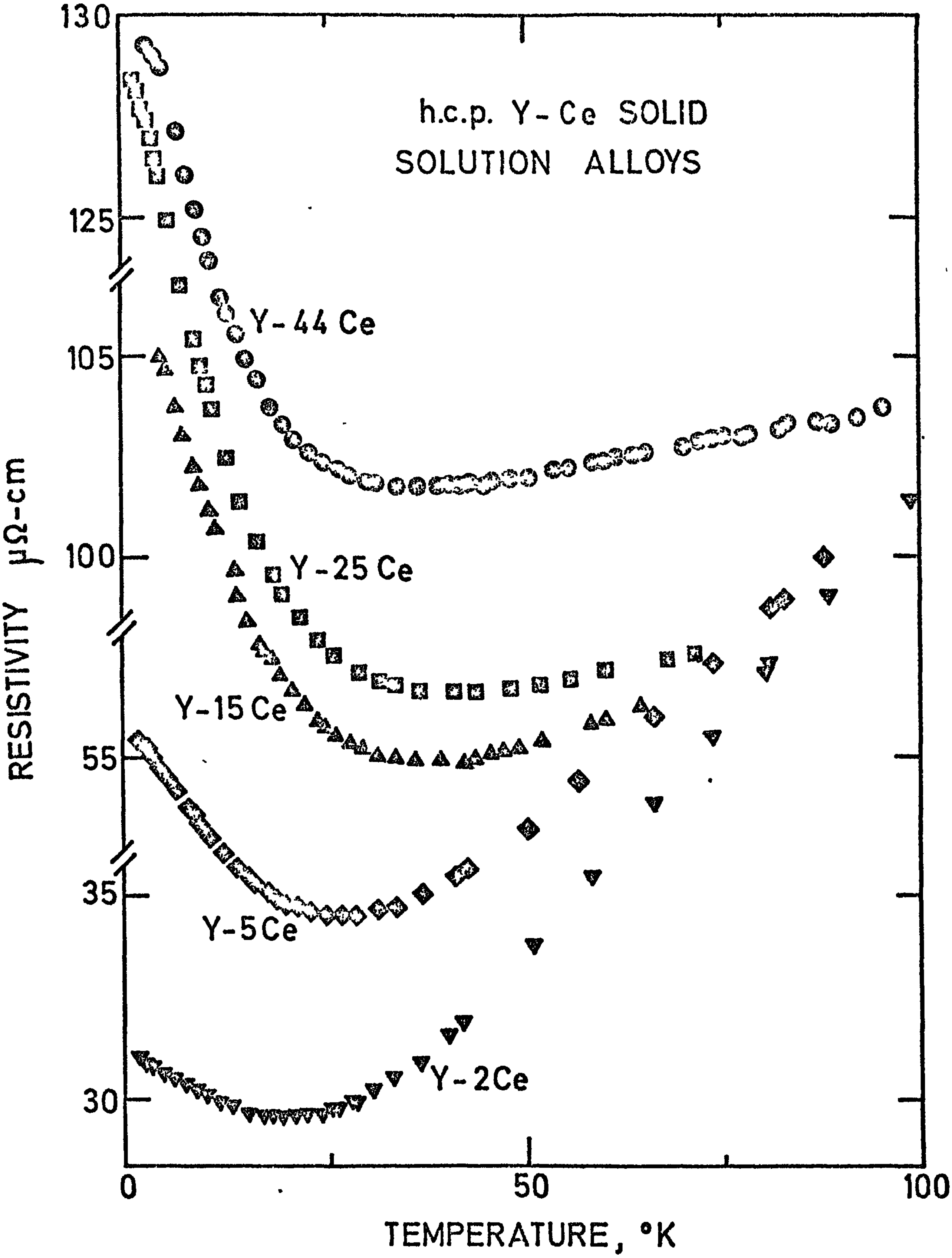

FIG. 6·7. ρ versus T for h.c.p. alloys. Indicated alloy compositions are in atomic percent. [Hill et al. 1969] resistivity was the same for the current direction parallel and perpendicular to the c axis. The resistivity behaviour of single crystal Y - 2 at.% Ce is given in Figure 6.8. From this work, they showed that the normalized parallel and perpendicular resistivities below 5 K could be expressed by

$$\frac{\Delta R\,(T)}{\Delta R\,(0)} = 1 - \left(\frac{T}{T_K}\right)^2$$

where T_K is the Kondo temperature which is isotropic and independent of the cerium concentration. The Kondo temperature is estimated to be at around 40 K from the resistivity data which is in good agreement with that obtained on polycrystalline specimen, 42 K [Sugawara and Yoshida (1968)]. The resistivity behaviour below the Kondo temperature was attributed to the existence of a bound state between the Ce^{3+} ion and the conduction electrons.

Sugawara and Yoshida (1971) have also measured the magnetic susceptibility of single crystals of Y-Ce alloys. The existence of the crystalline electric field splitting of cerium can be confirmed by the similarity between the observed temperature dependence and the theoretical curves. They proposed the following crystalline electric field levels diagram for Ce^{3+} ions in Yttrium in order to fit the susceptibility data to the calculated curves. The deviation of the experimental points from the theory was attributed to the Kondo effect.

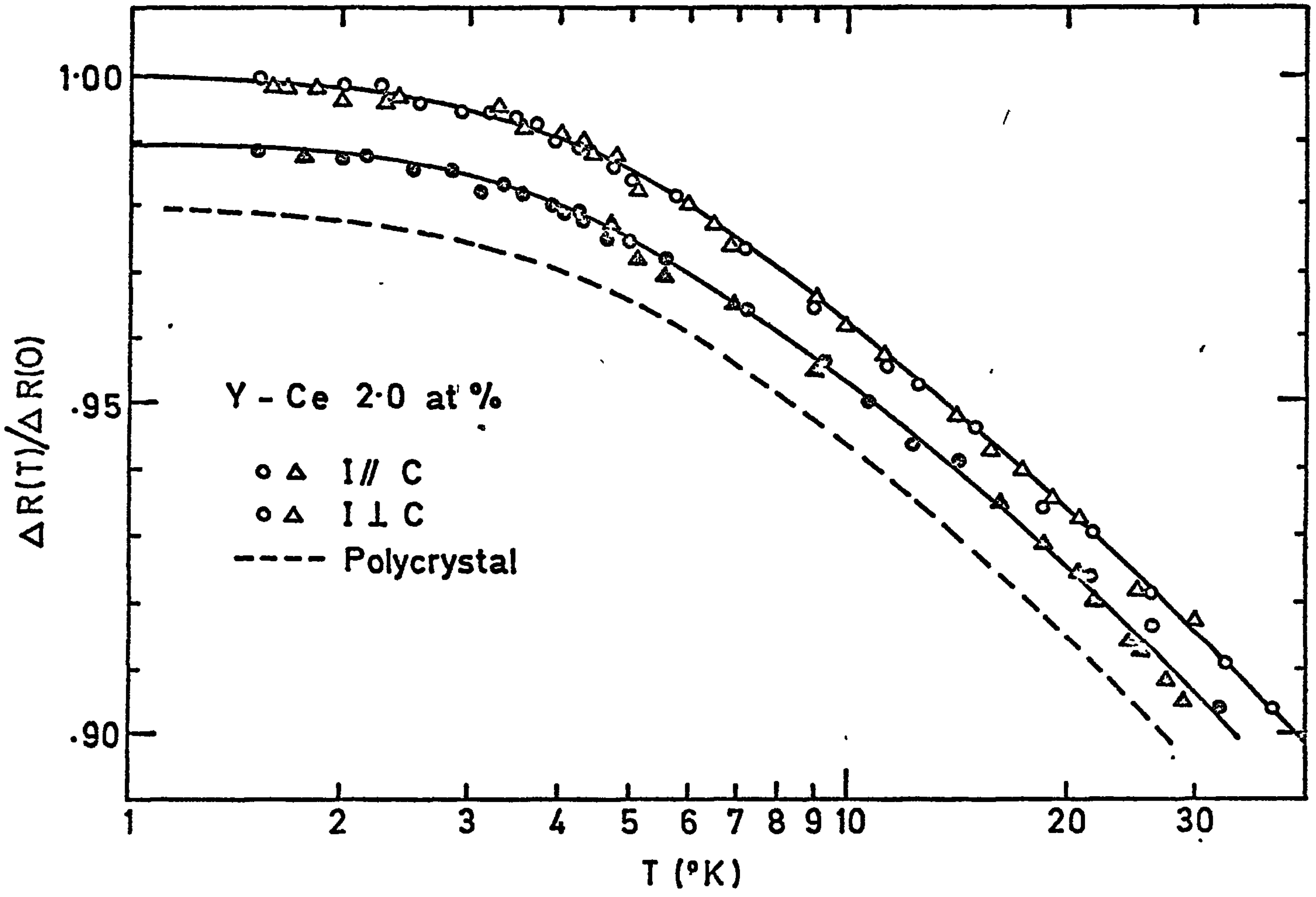

FIG. 6·8. The normalized solute resistivity for the directions parallel (I // C) and perpendicular (I ⊥ C) to the C axis. The vertical scales of the two lower curves have been shifted from the scale of the top curve by 0·01 and 0·02, respectively. [Sugawara and Yoshida 1971]

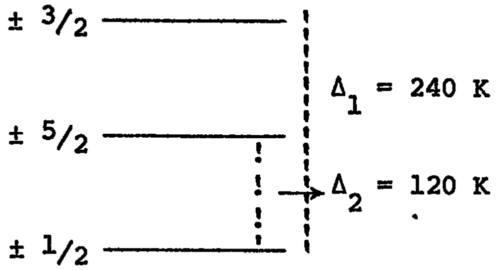

The energy-level diagram for the $^2F_{5/2}$ state of Ce^{3+} ion in yttrium proposed by Sugawara and Yoshida (1971).

The Y-Ce alloys become nonmagnetic at high pressures as it can be seen from the disappearance of the resistance minimum in Figure 6.9 (Coqblin 1971). This is again due to the increase of the 4f level with increasing pressure relative to the Fermi level.

6.7 Kondo Effect in some intermetallic compounds of cerium

A number of intermetallic compounds of cerium such as $CeAl_2$, Ce_3Al_{11} and $CeAl_3$ for which Γ, exchange interaction constant, has large and negative values show a Kondo effect. The behaviour of ρ, resistivity, as a function of temperature in the above mentioned compounds is presented in Figure 6.10 [van Daal, Maranzana and Buschow (1971)]. The gradual increase of ρ with decreasing temperature below about 15 K in $CeAl_2$ and 20 K in Ce_3Al_{11}, followed by a sharp maximum is considered to be due to the presence of the Kondo effect in the paramagnetic range. The sharp decrease in resistivity of $CeAl_2$ (< 4 K) and Ce_3Al_{11} (< 6 K) is attributed to the magnetic ordering. In $CeAl_3$, with decreasing temperature, a gradual increase of ρ, starting below room temperature, continued down to about 35 K and reaches a

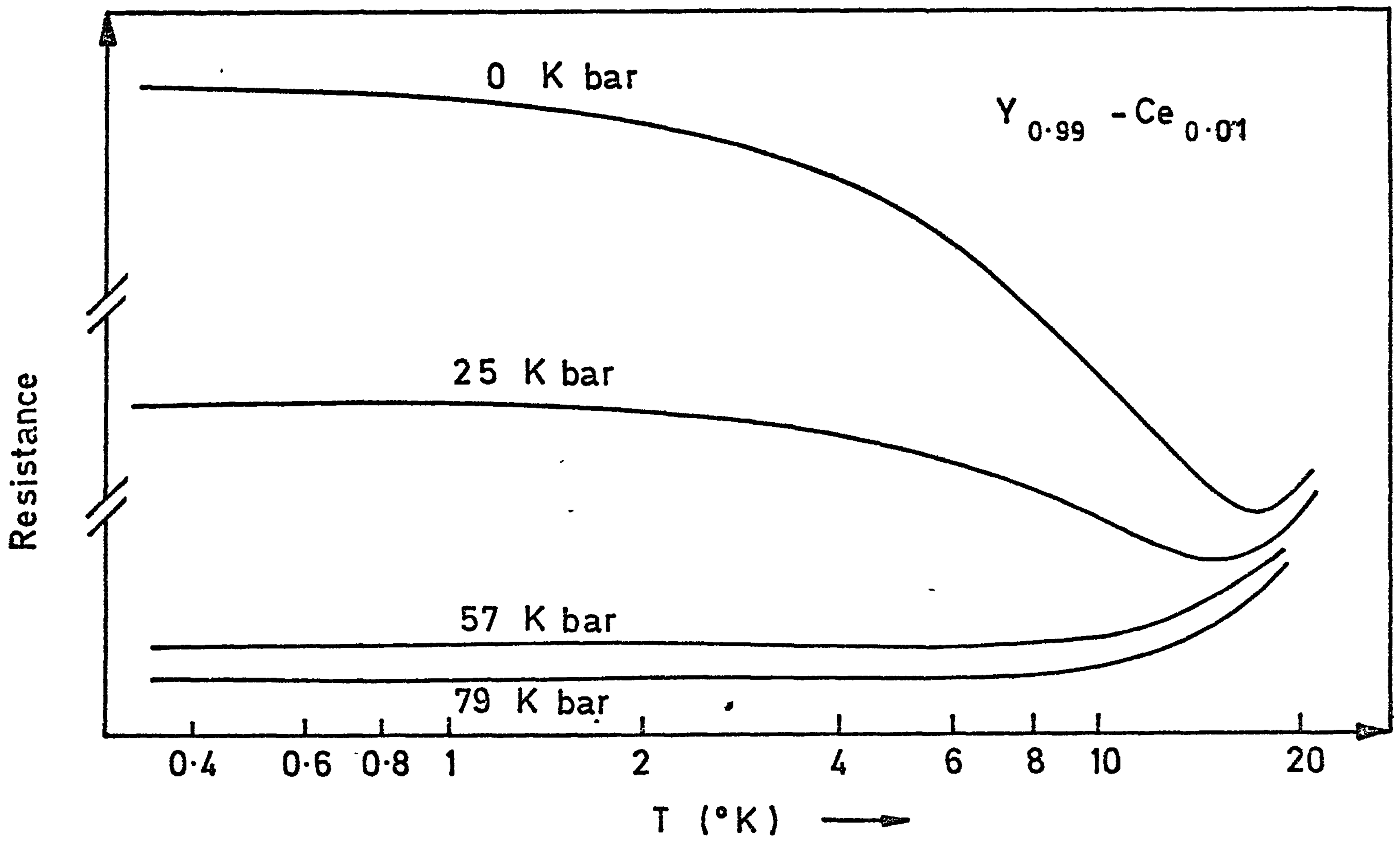

FIG. 6·9. Resistance (in arbitrary units) of Y-Ce alloy for different pressures. [Coqblin 1971]

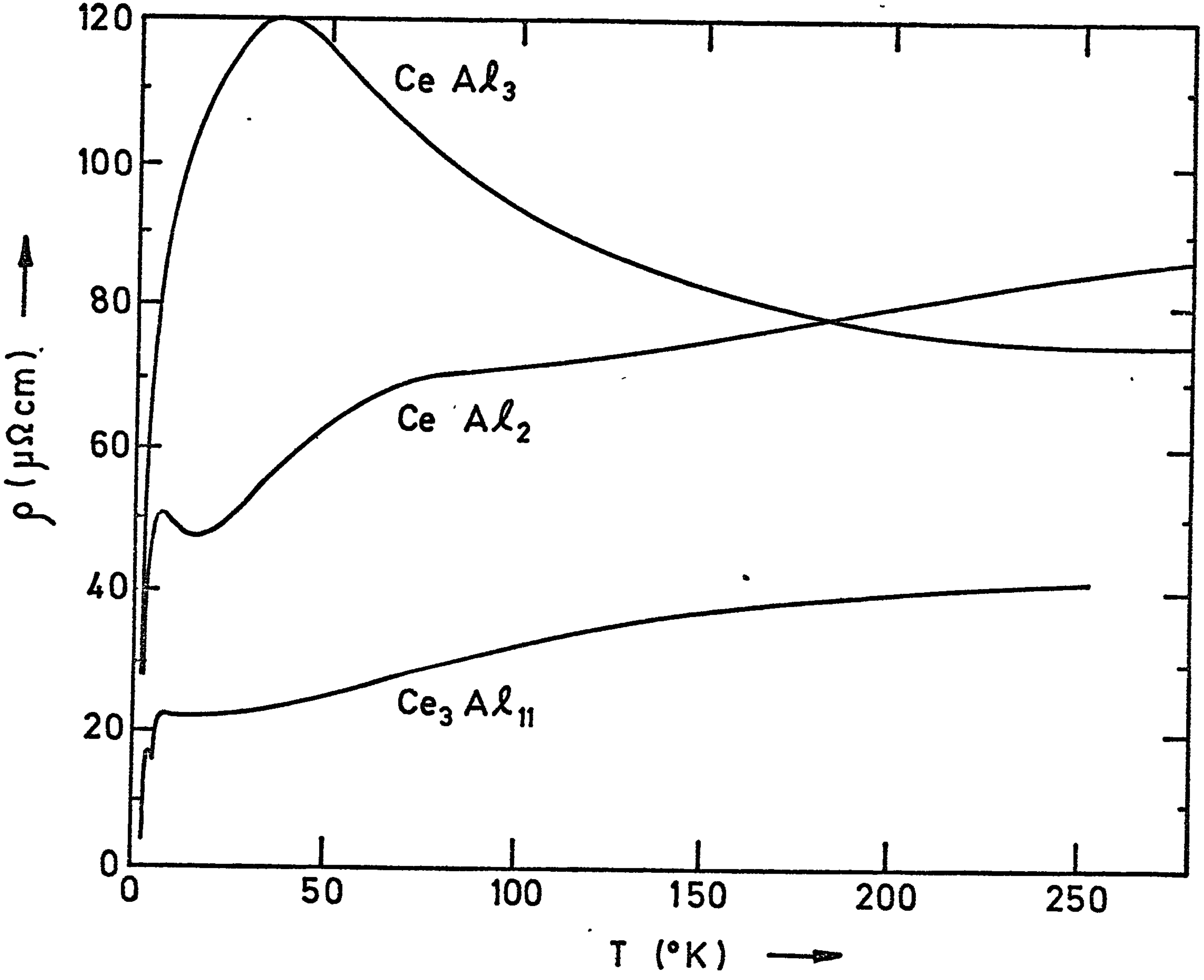

FIG. 6·10. The presence of Kondo effect in Ce_3Al_{11}, $CeAl_2$, $CeAl_3$. [van Daal et al. 1971] maximum and then falls rapidly. No magnetic ordering has been reported for $CeAl_3$ at low temperatures.

The observed temperature dependence of the electrical resistivity of $CeAl_3$ has been explained in terms of the "Kondo sidebands" by Buschow, van Daal, Maranzana and van Aken (1971). They have proposed that, in $CeAl_3$ the hexagonal crystalline electric field splits the Ce^{3+} ground multiplet in such a way that the doublet $|\pm 3/2>$ is the lowest. The relative position of the levels is such that Kondo sideband effects lead to two resonant peaks in the resistivity. The peaks merge together to one broad peak, the two peaks corresponding to the pairs of doublets $<\pm 3/2|$, $|\pm 1/2>$ and $<\pm 3/2|$, $|\pm 5/2>$. The normal Kondo effect due to the $|\pm 1/2>$state is quenched at temperatures which are low in comparison to the total splitting because this state is practically unoccupied.

The resistivity should exhibit not only a maximum but also a minimum at a lower temperature according to Cornut and Coqblin (1972) in view of the combined effect of a crystalline electric field and the Kondo scattering. In order to clarify this point Edelstein, Tranchita, McMaster and Gschneidner (1974) measured the resistivity behaviour of $CeAl_3$ down to 0.4 K. This is shown in Figure 6.11 with the theoretical prediction based upon the work of Cornut and Coqblin. As is seen, the expected minimum does not occur down to 0.325 K and it is difficult to understand the data with the proposed theory.

In these last three sections, we have seen that La-Ce and Y-Ce alloys show Kondo effect but do not possess the dramatic

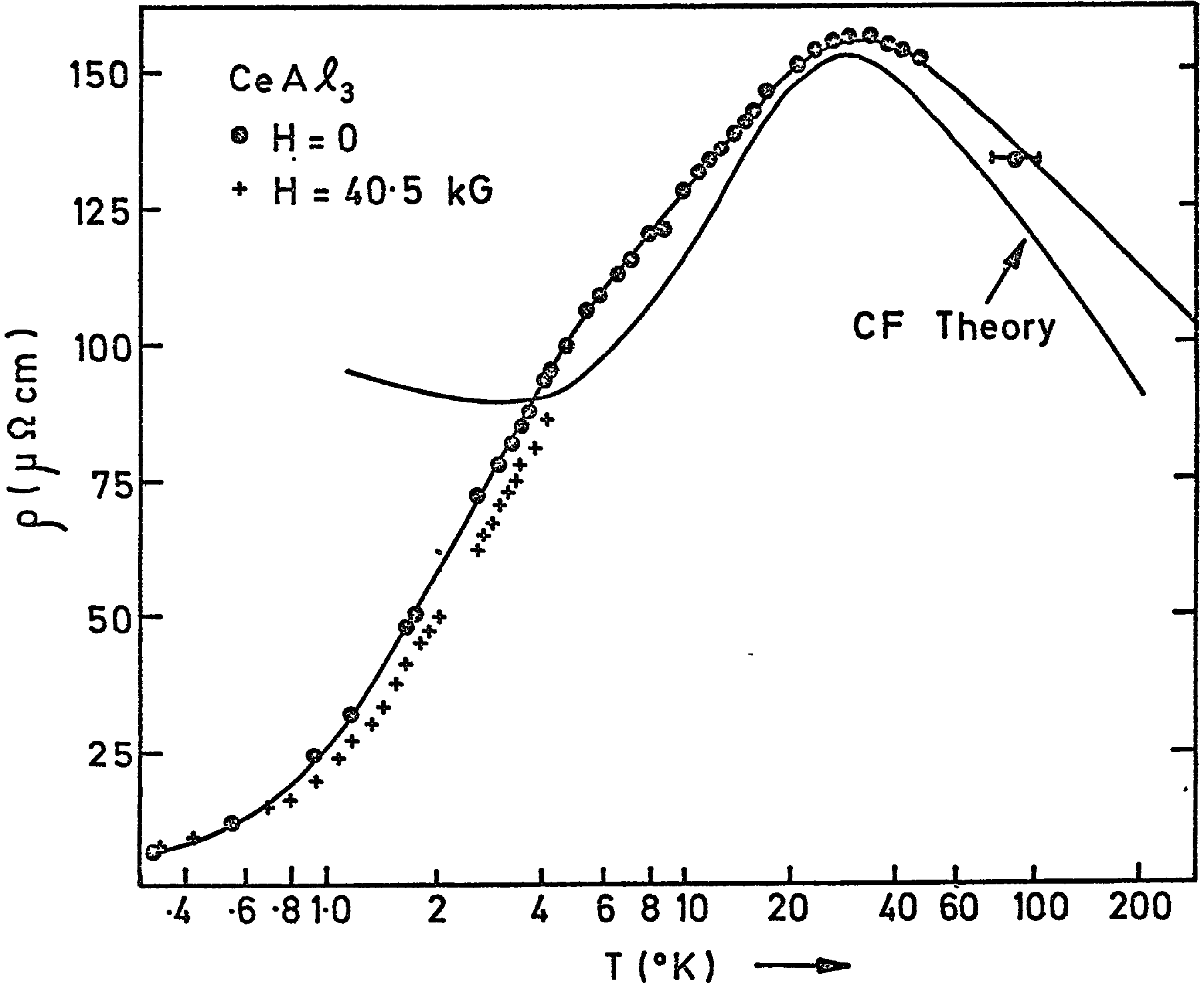

FIG. 6·11. Resistivity of $CeA\ell_3$ for H = 0 and H = 40·5 kG. [Edelstein et al 1974.]

"sidebands" structure in the electrical resistivity as it is suggested for intermetallic compounds of cerium. Kondo effect in some intermetallic compounds of cerium is reviewed by van Daal and Buschow (1970).

CHAPTER 7

RESULTS AND DISCUSSION OF ELECTRICAL PROPERTIES OF Pr-Ce ALLOYS

7.1 Results

The electrical resistivity of praseodymium-cerium alloys containing up to 25 at.% cerium has been studied in the temperature range 1.3 - 300 K. Alloys of six concentration were made, namely 0.5, 2, 5, 10, 20 and 25 at.% Ce. The position of the dhcp - fcc phase boundary in the Pr-Ce alloys has been discussed in Chapter 4. Since the transition from dhcp to fcc occurs beyond 67% at Pr, the alloys which we have studied can therefore be expected to occur in the double-hexagonal close packed phase at room temperature.

In Chapter 2.2, the necessity of making corrections for the non-uniformity of the current flow in the specimen was pointed out for the calculation of the resistivity from the measured resistance. This is because of the limited size of the available specimens. The dimensions of the samples appear to satisfy the conditions sufficiently well for Eq. 2.1 to be an adequate approximation. Table 7.1 gives a summary of specimen dimensions. The percentage corrections estimated using Eq. 2.1 are listed in Table 7.2. The correction for the 20 at.% Ce specimen appears to be the largest because it has a rather small value

Table 7.2: Percentage corrections for non-uniform current flow.

at.% Ce	0	0.5	2	5	10	20	25
% correction	-2.0	-1.1	-0.3	-0.5	-1.6	-5.3	-1.9

At.% Ce	t	2w	s	d	$e^{\frac{\pi d}{w}}$	$e^{\frac{\pi d}{t}}$	$\frac{\rho_o}{\rho}$
0	0.228 cm	0.452 cm	0.740 cm	0.217 cm	20.4	19.9	1.020
0.5	0.197	0.185	0.569	0.191	660	21.0	1.011
2	0.121	0.306	0.673	0.210	74	233	1.003
5	0.148	0.278	0.595	0.189	72	55	1.005
10	0.115	0.392	0.443	0.183	18.7	147	1.016
20	0.205	0.180	0.331	0.133	103	7.66	1.053
25	0.185	0.187	0.479	0.155	182	13.8	1.019

Table 7.1: Summary of specimen dimensions (Pr-Ce). ρ_o and ρ are the apparent and the corrected resistivity respectively.

of d (the separation of neighbouring current and potential leads) and large value of t (thickness). In no case does the correction exceed 6%, and so it is believed that the approximation used should be reasonably valid.

The derived alloy resistivities as a function of the alloy concentration x at room temperature and at 95°C are shown in Fig.7.1. It will be seen that on this enlarged scale the results are rather scattered. The principal reason for this is the occurrence of random errors in measuring the specimen dimensions using a travelling microscope, the errors in measuring the specimen resistance R being considerably less. Error bars calculated from the scatter of the observed dimensional data are given in Fig. 7.1, and are typically of order ± 2.5%. Despite careful measurements it was found difficult to reduce the errors much below this, largely because of the intrinsic roughness of the specimen surfaces and corners. An error of 2.5% in a thickness of 1 mm corresponds to about 10^{-3} inch, which is a typical machining tolerance. Perhaps polishing the specimen surfaces might have improved matters in this respect. Since the temperature variation of the resistance R of a specimen can be measured to considerably better accuracy than this, it seems valid to smoothly rescale the results of Fig. 7.1 in order to exploit the inherently greater precision of the temperature variation of resistivity. To this end, the results have been fitted by least squares regression using the error-bar of each point as a weighting factor. Thus we find:

$$\left.\frac{\partial\rho}{\partial x}\right|_{T=296\ \mathrm{K}} = (0.23 \pm 0.06)\ \mu\Omega\,\mathrm{cm/at.\%\ Ce.}$$

$$\left.\frac{\partial\rho}{\partial x}\right|_{T=368\ \mathrm{K}} = (0.19 \pm 0.06)$$

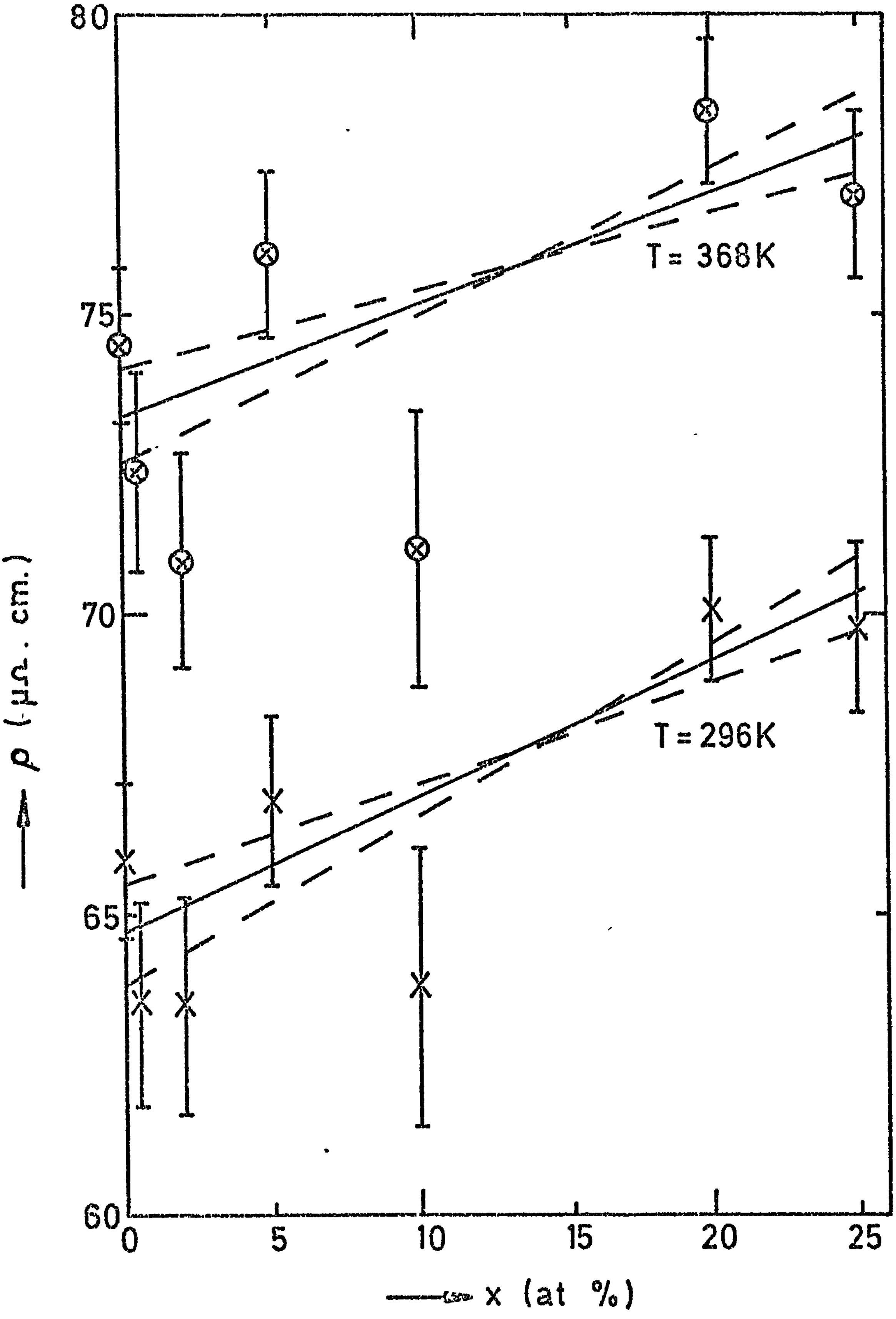

Fig. 7.1: The resistivity of Pr-Ce alloys as a function of Ce concentration.

The best straight lines corresponding to these gradients are shown in Fig. 7.1 together with lines showing estimates of the errors in the gradient. The data points are well fitted by the linear variation within the limits of the error bars. Within experimental error the gradients at room temperatures and 95°C are equal, but on our assumption that the resistivities can validly be rescaled to the best straight lines, the difference in gradients between room temperature and 95°C may be significant.

On this basis, all subsequent resistivity data have been rescaled by the appropriate factors to smooth the scatter in Fig.7.1. The temperature dependence of the resistivity, $\rho(T)$ for pure praseodymium and the six alloys plotted between 1.3 K and 300 K is shown in Fig. 7.2. Fig.7.3 is an expanded plot of the region up to 50 K, and clearly shows the existence of a Kondo effect below about 4 K in the 0.5, 2, and 5 at.% cerium alloys. The 10% alloy resistivity, however, is virtually flat below about 5 K and the 20 and 25% alloys show an increasingly sharp drop in resistivity below about 4 K with no sign of the conventional Kondo effect evident in the more dilute alloys.

Figures 7.1, 7.2 and 7.3 are all results obtained not on the initial low temperature run on each specimen, but during subsequent runs, after they had been thermally cycled between 1.3 and 300 K several times, usually with some weeks or months intervening. In these runs there is no sign of the antiferromagnetic transition reported by Meaden, Krithivas and Sze (1972).

However, it should be recorded that this transition has been observed in certain of the specimens after recent annealing and during the first low temperature run on these specimens. The

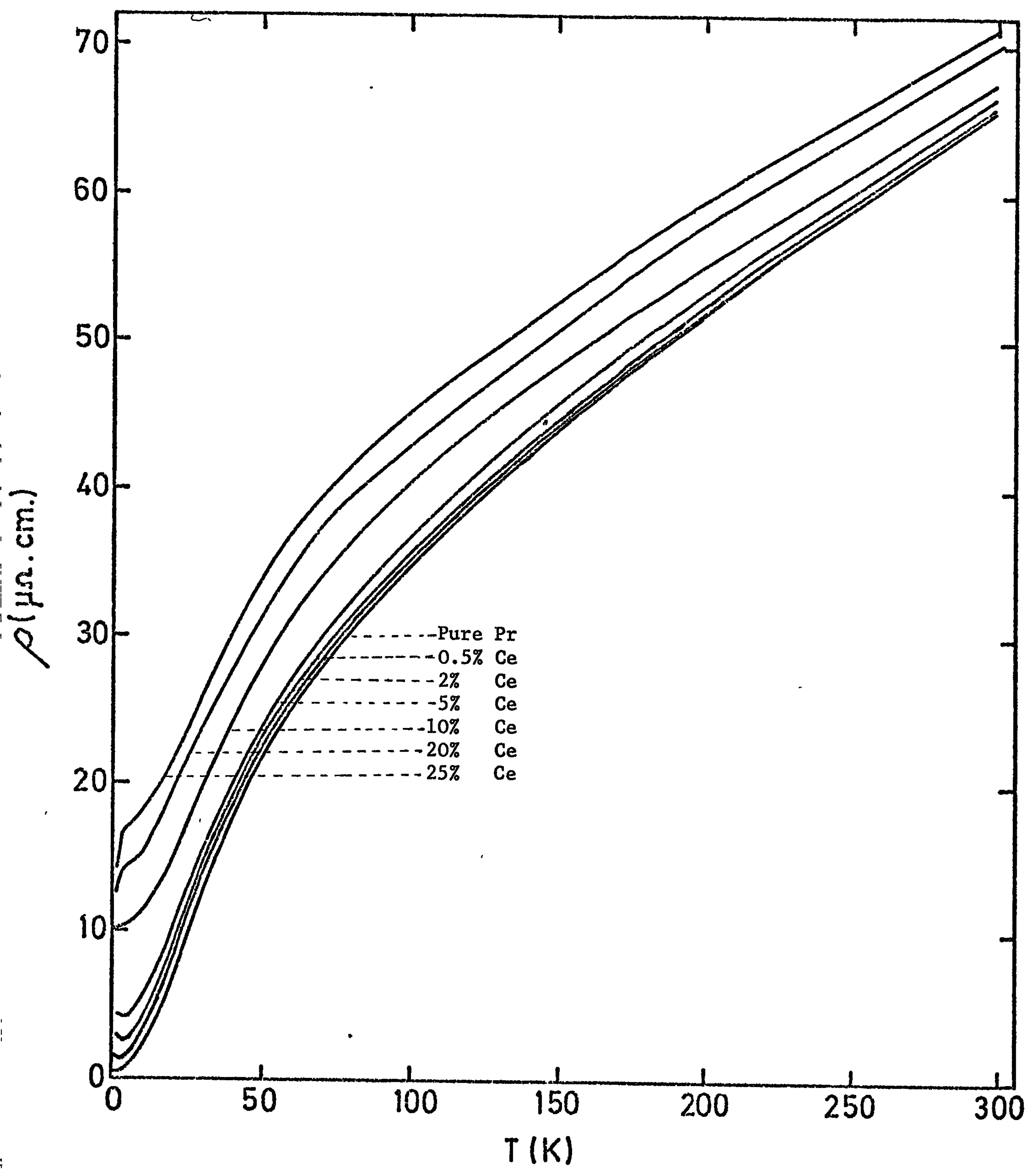

Fig. 7.2: The resistivity of Pr-Ce alloys as a function of temperature

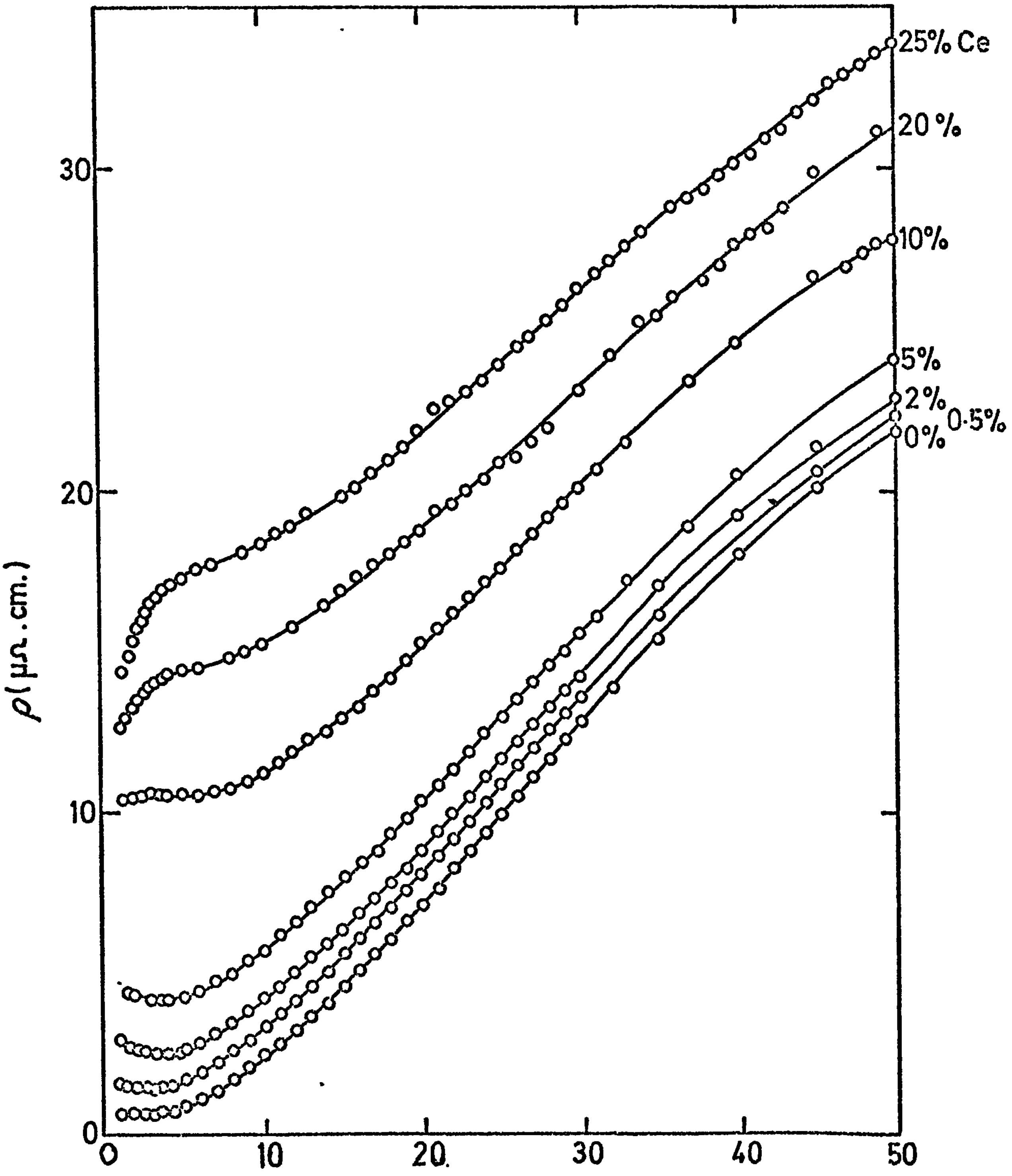

Fig. 7.3: An expanded plot of Fig. 7.2 in the range 1.3 - 50 K.

results of such observations are shown in Fig. 7.4 for pure praseodymium and the 5 and 10 at.% cerium alloys. It is noteworthy that the 5 at.% Ce alloy still shows a Kondo effect while exhibiting signs of antiferromagnetic ordering at about (26 ∓ 1) K. Within experimental error, there appears to be no considerable shift in the transition temperature with cerium concentration. The appearance of the transition seemed to be very evanescent in that it was not observable on the subsequent runs for these same three specimens.

There seems no reason to believe that it was not also present in the other alloys but unfortunately the necessity of making measurements immediately after annealing was not fully appreciated at the time the original results were taken.

Results of the electrical resistivity of Pr-Ce and La-Ce alloys in the temperature range 0°C to 800°C have been discussed in Chapter 4 in connection with structural phase transformations.

From Fig. 7.2 one can see that the general shape of the resistivity curve for pure praseodymium is very similar to that found by James, Legvold and Spedding (1952) and by Krithivas, Meaden and Sze (1972), but differs from that observed by Alsted, Colvin, Legvold and Spedding (1961), who found an abrupt increase in the slope of 61 K and a decrease at 95 K.

After the annealing process, the resistivity of pure Pr at 1.3 K was found to be 0.7 μΩ cm (Table 7.3). This figure is significantly lower than others reported in the literature except for that of Krithivas et al. (1972) which is about 0.5 μΩ cm .

7.2 Discussion: Total Resistivity of a paramagnetic binary alloy

In attempting to analyse the present results, we are faced

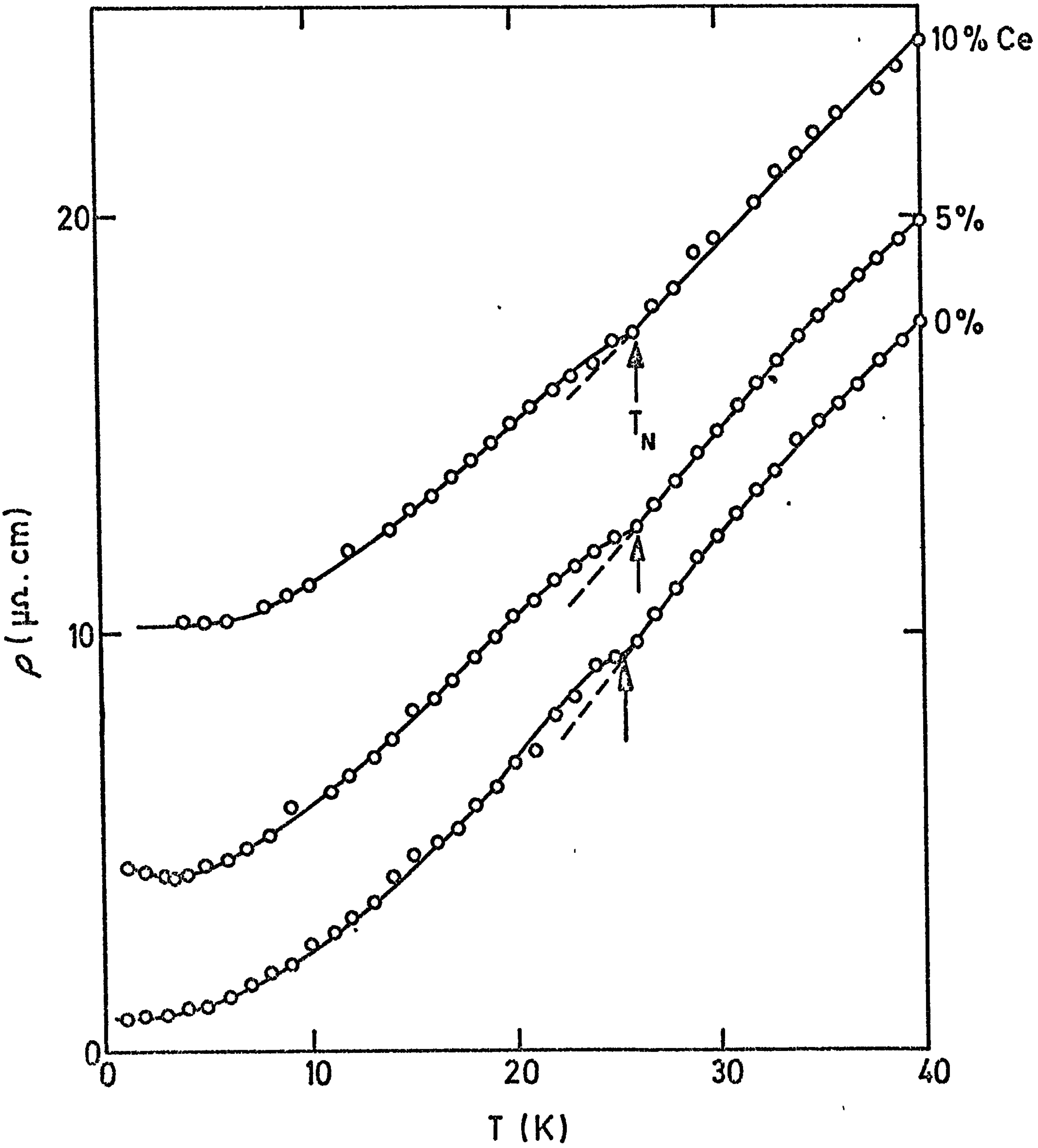

Fig. 7.4: The low temperature resistivity of Pr, 5 and 10 at.% Ce alloys, showing an antiferromagnetic transition

T ($^{\circ}$ K)	ρ_{Total} ($\mu\Omega$ cm)						
	Pr	$Pr_{.995}Ce_{.005}$	$Pr_{.98}Ce_{.02}$	$Pr_{.95}Ce_{.05}$	$Pr_{.90}Ce_{.10}$	$Pr_{.80}Ce_{.20}$	$Pr_{.75}Ce_{.25}$
1.3	0.703	1.580	2.771	4.488	10.21	13.23	14.81
4.2	0.772	1.509	2.454	4.367	10.32	14.59	17.63
10	2.415	3.36	4.23	5.95	11.13	15.52	18.92
15	4.56	5.56	6.36	8.16	13.07	17.19	20.31
20	7.07	7.99	8.84	10.39	15.04	19.12	22.51
25	9.82	10.79	11.62	12.29	17.13	21.19	24.60
30	13.23	13.50	14.09	14.86	19.62	23.56	27.67
40	17.22	18.77	18.96	19.84	24.31	28.11	31.03
50	21.51	22.12	22.62	23.98	28.12	31.86	36.48
75	28.82	29.32	30.02	30.83	35.45	38.90	41.50
100	33.99	34.56	35.10	36.64	40.14	43.32	45.95
125	38.96	39.32	39.83	41.46	44.81	47.58	50.02
150	43.24	43.65	44.15	45.40	48.53	51.55	53.52
175	47.46	47.50	48.10	49.60	52.00	55.18	57.30
200	51.15	51.40	51.90	53.30	55.51	58.75	60.61
225	54.78	54.88	55.40	56.60	58.62	61.88	63.72
250	58.06	58.40	58.80	60.00	61.71	65.14	66.61
275	61.38	61.48	62.20	63.30	64.83	67.55	69.12
300	64.53	64.70	65.10	66.10	67.07	69.03	71.14

Table 7.3: Some selected values of ρ(T) at different temperatures.

with the problem of separating out the different contributions to the total alloy resistivity. Dekker (1965) has treated the spin disorder resistivity of a paramagnetic binary alloy ($Pr_{1-x}Ce_x$ in our case) on the basis of Matthiessen's rule and the Nordheim approximation and has obtained an expression for the total resistivity equivalent to:

$$\rho(T) = \rho_{ph}(T) + (1-x)\rho_{Pr}{}^{m}(T) + x\,\rho_{Ce}{}^{m}(T) + x(1-x)\rho_{v} \qquad (7.1)$$

where ρ_{ph} is the phonon contribution, ρ^{m} is the total spin disorder resistivity (including the Kondo term arising from the second Born approximation), and ρ_{v} is simply due to potential scattering from the impurity ions. The spin disorder terms are expected to be temperature dependent on account of the modification by the crystalline electric field splittings. At this point it should be noted that the use of Matthiessen's rule for such alloys is not beyond question. For example, Fulde and Peschel (1972) give a rather sophisticated calculation of the first and second order spin disorder resistivities due to a crystalline electric field split impurity ion with a singlet ground state in which even the first order resistivity violates Matthiessen's rule to an extent depending on the ratio of exchange to potential scattering. However, for simplicity such a possibility will be neglected in what follows. Thus in the light of Eq. 7.1 we hope to be able to calculate the spin disorder solute resistivity of cerium in the double-hexagonal close packed environment afforded by the praseodymium host from the equation:

$$\rho_{Ce}{}^{m}(T) = \frac{1}{x}\,[\rho(T) - \rho_{ph}(T) - (1-x)\,\rho_{Pr}{}^{m}(T)] \;-\; (1-x)\,\rho_{v} \qquad (7.2)$$

In general, we have no unambiguous way of separating out ρ_v from our results since the presence of the Kondo effect and probably absence of magnetic ordering at low temperatures prevent the strict determination of residual resistivities for the alloys. Therefore, we have to be satisfied with leaving out the last term of Eq.7.2 in the hope that it is constant, which should be true to a good approximation for the dilute alloys.

7.3 The Phonon Resistivity

One is faced with the problem of how to separate out the phonon contribution from the total resistivity. In the case of heavy rare earths [see, for example, Smidt and Daane (1963), Popplewell, Arnold and Davies (1967)], this presents little problem. The high temperature resistivity tends to a constant slope $(\partial\rho/\partial T)$, which may be fitted to the usual Bloch-Grüneisen expression. The case of light rare earths (including lanthanum) is much more difficult since here $\rho(T)$ has a strong downwards curvature up to the melting point [Spedding, Daane and Herrmann (1957)]. It is also apparent from Fig.7.2 and Fig.4.1 that in the paramagnetic region the resistivities of praseodymium and the Pr-Ce alloys increase more slowly than would have been supposed from a linear law. Two approaches, neither of which seems very satisfactory, have been suggested in the literature. Watabe and Kasuya (1969) in discussing the spin disorder resistivities of pure praseodymium and neodymium, suggested that their phonon resistivities might be taken to be rescaled values of the resistivity of pure lanthanum as measured by Alstad, Colvin, Legvold and Spedding (1961).

$$\rho_{ph}(T) = \alpha \rho_{La}(T) \qquad (7.3)$$

The scaling factor α was adjusted so as to fit as closely as possible the shape of $\rho_{ph}(T)$ to that of $\rho(T)$ for praseodymium and neodymium at temperatures above about 100 K where the spin disorder resistivity is taken to have saturated. The philosophy behind this approach is that solid lanthanum is supposed to be nonmagnetic, its 4f levels lying above the Fermi level and therefore being unoccupied, and should thus have a resistivity composed of merely residual plus phonon contributions. In addition its electronic band structure and lattice dynamics should be very similar to those of the other light rare earths, and consequently its phonon resistivity should also be very similar. The disturbing feature of this method of fitting, however, is that rather drastic values of the rescaling factor α are required, being of the order 0.7 for both praseodymium and neodymium, the resistivity of lanthanum as given by Alstad et al. (1961) being actually larger at 300 K than that of either praseodymium or neodymium. The resistivity of lanthanum given by Alstad et al. (1961) is shown in Fig.7.5.

An alternative approach was suggested by Meaden et al. (1972) in which an expression of the form:

$$\begin{aligned}\rho_{Pr}(T) &= \rho_{Pr}^{m}(\infty) + \rho_{ph}(T) \\ &= \rho_{Pr}^{m}(\infty) + A\,T\left[1 - \left(\frac{T}{T_o}\right)^2\right]\end{aligned} \qquad (7.4)$$

was fitted to the high temperature behaviour (between about 100 and 300 K) of pure praseodymium. $\rho_{Pr}^{m}(\infty)$ is here the high temperature limit of the spin disorder resistivity, and A and T_o are treated as adjustable parameters. As pointed out by Meaden, this expression is

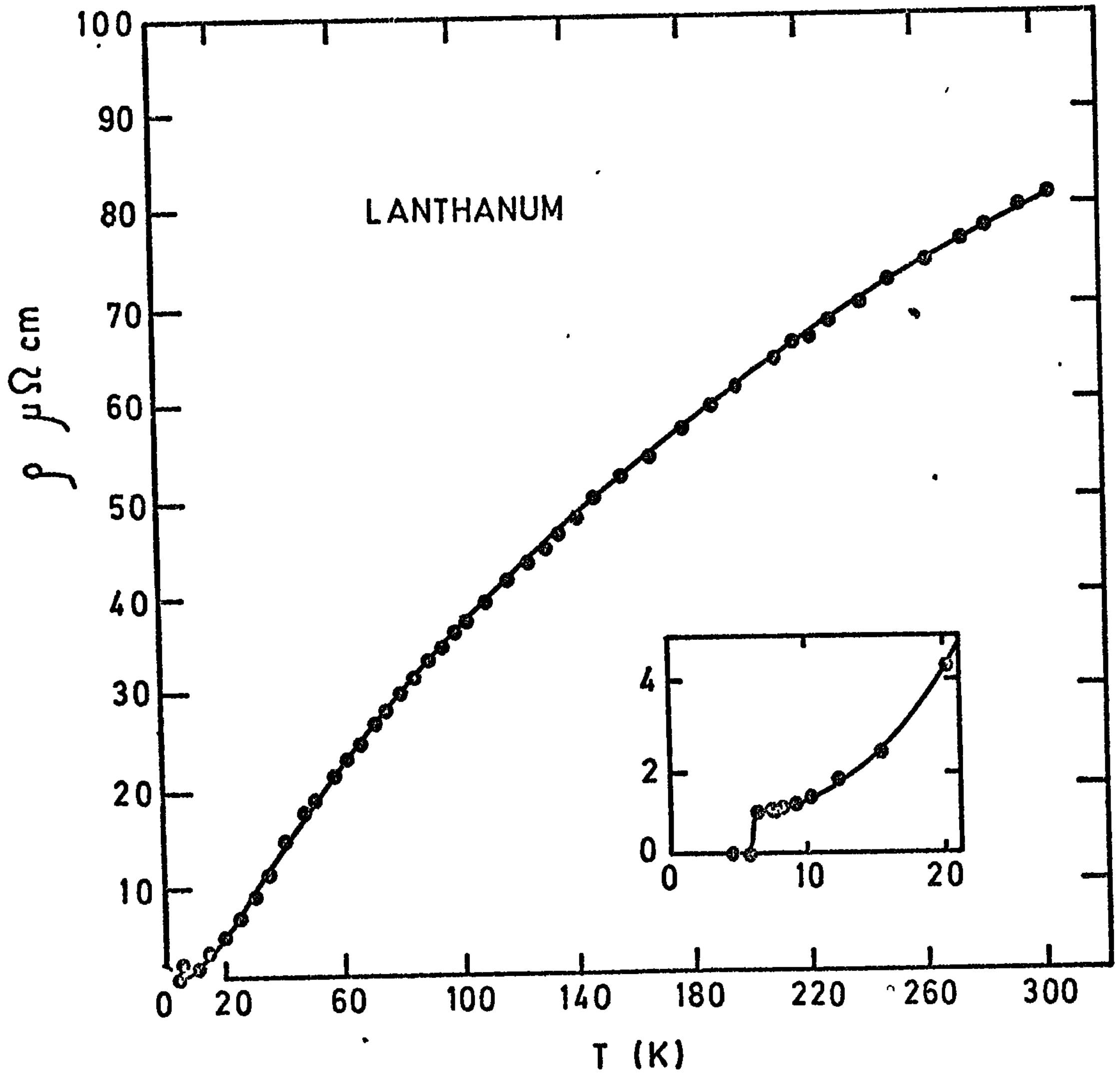

FIG. 7.5. The electrical resistivity of La vs temperature [Alstad et al. 1961]

well known to be a good representation of the phonon resistivity of the transition metals where T_o is related to the energy interval over which the density of states of the d-band is significantly curved, and is therefore rather a high temperature; but there is little fundamental reason to consider such an expression applicable to the rare earths. Also the value of T_o which Meaden finds necessary to fit his data, namely 580 K, is too low for the explanation to be tenable. He therefore almost retreats to the position of regarding equation 7.4 merely as an empirically useful fitting formula. Another problem with Meaden's approach is that it should be possible to fit the lanthanum data with an equation analogous to equation 7.4, but with $\rho_{La}{}^{m}(\infty) = 0$. Using this method an attempt has been made to evaluate the parameters leading to best values of: $\rho_{La}{}^{m}(\infty) = 13\ \mu\Omega\,\mathrm{cm}$, $A = 0.262\ \mu\Omega\,\mathrm{cm}\ K^{-1}$, $T_o = 784$ K for the data of Alstad et al. (1961). Hence it must be concluded either that lanthanum has a finite spin disorder resistivity at high temperatures, or that Eq.7.4 is an inadequate representation of its phonon resistivity. It is conceivable that if the 4f levels in lanthanum happen to lie sufficiently close to, but above, the Fermi level, there could be a form of spin disorder scattering which would set in at high temperatures. On the other hand, it might be that there is some unknown subtlety in the phonon resistivity of lanthanum which prevents good description by existing theories; if so, such would probably be true of praseodymium.

In view of the apparent absence of a reasonable theory of resistivity of lanthanum, it was preferred to adopt the approach of Watabe and Kasuya and use Eq.7.3 for the phonon resistivity. The data for pure praseodymium given in Fig.7.2 were fitted with equation 7.4 and best values of : $A = 0.179\ \mu\Omega\,\mathrm{cm}\ K^{-1}$ and $T_o = 860$ K were obtained.

These are to be compared with the values given by Meaden et al. (1972) of A = 0.2 $\mu\Omega$ cm K^{-1} and T_o = 580 K respectively. A plot of the equation $\rho(T) = 0.179\ T\ [1 - (T/860)^2]$ is shown in Fig.7.6 with the resistivity of pure praseodymium and of ($0.696\ \rho_{La}$). It appears to us that Meaden et al's choice of T_o introduces rather too much downward curvature of the phonon term at $T > 240$ K as is evident from Fig.1 of their paper [Meaden et al. (1972)].

Also curious is the rather low value he obtains for the absolute resistivity at T = 270 K, namely about 51 $\mu\Omega$ cm compared with a value from the present measurements of about 61 $\mu\Omega$ cm and that of Alstad et al. (1961) of about 63 $\mu\Omega$ cm. Meaden believes this occurs because his sample has a lower residual resistivity (0.45 $\mu\Omega$ cm) than that of Alstad et al., although the latter authors do not mention a figure for this quantity. The residual resistivity of our annealed specimen (0.7 $\mu\Omega$ cm) does not appear to be significantly worse than that of Meaden's.

One can see that for the given values of A and T_o, Eq.7.4 reduces to a linear form at very low temperatures. In fact this does not represent the phonon resistivity of praseodymium at very low temperatures. The logarithmic plot of $\rho(T) - \rho_o$, where ρ_o is the residual resistivity, for praseodymium is shown in Fig.7.7. Table 7.4 shows the coefficient of T in the expression $\rho = C\ T^n$ for pure praseodymium, 10 and 25 at.% cerium alloys. The present low temperature result for pure Pr ($n = 3.69 \pm 0.05$) is in good agreement with that of Arajs and Dunmyre (1967).

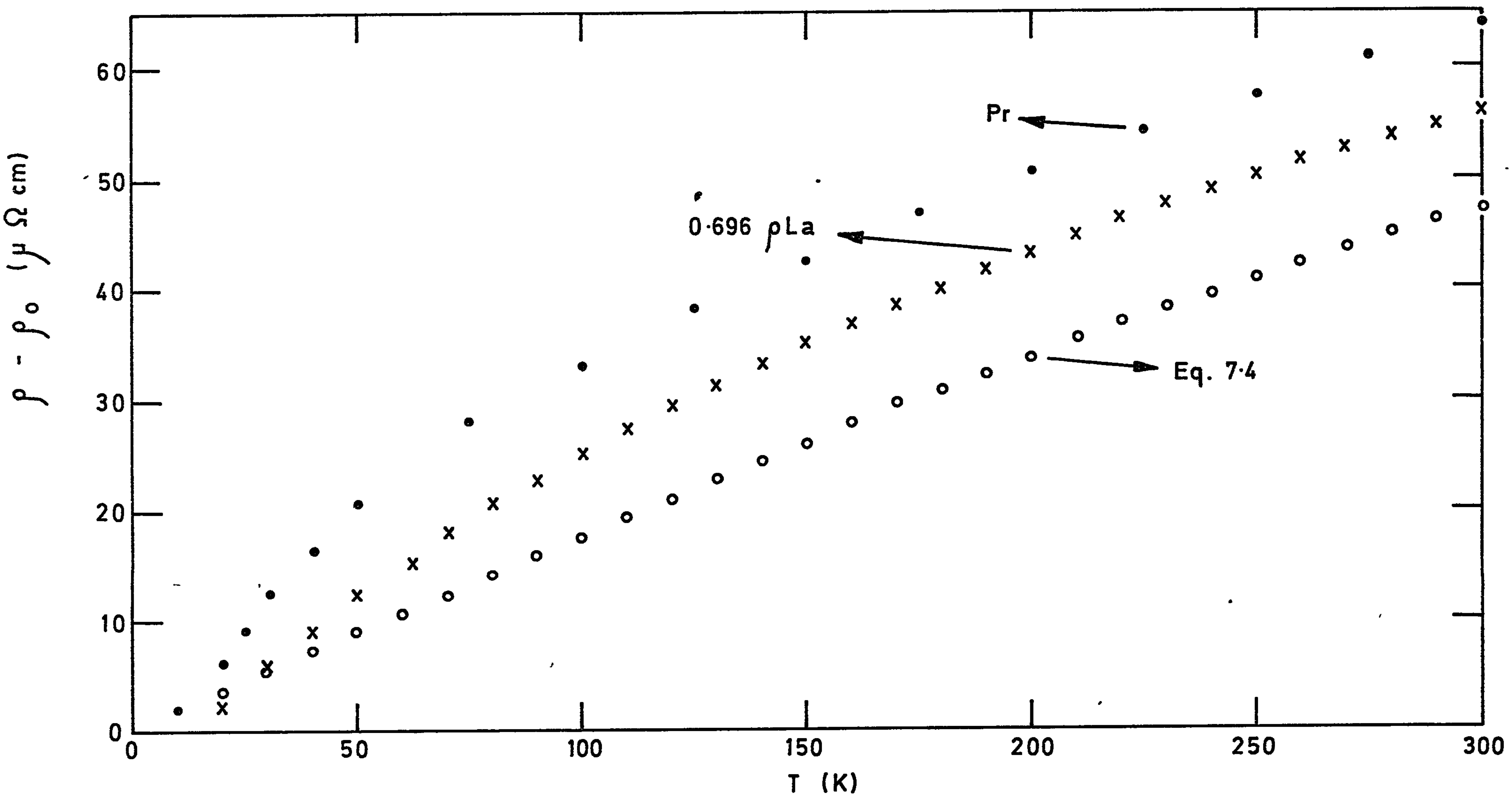

FIG. 7·6. The resistivity of Pr with the residual resistivity ρ_o subtracted as a function of temperature T.

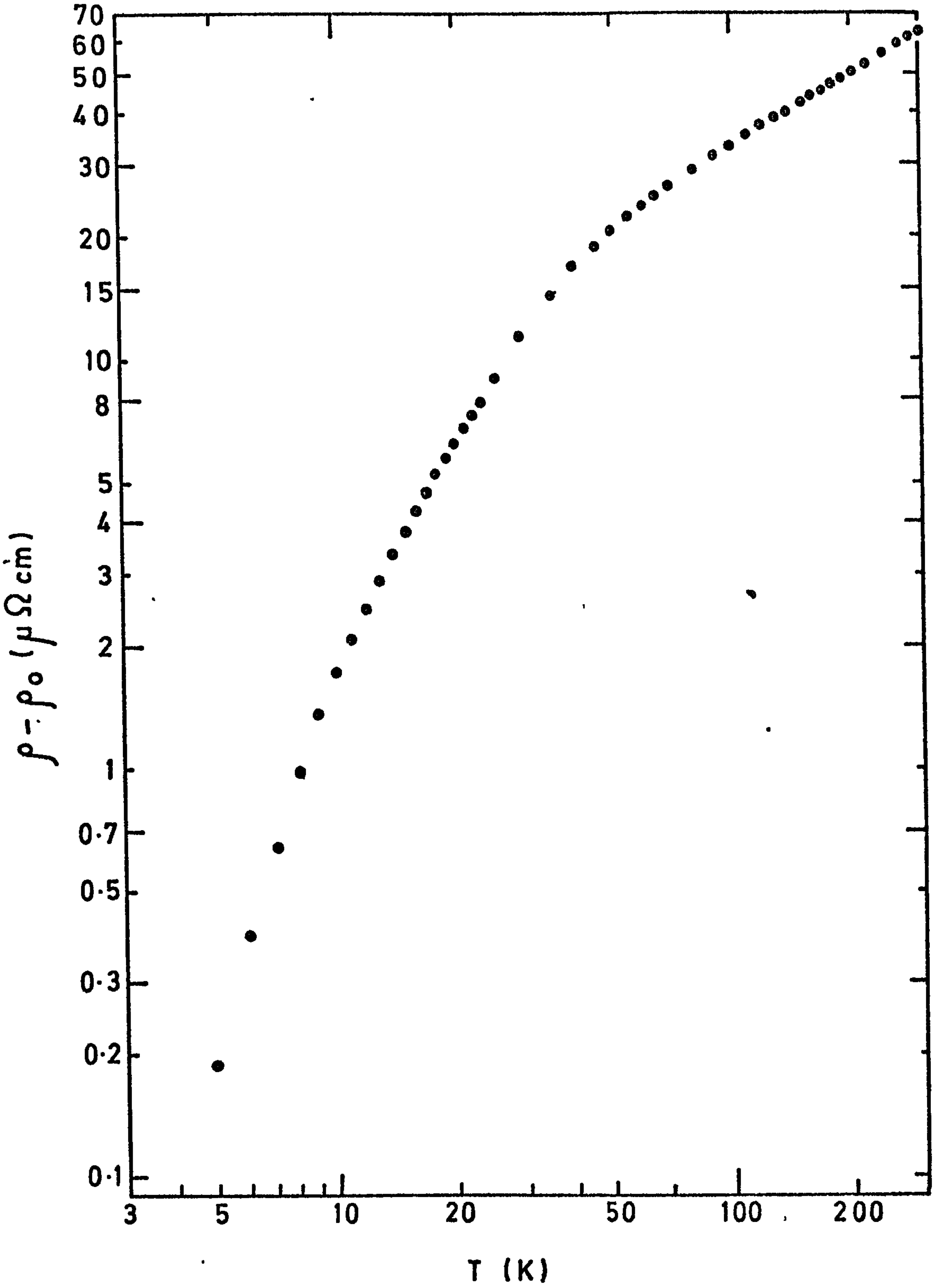

FIG. 7·7. Intrinsic electrical resistivity ($\rho - \rho_0$) of Pr as a function of temperature T.

Table 7.4: The exponent of temperature in the phonon resistivity

at.% Ce	n (5 - 10 K)	n (11 - 20 K)
0	3.69 ± 0.05	1.95 ± 0.05
10	2.69 ± 0.05	1.96 ± 0.05
25	0.49 ± 0.06	1.85 ± 0.06

7.4 Spin Disorder or Magnetic Resistivity of Praseodymium

It is now possible to make an attempt at extracting the magnetic component of the electrical resistivity. In attempting to obtain the rescaling factor α suitable for the praseodymium specimen, the problem arises that the high temperature curvatures of the present praseodymium data and the lanthanum data of Alstad et al. (1961) differ slightly, as evidenced by the different values of T_o for best fits (T_o = 860 K and 784 K respectively). Thus the rescaling must be a slight compromise, and it was decided to take $\alpha = 0.696$, a value similar to that used by Watabe and Kasuya (1969). The spin disorder resistivity calculated for pure Pr is then shown as the lower curve of Fig.7.8. Also shown are the high temperature limiting values of Meaden et al., and of Watabe and Kasuya, with which the present results agree fairly satisfactorily. In accord with both these sets of authors, it is found that the spin disorder term saturates above about 60 K. The inexactitude of fit of the shapes of the praseodymium and lanthanum data at high temperatures is manifest as a slight downward bowing (by about 1 $\mu\Omega$ cm) of the curve at around 160 K. By a

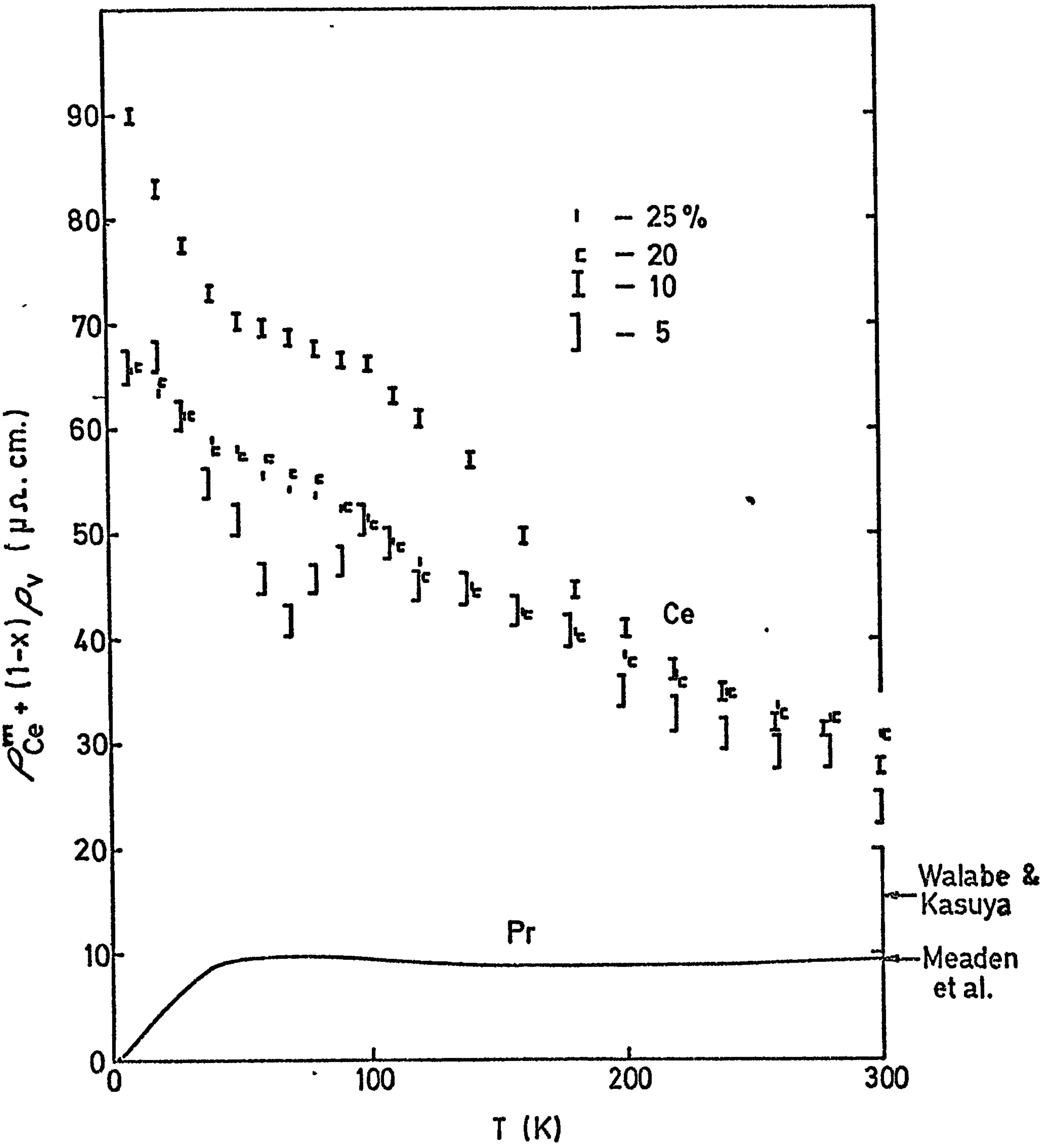

Fig. 7.8: The calculated temperature variation of the spin-disorder resistivity of Pr and of the Ce solute normalised to concentration X in the range 1.3 - 300 K.

consideration of the possibility of using a lanthanum specimen with high resistivity (because of observed mixed dhcp and fcc phases in the specimen) Meaden et al. have interpreted the high value for the magnetic resistivity of praseodymium found by Watabe and Kasuya.

The spin disorder resistivities of the heavy rare earth metals are found to be constant and proportional to the de Gennes factor $(g-1)^2 J(J+1)$ above the magnetic transition temperature. [See for example Smidt and Daane (1963)]. But in praseodymium the effect of the crystalline electric field is sufficiently important to modify the situation. As is evident from Fig.7.8 the spin disorder resistivity of praseodymium decreases below about 60 K according to what would be expected when the population of the crystalline electric field level of the Pr ions varies according to the Boltzmann law [Meaden et al. (1972)]. Without the crystalline electric field effect, the spin disorder resistivity would have remained constant down to about 26 K, the Néel point (Fig. 7.4). It should be noted that this temperature of $\sim$60 K agrees with the energy separation between the ground state and the first excited doublet on the hexagonal sites (63 K) found by Bleaney (1963).

7.5 Spin Disorder Resistivities of PrCe alloys

We now turn to the question of the subtraction of the phonon term in the alloys. Since praseodymium and cerium may be expected to be rather similar in their electronic and lattice dynamics, one would hope that the same scaling factor α would suffice for the alloys as for pure praseodymium. However, from the curves of Fig.7.2 it is evident that the high temperature slope decreases systematically with increasing cerium content. Plots of alloy resistivity versus $T[1 - (T/860)^2]$ were made at high temperature, and confirmed that this value of T_o still gave a satisfactory fit for all the alloys. A graph of the gradients of the plots so obtained is given in Fig.7.9 as a function of cerium concentration, from which the drop in gradient with increasing x is clear. Apart from the point for 10% Ce, the data are well fitted by a linear decrease with slope:

$$\frac{\partial A}{\partial x} = -(0.104 \pm 0.003)\ \mu\Omega\,\mathrm{cm}\ \mathrm{K}^{-1}$$

if the 10% Ce point is included the estimated error in slope rises to 0.02 $\mu\Omega$ cm K^{-1}. In passing, it should be noted that there is other evidence that the 10% Ce alloy may be somewhat anomalous in its behaviour; its room temperature resistivity is rather lower, and its resistivity at 4.2 K rather higher, than expected on the basis of a smooth variation with concentration (see the plot of $\rho(x)$ at 4.2 K shown in Fig.7.10). Possibly this alloy has some form of contamination, although we have no other evidence to support this point.

If the simple assumption is made that it is implausible that the phonon resistivity should be modified by as much as 15% in the 25 at.% cerium alloy (say) compared with pure praseodymium, since their electronic and phonon dynamics should be so similar, i.e. $\alpha = 0.696$ for all alloys, then Eq.7.2 may be used to calculate the cerium solute resistivity (plus the residual contribution). A plot of the resistivities ρ_{Ce}^{m} so calculated is shown up to 300 K as the upper curves in Fig.7.8 for the 5,10,20 and 25 at.% alloys; the error bars indicated correspond to absolute errors in the raw resistivities of ∿0.1 $\mu\Omega$ cm, a not unreasonable figure. Data for the

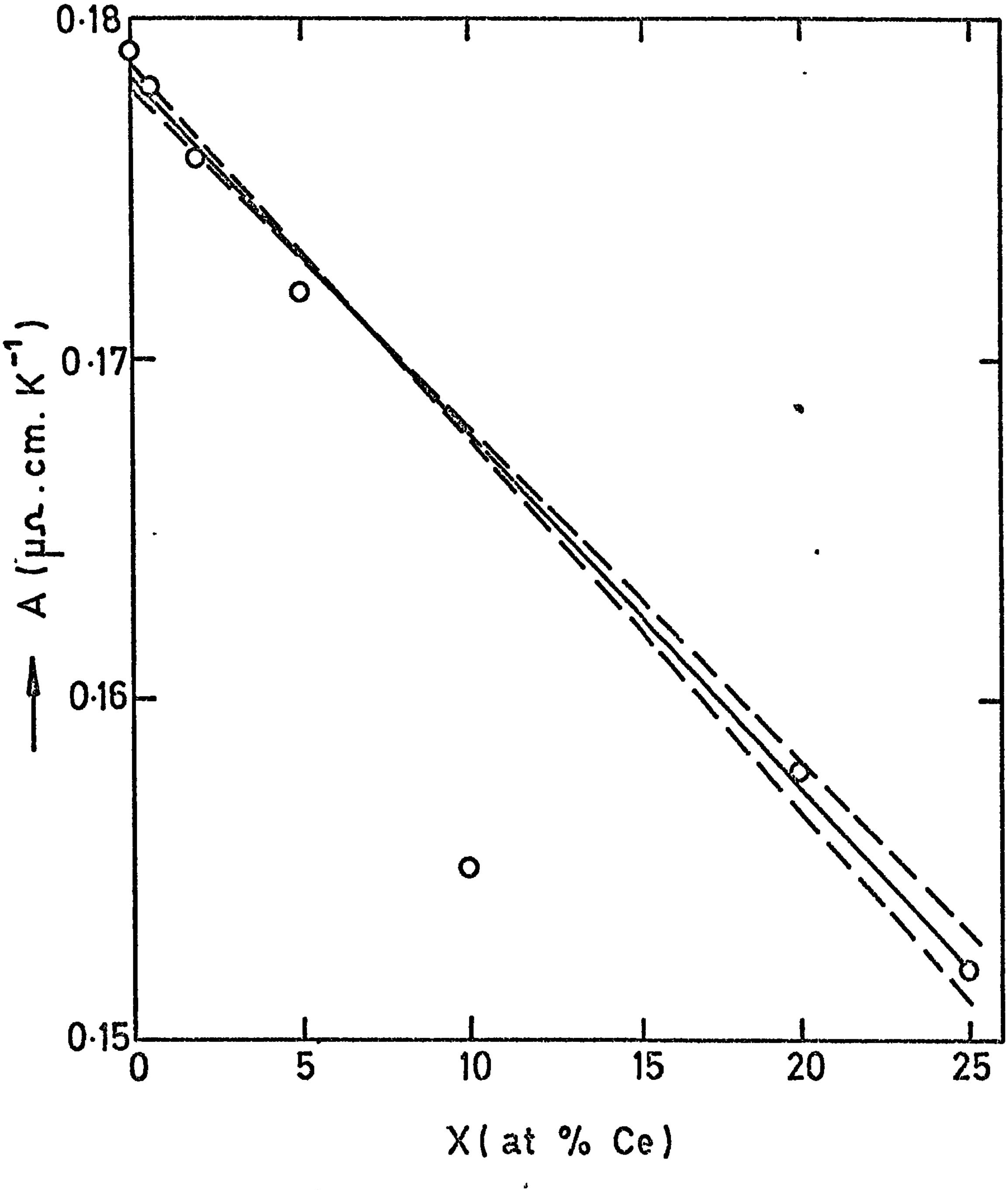

Fig. 7.9: The variation of the phonon fitting parameter A with alloy concentration X.

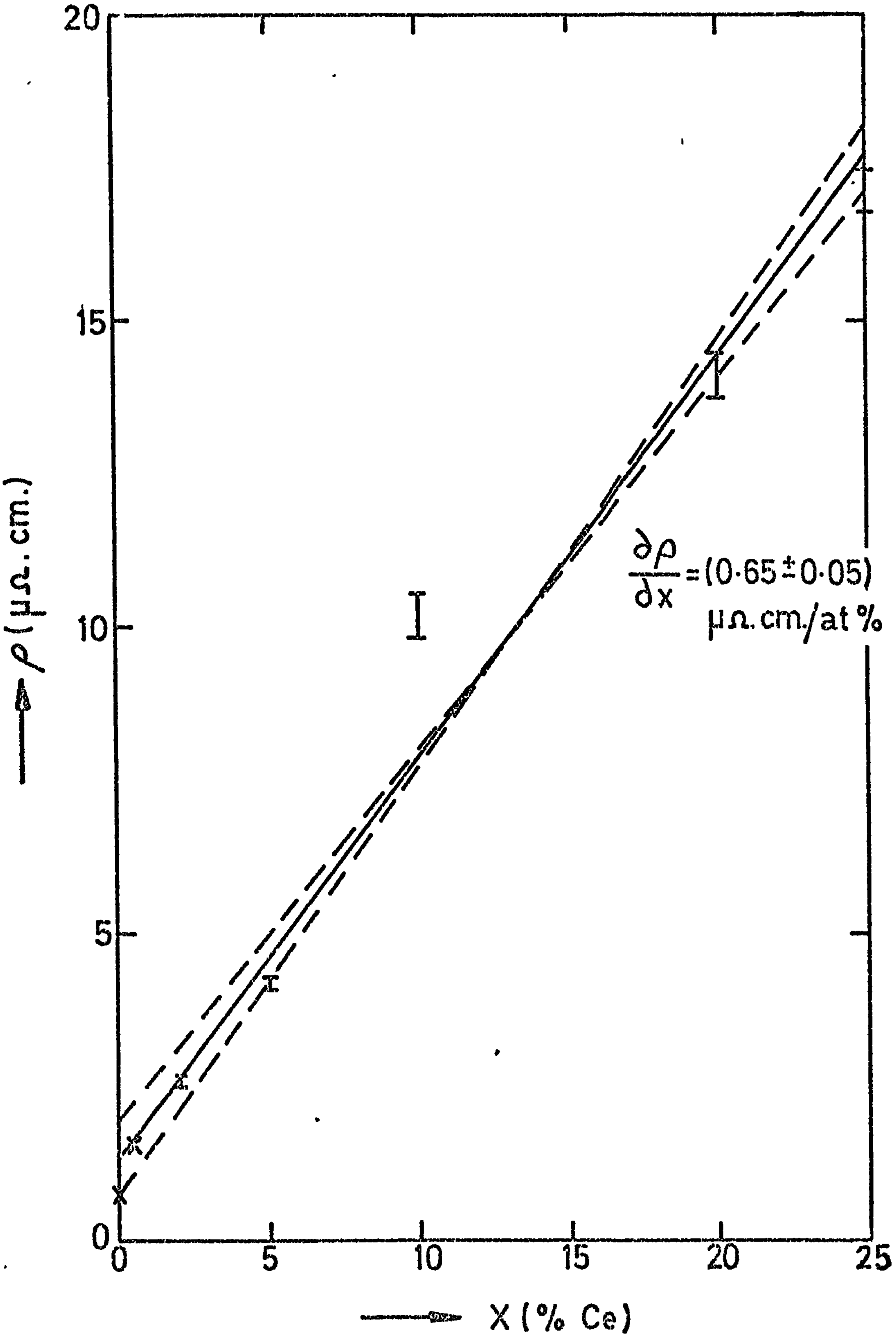

Fig. 7.10: Alloy resistivities at 4.2 K as a function of concentration X.

more dilute alloys are not plotted since the error bars become too large for the results to have much significance. Clearly the systematic agreement of the curves expected for the different compositions is not entirely satisfactory, particularly for the possibly anomalous 10 at.% cerium alloy. However, the general trend of the data is an increase towards lower temperatures, with a hint of structure, in the form of an upward bulge, around 100 K. In fact, the curves look remarkably similar to those predicted by Maranzana [Buschow et al. (1971), Maranzana (1970), Maranzana and Bianchessi (1971)] on the basis of the Kondo sideband model for a total crystalline electric field splitting of the cerium ion of 50 - 100 K (see Chapter 6.2). It seems reasonable to propose that the high-temperature tail of the Kondo sideband may well be quite sufficient to explain the negative slope up to 300 K of the curves of Fig.7.8, and thus also the decreasing slope of the total resistivities as a function of temperature for increasing cerium content (Fig. 7.9). Moreover, the structure apparent at about 100 K may well be the sideband in question, since the cerium crystalline electric field levels calculated in Appendix 1 on the basis of Rainford's crystalline electric field parameters for praseodymium suggest the existence of a state (the $| \pm \frac{5}{2} >$ doublet) at about 90 K. The energy level diagram is drawn below.

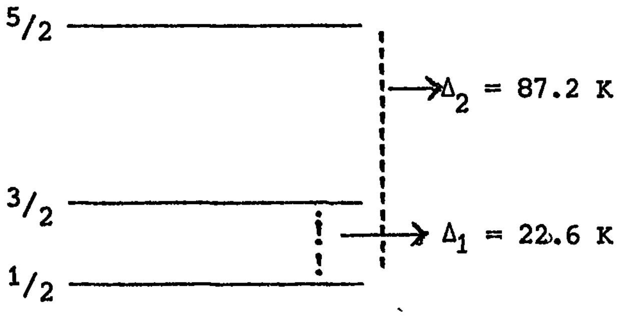

Crystalline electric field levels of Ce^{3+} ion in praseodymium

An alternative approach to the problem of the decreasing slopes shown in Fig.7.9 has been hinted at previously, namely that the phonon resistivities must be individually scaled for each alloy, and this will now be discussed at more length. Ziman (1964) gives an expression for the (constant) limiting high-temperature slope of the phonon resistivity of a metal:

$$\frac{\partial \rho_{ph}}{\partial T} (T \gg \theta) = K\, I \, \frac{n_a^{2/3}}{Ma\theta^2} \left(\frac{S_{free}}{S} \right)^2 \qquad (7.5)$$

where K is a constant involving some fundamental constants, I is a complicated integral depending on the Fermi surface geometry and the form of the electron-phonon scattering anisotropy, n_a is the number of conduction electrons per atom, M is the ionic mass, a is the lattice parameter, θ is the Debye temperature, S is the Fermi surface area, and S_{free} is the value of S calculated on the free electron model. Of course, the strict relevance of Eq.7.5 to the light rare earths must be dubious in view of their failure to reach a constant limiting slope at $T \gg \theta$. However, for qualitative purposes, perhaps the left-hand side of Eq.7.5 may be represented by the parameter A of Eq.7.4. Thus Fig.7.9 implies $\partial A/\partial x = -0.10\ \mu\Omega\,\mathrm{cm}\ K^{-1}$, and $A^{-1}\ \partial A/\partial x = -0.55$, a very rapid variation. Now if in Eq.7.5 it can be assumed that I is independent of x, then since M, a, and θ can only vary by a few percent across the alloy series, the major variation can only arise from the tendency to an increasing valency n_a with increasing cerium concentration and probably to an increase in the ratio (S_{free}/S) consequent on the resultant increasing complexity of the Fermi surface. Thus Eq.7.5 would tend to indicate $\partial A/\partial x > 0$ for increasing valency, a conclusion which is supported by Ziman's interpretation of the increasing ideal resistivity with valency for polyvalent metals [Ziman (1964)].

Hence the present result: $\partial A/\partial x < 0$, is inexplicable on this simple basis. However, perhaps relevant is the fact that at high temperatures (between about 300 K and 1000 K), the ratio of the change in resistivity for pure cerium to that for pure praseodymium is less than unity (about 0.75) [Spedding et al. (1957)], although account must be taken of their differing structures (fcc and dhcp) in this range. Unfortunately, the resistivity data on pure cerium below about 180 K, which show a much higher slope, are probably not relevant because of the structural collapse to a mixed hcp and fcc phase (see Chapter 3.3). Thus it is possible that the Pr-Ce system may be expected to violate the Ziman formula (Eq.7.5), or at any rate our simple interpretation of it, or alternately the unknown variation in the scattering integral I may be dominant.

Accordingly, it seems worthwhile to consider the effect of using a phonon scaling factor $\alpha(x)$ dependent on alloy composition, and on the basis of Fig.7.9 the following scaling factors have been taken, (Table 7.4). The data of Fig.7.8 have been recalculated with these factors, and are shown in Fig. 7.11. The results are now, of course, much more nearly constant than those of Fig.7.8; the high-temperature

Table 7.5: Scaling factors of Pr-Ce system

at.% Ce	0	0.5	2	5	10	20	25
$\alpha(x)$	0.696	0.694	0.688	0.676	0.655	0.614	0.594

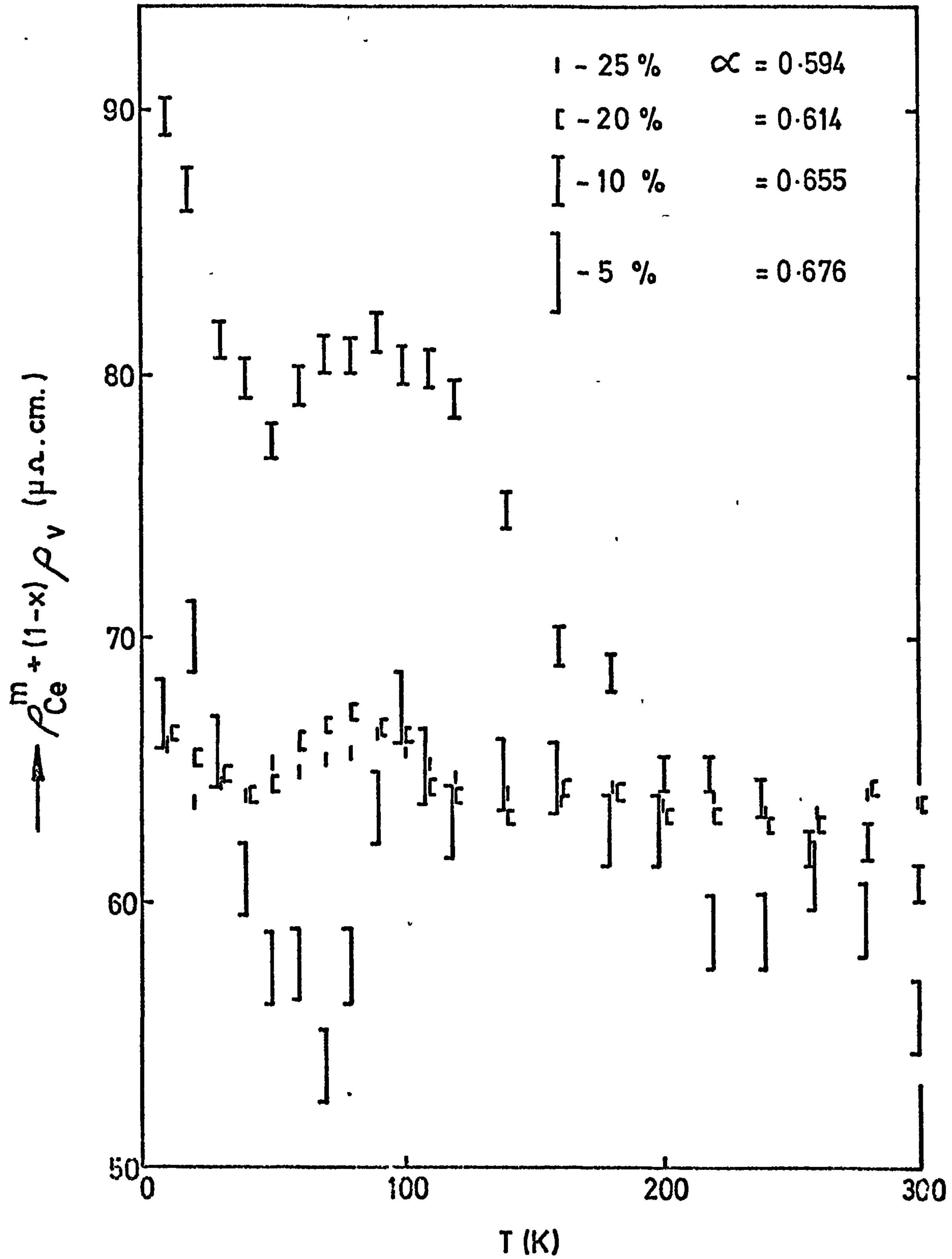

Fig. 7.11: Spin-disorder resistivity of Ce solute normalised to concentration X as a function of temperature T.

tail has been eliminated (except for the possibly anomalous 10% cerium alloy). Again, however, the sideband structure is visible at around 80-100 K in the 10, 20 and 25% cerium alloys; in the 5% cerium alloy there is a suggestion of a shift to higher temperature, but the size of the error bars prevents certainty of this point.

7.6 The Kondo Effect in the Low Temperature Region

So far we have discussed only the gross high-temperature behaviour of the Kondo effect, and we now turn to a consideration of the low temperature region where a Kondo divergence is observed in the three most dilute alloys.

As is seen from Fig.7.3, the temperature at which the minimum occurs, $T_m \approx 4$ K, is almost independent of the solute concentration. However, theory predicts that T_m should vary like $c^{1/n}$, where c is the solute concentration and n is the exponent of temperature in the phonon resistivity (see Table 7.4). The experimental results on T_m definitely contradict this expected concentration dependence, suggesting that there must be some other factors which determine T_m.

In Fig.7.12 are shown the calculated solute resistivities for these alloys as a function of $\ell n T$, where for clarity the results have not been normalized to the concentration x (Eq.7.2), but are plotted absolutely. We have arbitrarily chosen to use the individual scaling parameters $\alpha(x)$ given previously, rather than that for pure praseodymium; the effect of not having done so would have been to lower the ends of the curves progressively towards 30 K by a maximum of about 0.2 $\mu\Omega$ cm at 30 K for the 5% cerium alloy and proportionately less for the more dilute alloys. The depression is quite negligible

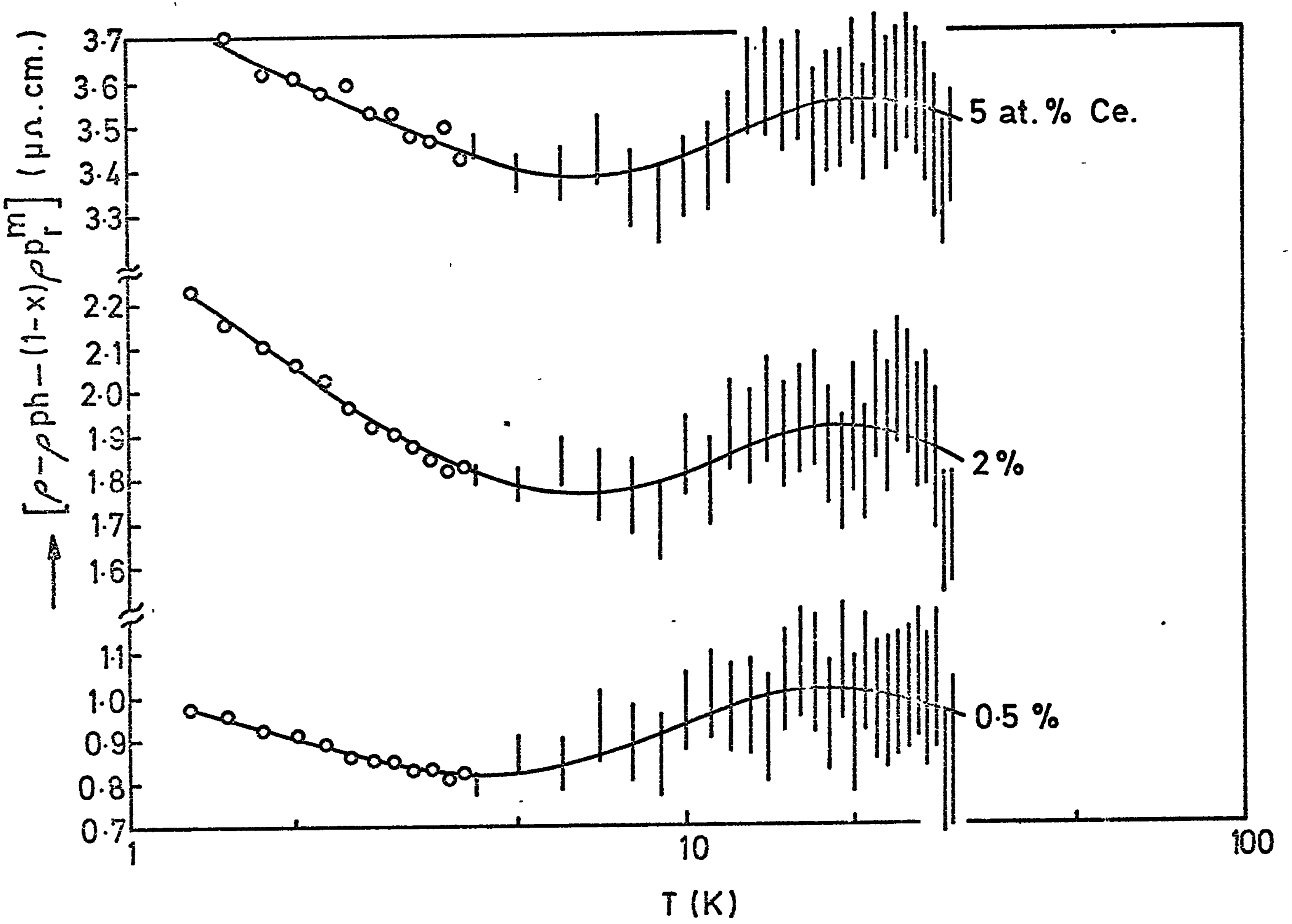

Fig. 7.12: Spin-disorder resistivity of Ce solute as a function of temperature in the range 1.3 - 30 K

below 4.2 K, however, so that the shape of the plots in that region is independent of assumptions about the phonon scaling. Also shown in Fig.7.12 are error bars estimated on the basis of an error in temperature measurement [using the Cu-(AuFe) thermocouple] of about ± 0.2 K; the errors in resistivity are negligible at low temperature but increase rapidly towards 30 K on account of the difficulty in accurately subtracting two steeply rising resistivity curves.

The results of Fig.7.12 are remarkable in again showing, within the limits of the error bars, a hint of structure in the form of a maximum around 20 K independent of the phonon scaling assumptions and again we wish to propose that this could be associated with the 20 K Kondo sideband incurred by the $| \pm {}^3/_2 >$ doublet (see Appendix 1). However, in view of the possible antiferromagnetic transition around 26 K seen in annealed, non-thermally cycled, specimens to be discussed later, the origin of this structure is a little more ambiguous than for the structure at 80 - 100 K (the data in Fig.7.12 are on thermally cycled specimens).

The last point to be made on the data of Fig.7.12 concerns the well established negative slopes below 4.2 K characteristics of the classical Kondo effect, arising probably from the $| \pm {}^1/_2 >$ ground-state doublet (see Appendix 1). As is seen in Chapter 5.3, the slopes in this region are expected to be proportional to concentration x (see Eq.5.18), but this is clearly not the case for the concentrations shown. The slopes normalized to solute concentration are in the ratios 1 : 0.6 : 0.15 in order of increasing solute concentration, and therefore these alloys are far from approaching the dilute limit. Clearly the Kondo effect is being quenched at these levels, and it is of some interest to consider the possible mechanism for this. An obvious candidate is the possible incipience of magnetic ordering, since the 20 and 25 at.% cerium alloys show evidence of what is probably an antiferromagnetic transition at around 4 K (see Fig.7.3). Efforts were made to check this by magnetic measurements using both a susceptibility bridge and a vibrating specimen magnetometer with a sensitivity of about 0.01 μ_B/atom; no sign of ordering could be detected. A second possibility is that the variable electronic structure of the alloys with increasing cerium content is drastically modifying the electronic density of states, and the position of the crystalline electric field levels relative to the Fermi level. In view of these various possibilities, there appears to be no unambiguous way to extrapolating the slopes of Fig.7.12 to zero concentration, and thus there appears to be little point in claiming to be able to calculate a value of the exchange interaction Γ. This is particularly so since the temperatures attained in the present experiments were insufficiently low for the unitarity limit to be approached (see Chapter 5.4), and thus we have no information on the value of the Kondo temperature.

7.7 The Néel-Type Anomaly

Finally, it remains to comment on the occurrence of the apparently antiferromagnetic transition around (26 ± 1)K in the pure praseodymium sample, and in the 5 and 10 at.% cerium alloys, during the first low temperature run after the annealing, as shown in Fig.7.4. A qualitative explanation of the hump-backed anomaly at antiferromagnetic-paramagnetic transitions in metals was mentioned in the introduction chapter (Chapter 1.6). The transition temperature should be compared with 23 K reported by Bucher et al. (1969) from magnetization measurements, ≈ 25 K by Cable et al. (1964) from neutron diffraction work and 22.2 K by Meaden et al. (1972) from electrical resistivity. Meaden attributed the smallness of the resistivity anomaly at the Néel temperature to the crystalline electric field effect which modifies the spin disorder resistivity of praseodymium as discussed in Section 7.4.

The coexistence of this transition with the low temperature Kondo effect in the 5 at.% cerium alloys argues strongly that only one, at most, of the two types of cerium ion (i.e. hexagonal or cubic site) can order; of course it may be that neither participates in the ordering, which may be purely characteristic of the praseodymium matrix. On the basis of the susceptibility measurements on dilute La-Pr alloys Nagasawa and Sugawara (1967) have concluded that of the two types of atomic sites occurring in the dhcp structure of praseodymium, (namely the sites of hexagonal and cubic environments), it is the former which order magnetically at low temperatures while the latter do not. This seems to support the Kondo effect observed in the Pr-Ce alloys.

The disappearance of the transition after sporadic thermal cycling seems to occasion no drastic changes in resistivity at temperatures other than close to 26 K, while x-ray diffraction studies (Harris 1975) indicate that minor strains in the dhcp praseodymium structure tend to anneal out at room temperature anyway. Thus it would seem that if the effect of thermal cycling between 0 and 300 K is structural, the occurrence of the transition must be very sensitive to the precise ratios of hexagonal and cubic sites present.

CHAPTER 8

CONCLUSION AND SUGGESTIONS FOR FURTHER WORK

8.1 Conclusion

The electrical resistivity data have confirmed the existence of a conventional Kondo divergence at T = 0 K in dhcp Pr-Ce alloys and have suggested the existence of Kondo sidebands at temperatures of about 20 and 90 K. The size of the structure in Pr-Ce alloys is relatively more subtle than that obtaining in the CeAℓ compounds, but it has proved possible to relate it to the crystalline electric field parametrization of pure praseodymium given by Rainford. No considerable claims can be made for the accuracy with which the phonon contributions have been subtracted, but at the least the methods adopted are useful means of displaying the structure inherent in the results. Accurate data on other alloy systems should be able to be analyzed in a similar way; for example, those of Elliott et al. (1969) on La-Ce appear to show slight evidence of similar structure at around 60 K (Fig. 2 of their paper). It could be objected that such structure is an artifact of the method of subtraction used. For example, for reasons discussed in Chapter 7, present data on the magnetic resistivity of pure praseodymium show evidence of a maximum around 70 K; it should be pointed out, however, that smoothing out this structure would in fact serve to increase that observed in the alloys at around 90 K (Fig. 7.8). Quenching of the Kondo structure with increasing concentration is observed for all three sidebands while below 4 K there is the possibility of ordering in the 20 and 25 at.% cerium alloys. Sporadic evidence of antiferromagnetic ordering around 26 K has been observed in some alloys, extending the work of Meaden on pure praseodymium.

In connection with the structural properties of the Pr-Ce system, the transition temperatures have been obtained in the solid state from the high temperature electrical resistivity data. At high temperatures, the decreasing hysteresis loop for the dhcp $\rightleftarrows$ fcc transition was observed with increasing praseodymium content and vanished in the $Pr_{.90}Ce_{.10}$ alloy. Alloys with higher Pr content showed no evidence of the transition. The observed similarity between the atomic volumes of the dhcp-Pr and hypothetical fcc-Pr and the disappearance of the dhcp $\rightleftarrows$ fcc transition in the Pr-Ce alloys containing more than 90 at.% Pr have indicated the possibility of there being a delicate relationship in favour of the dhcp phase towards the praseodymium end. (i.e. The free energy of the observed double-hexagonal form of Pr must be only slighly lower than that for a hypothetical face-centered form of Pr). The observed positive deviation from the line connecting the atomic volumes of dhcp-Pr and dhcp-Ce has been attributed to the change of effective valency of cerium from 3.1 to 3. A tentative phase diagram for the Pr-Ce system has been presented which is similar to the La-Nd phase diagram proposed by Gschneidner (1961). X-ray powder diffraction studies have showed that the position of the boundary between solid state phases depends on the thermal treatment of the specimen.

8.2 Suggestions for further work

In order to get more information about the Pr-Ce system it would be instructive to carry out the following:

(a) Detailed resistivity measurements should be extended to lower temperatures (< 1.3 K) in order to test the predicted contancy of solute resistivity, "unitarity limit," below the Kondo temperature.

(b) Thermoelectric power and specific heat measurements could be useful in order to get some information on the value of the Kondo temperature since, in most cases, a well defined peak appears in the above properties at around T_k, the Kondo temperature.

(c) Magnetic susceptibility measurements on single crystals of Pr-Ce alloys would be a useful check on the existence of crystalline electric field effect in the alloys.

(d) Magnetic measurements at higher sensitivity are needed to resolve the possibility of ordering in 20 and 25 at.% cerium alloys below 4 K.

(e) Systematic studies of the influence of annealing and thermal cycling on the occurrence of the antiferromagnetic-paramagnetic transition in the praseodymium-cerium alloys are necessary in order to investigate the precise nature of the transition.

(f) A combination of metallographic, thermal, X-ray diffraction, density etc. experiments are essential to delineate the phase boundaries in the solid and liquid state for the construction of a complete phase diagram for the Pr-Ce system.

APPENDIX 1

Crystal Field Levels of Ce^{3+} in d.h.c.p. environment of Pr

To a first approximation, we may suppose that the crystal field seen by each Ce ion in an alloy is identical with that seen by each Pr ion in pure Pr and is thus independent of x, at least in the dilute alloys. Hence it is of interest to consider the nature of the crystal field levels of Ce ion in both cubic (c) and hexagonal (h) environments of Pr ions. Now Rainford (1971) has given expressions for the spin Hamiltonian for each type of site relative to spin quantization along the d.h.c.p. c-axis as:

$$H_c = B_2^1(c)O_2^o + B_4^1(c)\left[O_4^o + 20\sqrt{2}\,O_4^3\right] + B_6^1(c)\left(O_6^o - \frac{35}{\sqrt{8}}O_6^3 + \frac{77}{8}O_6^6\right) \tag{A1.1}$$

$$H_h = B_2^1(h)O_2^o + B_4^1(h)O_4^o + B_6^1(h)\left(O_6^o + \frac{77}{8}O_6^6\right) \tag{A1.2}$$

where the B_2^1 term vanishes for an ideally close-packed crystal structure, but was taken by Rainford as finite in order to represent the departure of pure Pr from the ideal (c/a) ratio for d.h.c.p. On the unscreened nearest neighbour point-charge model:

$$B_n^1(c) = B_n^1(h) \tag{A1.3}$$

However, Rainford, in attempting to fit the magnetic heat capacity and susceptibility data on Pr, rather arbitrarily takes equation (A1.3) to hold for $n = 4$ and 6, but not for $n = 2$. His fitting parameters are given in Table A1.1, together with those suggested in the earlier work of Bleaney (1963) which treated the structure as being ideally close packed ($B_2^1 = 0$). In discussing the crystal field levels of the Ce ion in the Pr crystalline electric field, a considerable simplification of the Hamiltonians (A1.1) and (A1.2) occurs since the terms in B_6^1 may be neglected. This is because for $J = 5/2$ the matrix elements of the operators O_6^m vanish identically (Hutchings 1964). The hexagonal site

Table A1.1 Crystal field coefficients for Pr as given by Rainford (1971) and Bleaney (1963) expressed in Kelvin, for cubic (c) and hexagonal (h) sites.

	Rainford		Bleaney	
	c	h	c	h
B_2^1	0.0	4.92	0	
B_4^1	2.32×10^{-2}		4.63×10^{-2}	
B_6^1	9.8×10^{-4}		4.9×10^{-4}	

can now be treated very simply, since the remaining terms of Hamiltonian A1.2 are diagonal. Thus the crystal field eigenstates are the Kramers' doublets: $|\pm\frac{1}{2}>$, $|\pm\frac{3}{2}>$, and $|\pm\frac{5}{2}>$ with energies which may be read directly from Hutchings' tables (1964):

$$\left.\begin{aligned} E\left(\pm\tfrac{1}{2}\right) &= -\ 8\,B_2^1 + 120\,B_4^1 \\ E\left(\pm\tfrac{3}{2}\right) &= -\ 2\,B_2^1 - 180\,B_4^1 \\ E\left(\pm\tfrac{5}{2}\right) &= 10\,B_2^1 + 60\,B_4^1 \end{aligned}\right\} \qquad (A1.4)$$

Numerical values using both Rainford's and Bleaney's parameters are given in Table A1.2. It can easily be shown from equation (A1.4) that the critical values of B_2^1/B_4^1 at which the $|\pm\frac{1}{2}>$ and $|\pm\frac{3}{2}>$ levels the $|\pm\frac{1}{2}>$ and $|\pm\frac{5}{2}>$, and the $|\pm\frac{3}{2}>$ and $|\pm\frac{5}{2}>$, cross are 50, 10/3 and -20 respectively. We wish, therefore, to point out that there appears to be a slight error in the graph (Fig.5 of their paper) shown by Buschow et al (1971) of the relative positions of the doublets as a function of B_2^1/B_4^1 when they considered the problem of the Ce ion in the hexagonal crystal field appropriate to $CeAl_3$; the critical values for the level crossings given there are of the order 45, 10 and -10 respectively.

Table A1.2 Crystal field levels of Ce^{3+} ion in Pr host expressed in Kelvin relative to the ground state as zero, using both Rainford's and Bleaney's crystal field parameters.

	Rainford	Bleaney	
$\|\pm\frac{1}{2}>$	0	13.9	hexagonal
$\|\pm\frac{3}{2}>$	22.6	0	
$\|\pm\frac{5}{2}>$	87.2	11.1	
Γ_8	0	0	cubic
Γ_7	12.5	25.0	

The crystal field levels on the cubic sites are almost as easily dealt with. The Hamiltonian of equation A1.1 has only two off-diagonal elements which arise from O_4^3 and couple the $|\pm\frac{1}{2}>$ state with the $|+\frac{5}{2}>$. If $B_2^1 = 0$, the Hamiltonian can be diagonalized exactly to yield eigenstates consisting of a quartet Γ_8

$$|\pm\frac{3}{2}>, \left(\frac{\sqrt{5}}{3} \quad |\pm\frac{5}{2}> \ - \frac{2}{3} \quad |+\frac{1}{2}>\right)$$

and a doublet Γ_7:

$$\left(\frac{2}{3} \quad |\pm\frac{5}{2}> + \frac{\sqrt{5}}{3} \quad |\mp\frac{1}{2}>\right) ,$$

the energy levels being

$$\left.\begin{aligned} E(\Gamma_8) &= - 180 \ B_4^1 \\ E(\Gamma_7) &= + 360 \ B_4^1 \end{aligned}\right\} \qquad (A1.5)$$

Again, numerical values are given in Table 3. These results are identical with those obtained by Lea, Leask and Wolf (1962), when due allowance is made for the fact that their eigenstates are referred to the tetrad as quantization axis, whereas ours refer to the hexad (c-axis). If, however, unlike Rainford, one were to assume that the values of B_2^1 should be as large for the cubic sites as for the hexagonal, since the lattice distortion from close-packing is the same for each, then the term in O_4^3 in the Hamiltonian of equation (A1.1) becomes merely a small perturbation on that of equation (A1.2), and the energy levels are then very nearly identical with those of the hexagonal site.

To summarize the results obtained, it is only in the case of the hexagonal site that there is disagreement between the predictions using Rainford's and Bleaney's parameters over which state is the gound state, being $| \pm \frac{1}{2} >$ and $| \pm \frac{3}{2} >$ respectively. Thus on Maranzana's sideband model, Rainford's hexagonal site would give rise to a Kondo divergence at $T = 0$ while Bleaney's would not, provided of course that the site does not order at low temperatures. On the other hand, both predictions for the cubic site agree in giving a Kondo effect at $T = 0$ since the Γ_8 wave-functions are such as to allow internal spin-flips. On the Cornut-Coqblin model, however, even Bleaney's hexagonal site would give a Kondo effect. The largest overall splitting is for Rainford's hexagonal site, and the smallest for his cubic site. On our tentative assumption that the cubic site could have as large an axial crystal field as Rainford's hexagonal site, both sites would give rise to Kondo sidebands at about 20 and 90 K, assuming that the ground state is located just below the Fermi level.

APPENDIX 2

SYSTEMATIC ABSENCES OF LINES IN POWDER PHOTOGRAPHS OF d.h.c.p. STRUCTURE

The rule for simple h.c.p. is:

absence if $(h+2k)$ is a multiple of 3 and ℓ is odd (see Cullity: "Elements of X-ray Diffraction" pp.122).

Clearly if $(h+2k) = 3n$, then $(h-k) = 3(n-k)$ is a multiple of 3, so the rule may be restated:

absence if : $(h-k)$ is a multiple of 3 and ℓ is odd.

The rule for d.h.c.p. can be expected to be more restrictive than this owing to the increased complexity of the structure.

We may draw a unit cell for d.h.c.p. structure

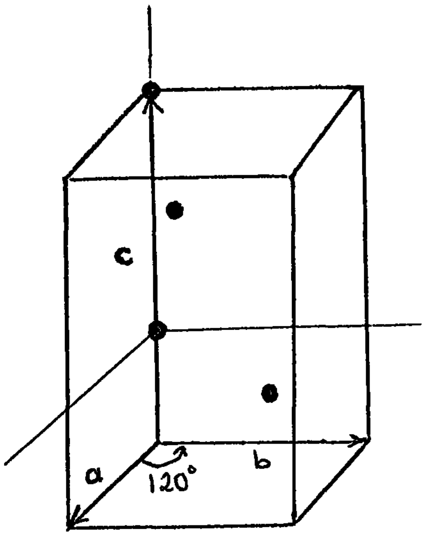

4 atoms per unit cell

$(0,0,0)$

$(\frac{2}{3},\frac{1}{3},\frac{1}{4})$

$(\frac{1}{3},\frac{2}{3},-\frac{1}{4})$

$(0,0,\frac{1}{2})$

Structure factor:

$$F = \sum_J f_J \exp\left[-2\pi i\ (hx_j+ky_j+\ell z_j)\right]$$

where x,y,z are fractional co-ordinates of the atoms,

h.k.ℓ are relative to reciprocal of lattice

f_J is atomic scattering factor.

Therefore $\frac{F}{f} = 1 + e^{-\ell\pi i} + e^{-(\frac{2}{3}h + \frac{1}{3}k + \frac{1}{4}\ell)2\pi i} + e^{-(\frac{1}{3}h + \frac{2}{3}k - \frac{1}{4}\ell)2\pi i}$

It is appropriate to consider the following cases:

$\ell = 4n,\ \ 4n\pm1,\ \ 4n\pm2,\ \ 4n\pm3$ (equivalent to $4n\pm1$)

(i) $\ell = 4n$

$$\frac{F}{f} = 2 + e^{-(\frac{2}{3}h + \frac{1}{3}k)2\pi i} + e^{-(\frac{1}{3}h + \frac{2}{3}k)2\pi i}$$

$\frac{F}{f} = 0$ for systematic absence of reflection.

Now since $|e^{i\theta}| = 1$, this equation can only be satisfied provided:

$$e^{-(\frac{2}{3}h + \frac{1}{3}k)2\pi i} = e^{-(\frac{1}{3}h + \frac{2}{3}k)2\pi i} = -1$$

i.e.

$$\left(\frac{2}{3}h + \frac{1}{3}k\right) = \frac{2p+1}{2}$$

$$\left(\frac{1}{3}h + \frac{2}{3}k\right) = \frac{2p'+1}{2} \qquad p,\ p' \text{ - integers}$$

Therefore

$$h = (2p - p') + \frac{1}{2}$$

$$k = (2p' - p) + \frac{1}{2}$$

But this is impossible because h, k must be integral, i.e. no line with ℓ - multiple of 4 can be absent. This rule represents the fact that there are four equivalent layers per unit cell in the z direction.

(ii) $\ell = 4n\mp1$ (or $4n\mp3$)

$$\frac{F}{f} = e^{-(\frac{2}{3}h + \frac{1}{3}k \mp \frac{1}{4})2\pi i} + e^{-(\frac{1}{3}h + \frac{2}{3}k \mp \frac{1}{4})2\pi i}$$

$\frac{F}{f} = 0$, since $e^{2\pi n i} = 1$

For this to be true, the arguments of the exponentials must differ only by $(2p\mp1)\pi i$

So,

$$\frac{2}{3}h + \frac{1}{3}k \mp \frac{1}{4} = \frac{1}{3}h + \frac{2}{3}k \mp \frac{1}{4} + p \mp \frac{1}{2}$$

Therefore

$$(h - k) \doteq 3p$$

i.e.,

systematic absence if (h-k) is multiple of 3 and

$\ell = 4n \mp 1$ (or ∓ 3).

(iii) $\ell = 4n \mp 2$

All the previous cases also satisfy the rule for hcp, but case (iii) which would give a systematic presence for hcp will be seen to give an absence for dhcp.

$$\frac{F}{f} = 2 + \exp - \left[\frac{2}{3}h + \frac{1}{3}k + (n \mp \frac{1}{2})\right] 2\pi i + \exp - \left[\frac{1}{3}h + \frac{2}{3}k - (n \mp \frac{1}{2})\right] 2\pi i = 0$$

By argument similar to that for $\ell = 4n$, we must have

$$\frac{2}{3}h + \frac{1}{3}k \mp \frac{1}{2} = \frac{2p \mp 1}{2}$$

$$\frac{1}{3}h + \frac{2}{3}k \mp \frac{1}{2} = \frac{2p' \mp 1}{2}$$

Therefore

$$h = (2p - p')$$

$$k = (2p' - p)$$

Therefore

$(h + k) = (p + p')$ ..... No restriction

$(h - k) = 3(p - p')$ i.e. $(h - k)$ must be multiple of 3.

i.e. systematic absence if (h-k) is multiple of 3 and

$\ell = 4n \mp 2$.

Combining the three rules gives:

Systematic absence of relfection (h,k,ℓ) for dhcp structure provided (h-k) is multiple of 3 and ℓ is not multiple of 4.

Now it is easy to enumerate those lines which should be present in Pr using a Bunn Chart for $(c/a) \simeq 3.2$ in order of increasing angle. Absent lines are shown in brackets.

000
(001)
(002)
(003)
100
101
004
102
103
(005)
104
(006)
105
110
(111)
(112)
(007)
106
(113)
200
201
114

202
107
008
203
(115)
204
(116)
108
(009)
205
(117)
206
109
210
(0,0,10)
211
212
207
118
213
1,0,10
214

208
(0,0,11)
215
(119)
300
(301)
(302)
1,0,11
216
(303)
209
(1,1,10)
304
0,0,12
217

REFERENCES

1. Adkins, C.J., 1961, J. Scientific Instruments, 38, 305
2. Alstad, J.K., Colvin, R.V., Legvold, S. and Spedding, F.H., 1961, Phys. Rev. 121, 1637
3. Anderson, P.W., 1961, Phys. Rev. 124, 41
4. Anderson, P.W., 1967, Phys. Rev. 164 352
5. Arajs, S. and Dunmyre, G.R., 1967, J. Less-Common Metals, 12, 162
6. Arajs, S. and Anderson, E.E., 1969, J. Applied Physics, 1969, 40, 3, 1470
7. Barson, F., Legvold, S. and Spedding, F.H., 1957, Phys. Rev., 105, 2, 418
8. Beal-Monod, M.T. and Weiner, R.A., 1968, Phys. Rev. 170 2, 552
9. Beaudry, B.J. and Palmer, P.E., 1974, J. Less-Common Metals, 34, 225
10. Beecroft, R.I. and Swenson, C.A., 1960, J. Phys. Chem. Solids, 15, 234
11. Blandin, A., Coqblin, B. and Friedel, J., 1965, Physics of Solids at High Pressures, ed. by Tomizuka, C.T. and Emrick, R.M. (Academic, New York)
12. Bleaney, B., 1963, Proc. R. Soc, A276, 39
13. Bucher, E., Chu, C.W., Maita, J.P., Andres, K., Cooper, A.S., Buehler, E., Nassau, K., 1969, Phys. Rev. Lett. 22 1260
14. Burov, I.V., Terekhova, U.F. and Savitskii, E.M., 1963, Zh. Neorgan. Khim. 8, 2685
15. Buschow, K.H.J., van Daal, H.J., Maranzana, F.E. and van Aken, P.B., 1971, Phys. Rev. B, 3, 1662

16. Cable, J.W., Moon, R.M., Koehler, W.C. and Wollan, E.O., 1964, Phys. Rev. Lett. 12, 20, 553

17. Clinard, Jr. F.W., 1967, J. Appl. Phys. 38, 4, 1694

18. Colvin, R.V., Legvold, S. and Spedding, F.H., 1960, Phys. Rev. 120, 741

19. Coqblin, B. and Blandin, A., 1968, Adv. Phys. 17, 281

20. Coqblin, B. and Schrieffer, R.J., 1969, Phys. Rev. 185, 847

21. Coqblin, B., 1971, J. de Physique C-1-32, 599

22. Cornut, B. and Coqblin, B., 1972, Phys. Rev. B. 5, 11, 4541

23. Cullity, B.D., 1967, "Elements of X-ray Diffraction" p.122, Addison-Wesley

24. van Daal, H.J. and Buschow, K.H.J., 1970, Phys. Stat. Sol. (a) 3, 853

25. van Daal, H.J., Maranzana, F.E. and Buschow, K.H.J., 1971, J. de Physique 32, C-1, 424

26. Daybell, M.D. and Steyert, W.A., 1968, Rev. Mod. Phys. 40, 380

27. Dekker, A.J., 1965, J. Appl. Phys. 36, 906

28. Dillamore, I.L., Harris, I.R. and Smallman, S.E., 1964, Acta. Met. 12, 155

29. Edelstein, A.S., 1968, Phys. Lett. 27A, 9, 614

30. Edelstein, A.S., Windmiller, L.R., Ketterson, J.B. and Culbert, H.V., 1971, AIP Conference Proceedings No.5, 558

31. Edelstein, A.S., Tranchita, C.J., McMaster, O.D. and Gschneidner, Jr. K.A., 1974, Solid State Commun. 15, 81

32. Elliott, R.O. and Miner, W.N., 1967, Transactions of the Met. Soc. of AIME, 239, 166

33. Elliott, R.O., Hill, H.H. and Miner, W.N., 1969, Phys. Stat. Sol. 32, 609

34. Fisher, K., 1971, Phys. Stat. Sol. (b), 46, 11

35. Francheschi, E. and Olcese, G.L., 1964, Phys. Rev. Lett. 22, 24, 1299

36. Frank, J.P., Manchester, F.D. and Martin, D.L., 1961, Proc. Roy. Soc. (London) A263, 494

37. Friedel, J., 1958, Nuovo Cemento (Suppl.) 7, 287

38. Fulde, P. and Peschel, I., 1972, Adv. Phys. 21, 1

39. De Gennes, P.G., 1962, Le Journal de Physique et le Radium 23, 510

40. Grobman, W.D., 1971, J. Appl. Phys. 42, 1456

41. Grüner, G. and Zawadowski, A., 1974, Rep. Prog. Phys. 37, 1497

42. Gschneidner, K.A. and Waber, J.T., 1959, Annual Meeting Am. Soc. Metals, Chicago

43. Gschneidner, K.A., 1961, Rare Earth Alloys, D. Van Nostrand Comp. Inc.

44. Gschneidner, K.A., Elliott, R.O. and Prince, M.Y., 1962 Rare Earth Research, p.71, ed. Nachman, J.F. and Lundin, C.E. (Gordon & Breach, New York)

45. Gschneidner, K.A., Elliott, R.O. and McDonald, R.R., 1962, J. Phys. Chem. Sol. 23, 555

46. Gschneidner, Jr. K.A. and Smoluchowski, R., 1963, J. Less-Common Metals, 5, 374-385

47. Gschneidner, K.A. and Valetta R.M., 1968, Acta Metalurgica, Vol.16, 477

48. Harris, I.R. and Raynor, G.V., 1969, J. Less-Common Metals, 17, 336

49. Harris, I.R., 1975, Private Communication

50. Harrison, R.J. and Klein, M.W., 1967, Phys. Rev. 154, 540

51. Hedgcock, F.T. and Petrie, B., 1970, Canadian J. of Phys. 48, 11, 1283

52. Heeger, A.J., 1969, Sol. St. Phys. 23, 283

53. Hermann, F. and Skillman, S., 1963, Atomic Structure Calculations, Englewood Cliffs, N.J., Prentice-Hall Inc.

54. Hill, H.H., Miner, W.N. and Elliott, R.O., 1969, Phys. Lett. 28A, 8, 588-589

55. Hirst, L.L., 1967, Sol. St. Comm. Vol.5, 751

56. Howie, A. and Valdrè, U., 1963, Phil. Mag. 8, 1981

57. Hume-Rothery, W., 1936, Institute of Metals Monograph and Report Series, No.1, 222

58. Hutchings, M.T., 1964, Sol. St. Phys. 16, 227-273

59. James, N.R., Legvold, S. and Spedding F.H., 1952, Phys. Rev. 88, 5, 1092-1098

60. Jayaraman, A. and Sherwood, R.C., 1964, Phys. Rev. 134, A691

61. Jayaraman, A., 1965, Phys. Rev. 137, A179

62. Johansson, B., 1974, Phil. Mag. 30, 3, 469

63. Kasuya, T., 1956, Progress of Theoretical Phys. 16, 1, 45

64. Kasuya, T., 1965, in Magnetism IIB, ed. G.T. Rado and H. Suhl (Academic Press)

65. Kevane, C.J., Legvold, S. and Spedding, F.H., 1953, Phys. Rev. 91, 6, 1372

66. Klement, W. and Jayaraman, A., 1967, Prog. Sol. St. Chem. 3, 289

67. Kondo, J., 1962, Prog. Theor. Phys. (Kyoto), 28, 846

68. Kondo, J, , 1964, Progress of Theoretical Physics, 32, No.1, 37-49

69. Kondo, J., 1969, Sol. St. Phys. 23, 183

70. Krithivas, G., Meaden, G.T. and Szę, N.H., 1972, J. Phys. Soc. of Japan 33, 6, 1584-1590

71. Lea, K.R., Leask, M.J.M. and Wolf, W.P., 1962, J. Phys. Chem. Sol. 23, 1381

72. Lehmann, H.W. and Meier, E., 1970, J. Phys. E. 3, 326

73. Levine, M. and Suhl, H., 1968, Phys. Rev. 171, 2, 567

74. Likhter, A.I. and Venttsel, V.A., 1962, Sov. Phys. Sol. St. Vol.4, No.2

75. Lock, J.M., 1957, Proc. Phys. Soc. (London), B70, 566

76. Lundin, C.E., Nachman, J.F. and Yamamoto, A.S., 1966, Acta. Met., 13, 149

77. Mackintosh, A.R., 1962, Phys. Rev. Lett. 9, 90

78. Maranzana, F.E., 1970, Phys. Rev. Lett. 25, 239

79. Maranzana, F.E. and Bianchessi, P., 1971, Phys. Stat. Sol. B. 43, 601

80. Maple, M.B., Wittig, J. and Kim, K.S., 1969, Phys. Rev. Lett. 23, 24

81. McHargue, C.J., Yakel, H.L. Jr. and Jetter, L.K., 1957, Acta Cryst. 10, 832

82. McHargue, C.J. and Yakel, H.L. Jr., 1960, Acta Met. 8, 637

83. McWhan, D.B. and Stevens, A.L., 1965, Phys. Rev. A682, 139

84. McWhan, D.B. and Stevens, A.L., 1967, Phys. Rev. 154, 438

85. McWhan, D.B., 1970, Phys. Rev. B. 1, 6, 2826

86. Meaden, G.T., 1971, Contemp. Phys. 12, 313

87. Meaden, G.T., Sze, N.H., Krithivas, G. and Zuckermann, M.J., 1971, J. de Physique C-1-375 32

88. Meaden, G.T., Krithivas, G. and Sze, N.H., 1972, J. Phys. Soc. Japan, 33, 1584

89. Mills, D.L., 1972, "Magnetism in Alloys" ed. by P.A. Beck and J.T. Waber, pub. by Metallurgical Society of AIME

90. Nagaoka, Y., 1965, Phys. Rev. 138, A1112

91. Nagaoka, Y., 1967, Prog. Theoret. Phys. (Kyoto), 37, 13

92. Nagasawa, H. and Sugawara, T., 1967, J. Phys. Soc. Japan, 23, 4, 701

93. Nelson, J.B. and Riley, D.P., 1945, Proc. of the Phys. Soc. Vol.57, 160-177

94. Norman, M., Harris, I.R. and Raynor, G.V., 1966, J. Less-Common Metal, 11, 395-402

95. Otte, H.M. and Chessin, H., 1965, Phys. Stat. Sol. 11, 91

96. Pauling, L., quoted by Schuch, A.F. and Sturdivant, J.H., 1950 J. Chem. Phys. 18, 145

97. Piermarini, G.J. and Weir, C.E., 1964, Science 144, 69

98. Ponyatovskii, E.G., 1958, Sov. Phys. JETP, 469

99. Popplewell, J., Arnold, P.G. and Davies, P.M., 1967, Proc. Phys. Soc. 92, 177

100. Purwins, H.G., 1972, Ann. Phys. 7, 329-348

101. Rainford, B.D., 1971, A.I.P. Con. Proc. No.5, Magnetism and Magnetic materials, 591-610

102. Ramirez, R., and Falicov, L.M., 1971, Phys. Rev. B. Vol.3 8, 2425

103. Ruderman, M.A. and Kittel, C., 1954, Phys. Rev. 96, 1, 99

104. Sarachik, M.P., Corenzwit, E. and Longinotti, L.D., 1964, Phys. Rev. Vol.135, No.4a, 1041-1045

105. Schrieffer, J.R. and Wolff, P.A., 1966, Phys. Rev. 149, 491

106. Smidt, F.A. and Daane, A.H., 1963, J. Phys. Chem. Sol. 24, 361

107. Spedding, F.H., Daane, A.H. and Herrmann, K.W., 1957, J. of Metals, 895

108. Spedding, F.H., Hanak, J.J. and Daane, A.H., 1961, J. Less-Common Metal 3 110-124

109. Spedding, F.H., Valletta, R.M. and Daane, A.H., 1962, Trans. Am. Soc. Metals, 55, 483

110. Speight, J.D., Harris, I.R. and Raynor, G.V., 1968, J. Less-Common Metals, 15, 317-330

111. Stephens, D.R., 1965, J. Phys. Chem. Sol. 26, 943

112. Stephens, A.E., Mackey, H.J. and Sybert, J.R., 1971, J. Appl. Phys. 42, 2592

113. Stevens, K.W.H., 1952, Proc. Phys. Soci. A65, 209

114. Sugawara, T., 1965, J. Phys. Soc. Japan, 20, 12, 2252

115. Sugawara,,T., Yamase, I. and Soga, R., 1965, J. Phys. Soc. Japan, 20, 618

116. Sugawara, T. and Eguchi, H., 1966, J. Phys. Soc. Japan, 21, 725

117. Sugawara, T. and Yoshida, S., 1968, J. Phys. Soc. Japan, 24, 1399-1400

118. Sugawara, T. and Eguchi, H., 1969, J. Phys. Soc. Japan 26, 1322

119. Sugawara, T. and Yoshida, S., 1971, J. of Low Temp. Phys. Vol.4, No.6, 657-663

120. Suhl, H., 1967, Theory of Magnetism in Transition Metals, W. Marshall, Ed., Academic Press, N.Y.

121. Taylor, K.N.R. and Darby, M.I. 1972, Physics of Rare Earth Solids, Chapman and Hall .

122. Watabe, A. and Kasuya, T., 1969, J. Phys. Soc. Japan 26, 1, 64

123. Wilding, M.D. and Lee, E.W., 1965, Proc. Phys. Soc. 85, 955

124. Wilkinson, M.K., Child, H.R., McHargue, C.Jr, Koehler, W.C. and Wollan, E.O., 1961, Phys. Rev. 122, 1409

125. Wittig, J., 1968, Phys. Rev. Lett. 21, 17, 1250

126. Yosida, K., 1957, Phys. Rev. 107, 2, 396

127. Zachariasen, W.H., 1949, Phys. Rev. 76, 301

128. Zener, C., 1951, Phys. Rev. 1, 440

129. Ziman, J.M., 1964, Electrons and Phonons (Oxford: Oxford Univ. Press), 374

130. Zinov'ev, V.E., Gel'd, L. P., Morozova, V.A. and Chuprikov, G.E., 1974, Sov. Phys. Sol. St. Vol.15, No.7, 1499